Carbon Coatings as a Tool for Controlling Surface Chemistry of Materials

By

Paige Carolyn Kinsley

A dissertation submitted in partial fulfillment of

the requirements for the degree of

Doctor of Philosophy

(Chemistry)

at the

UNIVERSITY OF WISCONSIN – MADISON

2022

Date of final oral examination: May 31, 2022

The dissertation is approved by the following members of the Final Oral Committee:
- Robert J. Hamers, Professor, Chemistry
- Timothy H. Bertram, Professor, Chemistry
- Randall Goldsmith, Professor, Chemistry
- Christy L. Haynes, Professor, Chemistry, University of Minnesota

Carbon Coatings as a Tool for Controlling Surface Chemistry of Materials

Paige Carolyn Kinsley

Under the supervision of Professor Robert J. Hamers

University of Wisconsin – Madison

Abstract

Carbon coatings provide a versatile handle on the surface control of materials, from controlling reactivity to increasing conductivity to providing a surface for functionalization. We have developed and characterized two applications of carbon coatings to two different systems, one to control the surface reactivity of red phosphorus, and the second to stably control the surface chemistry of metal oxide nanomaterials.

Red phosphorus, when exposed to humid atmospheres, degrades into toxic phosphine gas and acidic phosphorus species, introducing a challenge for applications as a flame retardant and pyrotechnic obscurant. We have developed and characterized a plasma-deposited nanometers-thin carbon coating to suppress degradation of red phosphorus. Using a combination of novel infrared headspace analysis and surface analysis by X-ray photoelectron spectroscopy, we quantified and developed an understanding of the reaction of red phosphorus with water vapor and the suppression of decomposition using a plasma-deposited graphitic carbon coating. Phosphine production, quantified by gas-phase IR, was accompanied by the production of phosphoric and phosphonic acid surface species. Increasing plasma deposition time increased the thickness and uniformity of the carbon coating, corresponding to a decrease in phosphine and PO_x species generation. This plasma-deposition method produces a thin, non-reactive carbon coating that provides a solution for long-term stability of red phosphorus.

Metal oxide nanomaterials are of interest for studying the interactions of nanoparticles in the environment, from long-term optical tracking using nanoruby, to studying the formation of protein coronas on superparamagnetic iron oxide, to efficiently delivering micronutrients to plants with zinc oxide. However, long-term surface species control of these materials is challenging. We have developed a novel carbon coating method to apply a nanometer thin carbon coating applicable to multiple metal oxides via the adsorption and then carbonization of a fatty acid monolayer. We show that this carbon coating can be further functionalized through a carbon-carbon bond using a thermal radical initiator, allowing us to stably bind ligands with a variety of charge and chemical characteristics. This carbon coating on metal oxides offers a platform for stable, long-term functionalization, providing a powerful tool to gain deeper insight into the interactions of nanomaterials in biological systems.

Alongside the studies done on novel carbon coatings, I also looked at the impact of a community-engaged learning undergraduate course, Service with Youth in STEM. This course provides a multifaceted framework for student learning, community engagement, and STEM identity growth, alongside opportunities for mentorship and the development of science communication skills. We found that the structure of the course improved student confidence in science, science communication, and their own science identities, with potential long-term impacts on engagement and retention in STEM fields for both undergraduate students and the communities they serve.

Acknowledgements

Grad school is not something that can be done alone. It requires a community of support and love and laughter, of people that will push you do better and to think harder. I have been unbelievably lucky in the community that has helped me through this insane roller coaster during these past five years.

First, thank you, Bob, for building a space, both in the group and in the CSN, for me to grow and learn as both a scientist and a person.

To the Center for Sustainable Nanotechnology, for funding this wild journey through graduate school and giving me unbelievable friends along the way. (And letting me make all those friends do improv). To Miriam Krause, for offering support and resources for all my adventures in outreach. To Arielle Mensch, for being a friend and mentor all through grad school, even though we were never really in the same place at the same time. To Steph Mitchell, for sharing your passion and light about science and outreach. Never have I had such a beautiful collaborative experience than with you and Jaya.

To Mike Schwartz, for being a shelter and sanity check through the storm that is grad school, helping me cut through the tangle of research to find what was important to me and being the loudest and most fervent advocate for students in the CSN and the chemistry department.

To all the chemistry department staff who have kept this ship (literally) afloat during my time in grad school. To Jeff Neilsen, for holding up the building walls as things seemed to fall down around us. To Sue Martin-Zernicke, for keeping us organized, reimbursed, and just generally taking care of when we couldn’t take care of ourselves.

To the Public Service Fellows, for giving me a space to explore the impact of science outside of research and academia. Your support and validation pushed me towards finding a job and career that are fulfilling. To Anna, for being both mentor and friend, for teaching me about the importance of community, and for showing me that the path forward may not me straight, but you’ll end up where you need to be in the end. To Evan, for being my support mirror for the last year. Your friendship through this transitory period of our lives was something I didn’t realize I needed until we found each other.

To Atlas Improv and Anne Lynn Gillian-Daniel, for teaching me the power of “Yes, and…” and giving me the tools to show others how improv can transform science.

To my friends and teachers at Barrio Dance, for lifting me up and giving me music and laughter and joy in my final year in Madison.

To the Hamers group, for being so much more than a research group. Graduate school would have been impossible without the laughter and support and antics of this group, from 100 rubber ducks to (at least) 12 pounds of jellybeans to too many twinstances to count. For the support in solving research problems to troubleshooting instruments to tearing apart presentations. You all have kept me engaged and growing as a scientist and a person these past five years. To Connor, for being my rock and keeping me sane in my final semester with delicious food and stupid movies and goofy podcasts. To Katie, for always having a book recommendation on hand and being willing to take any of mine (no matter how crazy). To Louis, for the long engaging conversations about anything and everything we needed to put out in the world (and also reading all my crazy books). To Jaya, for the conversations and validations and warm hugs, no matter the distance. To Rebeca (you're essentially a member of the group), for taking me on adventures and letting us weirdos hang around even when the puns got really bad. To Zack, for your humor and calm presence and love of fancy mixed drinks. I looked forward to coming in to work every day because of you. To Liz, for being my best friend and mentor. You have kept me grounded and laughing and thriving during grad school even when things were darkest. You bring me joy every day, and I truly, truly cannot wait to see what we build together at Argonne (dreams really do come true).

To Ethan, for being with me through crazy transitions and train trips, and for supporting me through some of the hardest times I've had. You kept me floating, and I will forever appreciate that.

To my family, for the love and support that has made me into the person I am today. To my parents, for never saying, "No, you can't do that," instead saying "ok what's next?" For feeding me tasty food and teaching me to love an adventure but knowing when it's time to take a sit and sip. To my brother, for being a friend across continents and oceans, and being the best weirdo nerd a sister could ask for.

Finally, to Grandma, for planting seeds of curiosity and wonder that have guided me since the beginning and for showing me that being just a little weird only make things more interesting. I wish you could've seen me graduate. I miss you every day.

Table of Contents

Chapter 1: Background and Introduction

1.1. Carbon as a material

Carbon is the stuff of life,[1] the fundamental component of all living organisms on Earth. This fact alone makes it amazing. Carbon in its elemental form has properties that span the extremes of material properties. Carbon allotropes, ranging from graphite to diamond to amorphous carbon, are dependent on sp^2 and sp^3 content as well as structural morphology, both which have significant impacts on the functionality of the material.[2] Graphite, with its high sp^2 content within each 2-dimensional layer, along with weak Van der Waals forces between graphene layers, is one of the softest materials known, sheering easily, and displays superlubricity, the regime in which friction very nearly vanishes.[3] The extended network of double bonds in the basal plane makes it an extremely effective electrical conductor.[4] Diamond, on the other hand, made of an extended tetrahedral crystal lattice of sp^3 carbon, is the hardest material known and is used as the ultimate abrasive. Diamond is also an effective electrical insulator,[5] and the best naturally-occurring thermal conductor.[4] Both diamond and graphite are highly chemically resistive, surviving extremes in pH, ionic strength, and solvent.[4]

Other allotropes of carbon can be mapped on a ternary phase diagram with graphite, diamond, and hydrocarbons in each corner, varying in sp^2 and sp^3 content as well as degree of crystallinity and hydrogen content.[6, 7] Allotropes within this diagram are generally known as amorphous carbon, though show high variability in structure and function. As an example, diamond-like carbon (DLC) is a material with a variable mix of sp^2 and sp^3 but no long-range order.[4] DLC has outstanding hardness and a low coefficient of friction, and, like graphite and diamond, is chemically inert.[4] DLC is often applied as a thin coating (no greater than a few microns). However, even at a nanometer thickness, DLC is an effective diffusion barrier against moisture and gases.

The tunability of properties of carbon allotropes make them exciting materials to study and apply, from batteries to optics to coatings.

1.2. Versatility of carbon coatings

Researchers across a huge variety of fields are interested in taking advantage of some these impressive properties carbon shows, particularly applied to surfaces and interfaces, applying carbon as a coating. Variability in carbon precursors and deposition methods means we can form a variety of carbon coatings with different functionalities, from surface passivation to increasing conductivity.[8-10] Carbon coatings are often made up of carbon with variable sp^2/sp^3 content, falling in the regime of diamond-like carbon.

The most common methods used in applying carbon coatings are through chemical vapor deposition (CVD)[9, 11, 12] or through pyrolysis of adsorbed carbon precursors on the surface of the material.[8, 13, 14] CVD parameters, such as carbon precursor, temperature, pressure, and plasma creation technique (microwaves or radio waves) can be used to tune the sp^2/sp^3 content as well as the C/H content. Deposition time can be used to control coating thickness.[4] For pyrolyzed samples, carbon precursors such a polymers, sugars, or fatty acids are initially adsorbed to the material surface, then heated to carbonize, often creating a more graphitic coating.

Graphitic carbon coatings have been used to increase performance[15] and conductivity of lithium battery cathode materials, with the advantage of showing impressive lithium ion diffusion.[16] These carbon coatings also protect the cathode material from direct contact with the electrolyte, preventing side reactions between the electrode and electrolyte that cause degradation to both, as well as the formation of potentially dangerous side products.[17] The chemical inertness of the carbon coating itself inhibits chemical reactions between the coating and the electrolyte or electrode.

Carbon coatings have also been applied in biological systems, particularly as coatings for biomedical devices and implants.[18] Studies have shown that diamond-like carbon coatings are resistant to corrosion in biological systems.[12] Additionally, because of the graphitic character of most DLC coatings, they are resistant to wear thanks to their low coefficient of friction,[19] which is especially important if coating replacement joints. A major challenge in biomedical implants is the foreign body response, in which the body has an inflammatory response to the implant, attempting to isolate the foreign object from the body with collagen build up then breaking it down.[20] Diamond-like carbon coatings when tested both in vitro and in vivo, show low toxicity and no inflammatory response, allowing for long-term implantation.

We are interested in taking advantage of the versatility of carbon coatings as a method of both surface passivation, but also as a platform for secondary functionalization, using the power of organic chemistry to attach small molecules to the surface to control surface chemistry.[21] Carbon coatings are a powerful tool to assist in answering questions about nanotechnology in complex biological systems.

1.3. Understanding the interactions of nanomaterials in the environment

Nanomaterials are being used more and more often in industrial applications, from metal oxides in phone and computer batteries[22] to quantum dots in television screens[23] to silver nanoparticles in clothing[24]. While the small size and high reactivity of these materials makes them excellent for their intended applications, their fate once they are no longer in their intended environments is a complex challenge, particularly when interacting with biological systems.[25] Nanomaterials, defined as having one dimension between 1 to 100 nm[26], are on the same size order of cellular membranes and organelles, allowing them to interact with living organisms in unique and complex ways.[27]

Upon release in to the environment, interactions of nanomaterials in biological systems is largely controlled by the chemical species on the surface.[28, 29] The surface will control where it goes (does it stay in solution or precipitate out?),[30, 31] how it interacts (is it internalized into cells or does it remain on their surface?),[32, 33] and what chemistry it does (does is it release ions, undergo oxidation or reduction, remain inert?).[34] Studying where nanomaterials go and how they interact is challenging because of their extremely small size, made even more complicated by the complex biological systems that are of interest.

1.3.1. Optical tracking of nanomaterials in complex biological systems

One solution for understanding nano-bio interactions is using "model" fluorescent nanomaterials that allow for optical tracking even in systems with large amounts of autofluorescence.[35] An ideal material for long-term tracking in biological systems is (1) chemically stable, undergoing no transformations even in complex systems, (2) biologically compatible, (3) easily functionalized, and (4) has stable fluorescence than can be differentiated from biological autofluorescence.[36] With intentional control of the chemistry of the surface of such a material, we would be able to connect surface chemistry of materials on where they go in biological systems. Two emerging materials that fit these parameters are nanoruby and nitrogen-vacancy (NV) doped nanodiamond.

NV-nanodiamond has the chemical inertness of diamond while also having a surface that can be functionalized through carbon-carbon bonds with molecules with a breadth of functionality.[21, 37] The nitrogen-vacancy center that gives diamond fluorescence, made up a substitutional nitrogen next to a vacancy in the crystal lattice, provides long-term photostability, with broad emission above 650 nm.[36] Additionally, because of its electronic structure, the particle fluorescence can be modulated by either microwave or magnetic fields.[38, 39] This modulation allows for background subtraction of biological fluorescence, leaving only nanodiamond fluorescence in both spectra and images.[40] The carbon surface of nanodiamond provides a platform for functionalization with a variety of molecules.[37] This allows for tunable, stable surface chemistry control, an important aspect when parsing apart how nanomaterials interact in the environment. While nanodiamond is a powerful tool for optical tracking in biological systems, NV modulation can add technical complexity to imaging systems.

Another material with long-term fluorescence is nanoruby. Nanoruby is Al_2O_3 doped with chromium with a strong narrow emission line at 694 nm.[41] Aluminum oxide, as with diamond, is chemically stable and will not undergo chemical transformations in biological systems. Also like diamond, the fluorescence of ruby arises because of a defect in the crystal lattice, namely Cr^{3+}, making it extremely photostable. While nanoruby is often called a “fluorescent” material, the mechanism of emission is actually phosphorescence, with emission lifetimes on the order of ~3 ms.[42] This is orders of magnitude longer than autofluorescence in biological systems, which is often on the order of nanoseconds. This means distinction of nanoruby for fluorescent background can be done using time-gated imaging, in which after the initial excitation pulse from the light source, there is an intentional delay in detection during which time background fluorescence decays away while nanoruby emission persists.[41] A challenge of using nanoruby is the current limited capacity for long-term functionalization of the surface, with most methods lacking stability in complex biological systems. A solution to this challenge is addressed in Chapter 3 of this thesis.

1.3.2. Corona formation and identity on nanomaterials

While understanding where nanomaterials go in biological systems is important, another aspect to exploring the interaction of nanomaterials in the environment is understanding how biological molecules, both small and large, interact with nanomaterials. The adsorbed biomolecules, often consisting of proteins, lipids, and metabolites, is known as the corona, or eco-corona.[43] The identity of the nanomaterial and the species on its surface control what adsorbs to the particle surface and for how long.[44, 45] The identity of the molecules in the corona control the biological identity of the nanomaterial, impacting their physiological impact and interaction with biological systems.[46] Not only that, the identity of the corona can chemically alter the nanomaterial,[47] and the nanomaterial can similarly change the functionality of the molecules in the corona.[48] Studying the formation and identity of the corona can be challenging. After nanoparticle exposure to a biological medium, the nanoparticles are most often separated using centrifugation.[49] Coronas, particularly protein coronas, are often composed of a "soft corona," composed of weakly-bound, nonspecific species, and a "hard corona," composed strongly bound, physi- or chemisorbed species. Centrifugation often desorbs the soft corona, losing important information on what species are actually exposed to solution. Recent work has looked at superparamagnetic iron oxide nanoparticles as a potential solution to this problem.[50] These Fe_3O_4 nanoparticles provide a method for gentle retrieval of nanoparticles from solution, maintaining the soft corona for further analysis, deepening the understanding of the biological identity of these materials after exposure to complex matrices.

Unsurprisingly, the initial surface of the nanoparticle placed in the biological matrix is important in controlling what ultimately adsorbs. Therefore, for rigorous study of protein corona formation, intentional control of the nanoparticle surface of interest is important. For a material like magnetically-retrievable iron oxide, long-term functionalization is challenging, similar to aluminum oxide, in that most species bound to the surface through metal-oxygen-carbon bonds, or even silane bonds, are easily detached or exchanged when placed into solutions of variable pH, ionic strength, and compositional complexity.[51] A proposed method of control of metal oxides like iron oxide is given in Chapter 3, allowing for long-term control of surface chemistry.

1.3.3. Metal oxide nanomaterials in agriculture

Intentional surface control of model nanomaterials is important to continue to understand how nanomaterials interact in biological systems. However, this surface control can be extended to relevant applied materials as well. In particular, there has been an increasing interest in using nanomaterials to improve plant health and suppress disease.[52] As the global population continues to increase while water and arable land continue to decrease, new strategies for sustainable agriculture need to be investigated.[53] Additionally, disease and pests are major factors in crop loss, accounting for 20-40% decreases in yield.[54] Use of nanomaterials offers a method to more efficiently apply macro- and micronutrients and pest controls to plants.[55]

Traditional applications of nutrients and pest controls require the dissolution of the salt of interest in water, copper sulfate for example, followed by spraying the solution on the crop. This method has a number of drawbacks, the first being poor adsorption of the aqueous salts to the crop leaves. These salts can be easily washed off by rain, making their way into the soil. Once there, they are transformed into species inaccessible to plants due to alkaline conditions or chelation by organic molecules, as well as being detrimental to the local microbiome that supports plant health.[56] Runoff containing these nutrients can also affect the ecosystem even further afield, causing eutrophication harmful to other species in the area.[57]

Nanomaterials offer solutions to some of these problems. Studies comparing copper-based nanomaterials to their salt-based counterparts have shown that less material by copper content is needed to have the same effects on improved plant health and disease suppression in watermelon.[58] The high surface area of nanomaterials also allows them to adsorb more effectively to leaf surfaces, preventing runoff into the soil. The tunability of morphology of nanomaterials also gives control of interaction with and uptake in plants, with evidence that nanosheets bind more efficiently to leaves than nanospikes, which corresponds to an increase in plant health.[59] Alongside morphology, surface species and surface charge on nanomaterials also impacts their uptake and translocation in plants.[60] Fine control over morphology and surfaces species of nanomaterials would allow for more targeted interaction and nutrient delivery in plants, providing tools to better grow crops in a sustainable, efficient manner.

1.4. Community-engaged learning for the benefit of both students and their communities

In 1905, University of Wisconsin President Charles Van Hise put forward an idea on the relationship of the university and the people of Wisconsin: “I shall never be content until the beneficent influence of the University reaches every family of the state.”[61] This philosophy was the seed that bloomed into what is now known as the Wisconsin Idea. First formalized by Charles McCarthy in his 1912 book by the same name,[62] the Wisconsin Idea has transformed into a commitment by the University of Wisconsin system to serving the government and people of the state of Wisconsin by directing policy and carrying out research to solve problems that are important to residents of the state.[63]

One form the Wisconsin Idea takes, not only at the University of Wisconsin, but across academia is through community-engaged learning courses. Community-engaged learning (CEL) combines students learning into courses with community experiences, centered on the partnership between the university and local community.[64] These partnerships connect university students to their local community, building relationships between university and community, while also addressing community-identified needs.[65] You’re now probably asking how this is relevant to science and STEM researchers at a university, and why this is showing up in a chemistry Ph.D. thesis. Well, let me tell you.

How we teach science impacts both *who ends up as a scientist* and *what research questions are asked*.[66] Traditional methods for teaching science, technology, engineering, and math (STEM) subjects, both at the grade-school and undergraduate levels, focus on learning fundamentals and foundations of the subject, asking students to memorize concepts often without contextualizing how they might connect to the broader world and students' day to day lives.[67] When there are attempts to connect to historical contexts, the role models put forward often all look the same (male and white), adding another layer of discouragement for those already underrepresented in the field.[68] Studies have found that a sense of belonging in science, stemming from confidence in your own abilities as well as seeing yourself in those around you, is key to recruiting and retaining students in STEM.[69]

STEM community-engaged learning courses at the undergraduate level can address a number of these issues. Studies have shown that CEL courses in which students have direct interaction with non-science experts in the community, whether they are K-12 students or adults, improve scientific communication skills.[70] Opportunities to teach and talk about science to non-experts increases confidence and reaffirms science identity. Undergraduate students also step into the role of science role model for K-12 students, providing real-life examples of scientific success to younger students.

Because of the focus of community-engaged learning courses is *community engagement*, the courses often have students go beyond one-directional, deficit-based thinking in their interactions with the community. Deficit-based thinking assumes that the non-STEM audience is merely lacking sufficient information and facts to make informed decisions, and with increased science literacy, they would make science-based decisions.[71] Two-way, asset-based brings together the expertise and interests of both groups to build a better understanding for all involved.[72] This type of interaction meet audiences where they are at, both in terms of shared interest and sometimes physically, building deeper relationships and trust. The most effective science communication, especially when hoping to change perceptions about specific scientific topics, is done when relationships between scientists and their community are built.[73] Community-engaged learning courses offer a method for the university and its students to serve the community around them, building relationships based on trust and mutual interest, and teaching students how they might serve their communities as future scientists, bringing President Van Hise's Wisconsin Idea to life.

1.5. Scope of Thesis

Carbon coatings provide a versatile handle on the surface control of materials. This thesis looks at the application of carbon coatings in two different systems. In Chapter 2, carbon coatings are used as a method of surface passivation for red phosphorus, suppressing the production of toxic phosphine gas from red phosphorus powders. In the study, through a combination of a novel headspace IR analysis and x-ray photoelectron spectroscopy, we develop a model of red phosphorus degradation to phosphine gas and PO_x species, and how a nano-thin layer of graphitic carbon can suppress that degradation.

In Chapter 3, carbon coatings are used as a stable scaffold for the long-term surface functionalization of metal oxide nanomaterials. The study characterizes a novel carbon coating technique to produce a nano-thin layer of graphitic carbon through the carbonization of fatty acids. This method can be applied to a variety of metal oxide nanomaterials of interest, including fluorescent nanoruby, superparamagnetic iron oxide, and zinc oxide. We then show that this carbon coating can be functionalized with a variety of small molecules through stable, carbon-carbon bonds, producing negatively, neutrally, and positively charged metal oxide nanoparticles that can be used to further understand the interactions of nanomaterials in complex biological systems.

Finally, Chapter 4 introduces and assesses a community-engaged learning undergraduate course offered at the University of Wisconsin-Madison called Service with Youth in STEM. The course teaches students best practices in community engagement, while exemplifying the importance of relationship building and reflection in science communication. Throughout the class, we found that the students also develop a better understanding of their STEM identities, building confidence and a sense of belonging in STEM, potentially increasing retention and engagement of STEM undergraduates in their STEM fields of interest.

1.6. References

1. Hamers, R. J., 2021.
2. Edwards, I. A.; Marsh, H.; Menendez, R., *Introduction to carbon science*. Butterworth-Heinemann: 2013.
3. Dienwiebel, M.; Verhoeven, G. S.; Pradeep, N.; Frenken, J. W.; Heimberg, J. A.; Zandbergen, H. W., Superlubricity of graphite. *Physical review letters* **2004,** *92* (12), 126101.
4. Pierson, H. O., *Handbook of carbon, graphite, diamonds and fullerenes: processing, properties and applications*. William Andrew: 2012.
5. Collins, A. T., The optical and electronic properties of semiconducting diamond. *Philosophical Transactions of the Royal Society of London. Series A: Physical and Engineering Sciences* **1993,** *342* (1664), 233-244.
6. Falcao, E. H.; Wudl, F., Carbon allotropes: beyond graphite and diamond. *Journal of Chemical Technology & Biotechnology: International Research in Process, Environmental & Clean Technology* **2007,** *82* (6), 524-531.
7. Ferrari, A. C.; Robertson, J., Raman spectroscopy of amorphous, nanostructured, diamond–like carbon, and nanodiamond. *Philosophical Transactions of the Royal Society of London. Series A: Mathematical, Physical and Engineering Sciences* **2004,** *362* (1824), 2477-2512.
8. Saroha, R.; Panwar, A. K., Effect of in situ pyrolysis of acetylene (C2 H2) gas as a carbon source on the electrochemical performance of LiFePO4 for rechargeable lithiumion batteries. *Journal of Physics D: Applied Physics* **2017,** *50*, 255501-255501.
9. Heaney, P.; Torres, C.; Sumant, A.; Carpick, R. W.; Pfefferkorn, F., Effect of nanocrystalline diamond coatings on micro-end milling performance. *ICOMM, Urbana, IL* **2006**.
10. Fedel, M., 4 - Blood compatibility of diamond-like carbon (DLC) coatings. In *Diamond-Based Materials for Biomedical Applications*, Narayan, R., Ed. Woodhead Publishing: 2013; pp 71-102.
11. Marcinek, M. L.; Wilcox, J. W.; Doeff, M. M.; Kostecki, R. M., Microwave Plasma Chemical Vapor Deposition of Carbon Coatings on LiNi1/3Co1/3Mn1/3O2 for Li-Ion Battery Composite Cathodes. *Journal of the Electrochemical Society* **2009,** *156* (1), A48-A51.
12. Cui, F. Z.; Li, D. J., A review of investigations on biocompatibility of diamond-like carbon and carbon nitride films. *Surface and Coatings Technology* **2000,** *131* (1), 481-487.

13. Kim, H.-S.; Kong, M.; Kim, K.; Kim, I.-J.; Gu, H.-B., Effect of carbon coating on LiNi1/3Mn1/3Co1/3O2 cathode material for lithium secondary batteries. *Journal of Power Sources* **2007,** *171*, 917-921.
14. Cao, Q.; Zhang, H. P.; Wang, G. J.; Xia, Q.; Wu, Y. P.; Wu, H. Q., A novel carbon-coated LiCoO2 as cathode material for lithium ion battery. *Electrochemistry Communications* **2007,** *9* (5), 1228-1232.
15. Li, H.; Zhou, H., Enhancing the performances of Li-ion batteries by carbon-coating: present and future. *Chemical Communications* **2012,** *48*, 1201-1217.
16. Moskon, J.; Dominko, R.; Cerc-Korosec, R.; Gaberscek, M.; Jamnik, J., Morphology and electrical properties of conductive carbon coatings for cathode materials. *Journal of Power Sources* **2007,** *174* (2), 683-688.
17. Chen, Z.; Qin, Y.; Amine, K.; Sun, Y.-K., Role of surface coating on cathode materials for lithium-ion batteries. *Journal of materials chemistry* **2010,** *20* (36), 7606-7612.
18. Grill, A., Diamond-like carbon coatings as biocompatible materials—an overview. *Diamond and related materials* **2003,** *12* (2), 166-170.
19. Grill, A., Review of the tribology of diamond-like carbon. *Wear* **1993,** *168* (1), 143-153.
20. Carnicer-Lombarte, A.; Chen, S.-T.; Malliaras, G. G.; Barone, D. G., Foreign body reaction to implanted biomaterials and its impact in nerve neuroprosthetics. *Frontiers in Bioengineering and Biotechnology* **2021**, 271.
21. Zhang, Y.; Tamijani, A. A.; Taylor, M. E.; Zhi, B.; Haynes, C. L.; Mason, S. E.; Hamers, R. J., Molecular Surface Functionalization of Carbon Materials via Radical-Induced Grafting of Terminal Alkenes. *Journal of the American Chemical Society* **2019,** *141*, 8277-8288.
22. Whittingham, M. S., Lithium Batteries and Cathode Materials. *Chemical Reviews* **2004,** *104* (10), 4271-4302.
23. Bourzac, K., Quantum dots go on display. *Nature* **2013,** *493* (7432), 283-283.
24. Yetisen, A. K.; Qu, H.; Manbachi, A.; Butt, H.; Dokmeci, M. R.; Hinestroza, J. P.; Skorobogatiy, M.; Khademhosseini, A.; Yun, S. H., Nanotechnology in Textiles. *ACS Nano* **2016,** *10* (3), 3042-3068.
25. Murphy, C. J.; Vartanian, A. M.; Geiger, F. M.; Hamers, R. J.; Pedersen, J.; Cui, Q.; Haynes, C. L.; Carlson, E. E.; Hernandez, R.; Klaper, R. D.; Orr, G.; Rosenzweig, Z. e., Biological Responses to Engineered Nanomaterials: Needs for the Next Decade. *ACS Central Science* **2015,** *1* (3), 117-123.
26. Poole Jr, C. P.; Owens, F. J., *Introduction to nanotechnology*. John Wiley & Sons: 2003.
27. Hamers, R. J., Nanomaterials and Global Sustainability. *Accounts of Chemical Research* **2017,** *50* (3), 633-637.
28. Grassian, V. H.; Haes, A. J.; Mudunkotuwa, I. A.; Demokritou, P.; Kane, A. B.; Murphy, C. J.; Hutchison, J. E.; Isaacs, J. A.; Jun, Y.-S.; Karn, B., NanoEHS–defining fundamental science needs: no easy feat when the simple itself is complex. *Environmental Science: Nano* **2016,** *3* (1), 15-27.

29. Christian, P.; Von der Kammer, F.; Baalousha, M.; Hofmann, T., Nanoparticles: structure, properties, preparation and behaviour in environmental media. *Ecotoxicology* **2008,** *17* (5), 326-343.

30. Hotze, E. M.; Phenrat, T.; Lowry, G. V., Nanoparticle aggregation: challenges to understanding transport and reactivity in the environment. *Journal of environmental quality* **2010,** *39* (6), 1909-1924.

31. Laudadio, E. D.; Bennett, J. W.; Green, C. M.; Mason, S. E.; Hamers, R. J., Impact of Phosphate Adsorption on Complex Cobalt Oxide Nanoparticle Dispersibility in Aqueous Media. *Environmental Science & Technology* **2018,** *52* (17), 10186-10195.

32. Feng, Z. V.; Gunsolus, I. L.; Qiu, T. A.; Hurley, K. R.; Nyberg, L. H.; Frew, H.; Johnson, K. P.; Vartanian, A. M.; Jacob, L. M.; Lohse, S. E., Impacts of gold nanoparticle charge and ligand type on surface binding and toxicity to Gram-negative and Gram-positive bacteria. *Chemical science* **2015,** *6* (9), 5186-5196.

33. Lochbaum, C. A.; Chew, A. K.; Zhang, X.; Rotello, V.; Van Lehn, R. C.; Pedersen, J. A., Lipophilicity of Cationic Ligands Promotes Irreversible Adsorption of Nanoparticles to Lipid Bilayers. *ACS Nano* **2021,** *15* (4), 6562-6572.

34. Henke, A. H.; Laudadio, E. D.; Orbeck, J. K. H.; Tamijani, A. A.; Hoang, K. N. L.; Mason, S. E.; Murphy, C. J.; Feng, Z. V.; Hamers, R. J., Reciprocal redox interactions of lithium cobalt oxide nanoparticles with nicotinamide adenine dinucleotide (NADH) and glutathione (GSH): toward a mechanistic understanding of nanoparticle-biological interactions. *Environmental Science: Nano* **2021,** *8* (6), 1749-1760.

35. Reineck, P.; Gibson, B. C., Near-infrared fluorescent nanomaterials for bioimaging and sensing. *Advanced Optical Materials* **2017,** *5* (2), 1600446.

36. Reineck, P.; Francis, A.; Orth, A.; Wai Mo Lau, D.; David Valmont Nixon-Luke, R.; Das Rastogi, I.; Aizuddin Wan Razali, W.; Maree Cordina, N.; Marie Parker, L.; Kumaraswamy Annayya Sreenivasan, V.; Jennifer Brown, L.; Cameron Gibson, B., Brightness and Photostability of Emerging Red and Near-IR Fluorescent Nanomaterials for Bioimaging. *Advanced Optical Materials* **2016,** *4*, 1549-1557.

37. Mochalin, V. N.; Shenderova, O.; Ho, D.; Gogotsi, Y., The properties and applications of nanodiamonds. *Nature Nanotechnology* **2012,** *7* (1), 11-23.

38. Jones, Z. R.; Niemuth, N. J.; Zhang, Y.; Protter, C. R.; Kinsley, P. C.; Klaper, R. D.; Hamers, R. J., Use of Magnetic Modulation of Nitrogen-Vacancy Center Fluorescence in Nanodiamonds for Quantitative Analysis of Nanoparticles in Organisms. *ACS Measurement Science Au* **2022**.

39. Hsiao, W. W.-W.; Yung Hui, Y.; Tsai, P.-C.; Chang, H.-C., Fluorescent Nanodiamond: A Versatile Tool for Long-Term Cell Tracking, Super-Resolution Imaging, and Nanoscale Temperature Sensing. *Accounts of Chemical Research* **2016,** *49*, 400-407.

40. Jones, Z. R.; Niemuth, N. J.; Robinson, M. E.; Shenderova, O. A.; Klaper, R. D.; Hamers, R. J., Selective imaging of diamond nanoparticles within complex matrices using magnetically induced fluorescence contrast. *Environmental Science: Nano* **2020,** *7* (2), 525-534.

41. Edmonds, A. M.; Sobhan, M. A.; Sreenivasan, V. K.; Grebenik, E. A.; Rabeau, J. R.; Goldys, E. M.; Zvyagin, A. V., Nano-ruby: a promising fluorescent probe for background-free cellular imaging. *Particle & Particle Systems Characterization* **2013,** *30* (6), 506-513.
42. Seat, H. C.; Sharp, J. H., Dedicated temperature sensing with c-axis oriented single-crystal ruby (Cr/sup 3+/:Al/sub 2/O/sub 3/) fibers: temperature and strain dependences of R-line fluorescence. *IEEE Transactions on Instrumentation and Measurement* **2004,** *53* (1), 140-154.
43. Wheeler, K. E.; Chetwynd, A. J.; Fahy, K. M.; Hong, B. S.; Tochihuitl, J. A.; Foster, L. A.; Lynch, I., Environmental dimensions of the protein corona. *Nature Nanotechnology* **2021,** *16* (6), 617-629.
44. Borgatta, J. R.; Lochbaum, C. A.; Elmer, W. H.; White, J. C.; Pedersen, J. A.; Hamers, R. J., Biomolecular corona formation on CuO nanoparticles in plant xylem fluid. *Environmental Science: Nano* **2021,** *8* (4), 1067-1080.
45. Richtering, W.; Alberg, I.; Zentel, R., Nanoparticles in the biological context: surface morphology and protein corona formation. *Small* **2020,** *16* (39), 2002162.
46. Tenzer, S.; Docter, D.; Kuharev, J.; Musyanovych, A.; Fetz, V.; Hecht, R.; Schlenk, F.; Fischer, D.; Kiouptsi, K.; Reinhardt, C.; Landfester, K.; Schild, H.; Maskos, M.; Knauer, S. K.; Stauber, R. H., Rapid formation of plasma protein corona critically affects nanoparticle pathophysiology. *Nature Nanotechnology* **2013,** *8* (10), 772-781.
47. Xie, C.; Zhang, J.; Ma, Y.; Ding, Y.; Zhang, P.; Zheng, L.; Chai, Z.; Zhao, Y.; Zhang, Z.; He, X., Bacillus subtilis causes dissolution of ceria nanoparticles at the nano–bio interface. *Environmental Science: Nano* **2019,** *6* (1), 216-223.
48. Albanese, A.; Walkey, C. D.; Olsen, J. B.; Guo, H.; Emili, A.; Chan, W. C. W., Secreted Biomolecules Alter the Biological Identity and Cellular Interactions of Nanoparticles. *ACS Nano* **2014,** *8* (6), 5515-5526.
49. Capriotti, A. L.; Caracciolo, G.; Cavaliere, C.; Colapicchioni, V.; Piovesana, S.; Pozzi, D.; Laganà, A., Analytical Methods for Characterizing the Nanoparticle–Protein Corona. *Chromatographia* **2014,** *77* (11), 755-769.
50. Hoang, K. N. L.; Wheeler, K. E.; Murphy, C. J., Isolation Methods Influence the Protein Corona Composition on Gold-Coated Iron Oxide Nanoparticles. *Analytical Chemistry* **2022,** *94* (11), 4737-4746.
51. Neouze, M.-A.; Schubert, U., Surface Modification and Functionalization of Metal and Metal Oxide Nanoparticles by Organic Ligands. *Monatshefte für Chemie - Chemical Monthly* **2008,** *139*, 183-195.
52. Servin, A.; Elmer, W.; Mukherjee, A.; De la Torre-Roche, R.; Hamdi, H.; White, J. C.; Bindraban, P.; Dimkpa, C., A review of the use of engineered nanomaterials to suppress plant disease and enhance crop yield. *Journal of Nanoparticle Research* **2015,** *17* (2), 92.
53. Rodrigues, S. M.; Demokritou, P.; Dokoozlian, N.; Hendren, C. O.; Karn, B.; Mauter, M. S.; Sadik, O. A.; Safarpour, M.; Unrine, J. M.; Viers, J., Nanotechnology for sustainable food production: promising opportunities and scientific challenges. *Environmental Science: Nano* **2017,** *4* (4), 767-781.

54. Savary, S.; Ficke, A.; Aubertot, J.-N.; Hollier, C., Crop losses due to diseases and their implications for global food production losses and food security. *Food Security* **2012,** *4* (4), 519-537.

55. Singh, A.; Singh, N. B.; Afzal, S.; Singh, T.; Hussain, I., Zinc oxide nanoparticles: a review of their biological synthesis, antimicrobial activity, uptake, translocation and biotransformation in plants. *Journal of Materials Science* **2018,** *53* (1), 185-201.

56. Nunes, I.; Jacquiod, S.; Brejnrod, A.; Holm, P. E.; Johansen, A.; Brandt, K. K.; Priemé, A.; Sørensen, S. J., Coping with copper: legacy effect of copper on potential activity of soil bacteria following a century of exposure. *FEMS Microbiology Ecology* **2016,** *92* (11), fiw175.

57. Hoang, T. C.; Rogevich, E. C.; Rand, G. M.; Gardinali, P. R.; Frakes, R. A.; Bargar, T. A., Copper desorption in flooded agricultural soils and toxicity to the Florida apple snail (Pomacea paludosa): Implications in Everglades restoration. *Environmental Pollution* **2008,** *154* (2), 338-347.

58. Borgatta, J.; Ma, C.; Hudson-Smith, N.; Elmer, W.; Plaza Pérez, C. D.; De La Torre-Roche, R.; Zuverza-Mena, N.; Haynes, C. L.; White, J. C.; Hamers, R. J., Copper Based Nanomaterials Suppress Root Fungal Disease in Watermelon (Citrullus lanatus): Role of Particle Morphology, Composition and Dissolution Behavior. *ACS Sustainable Chemistry & Engineering* **2018,** *6* (11), 14847-14856.

59. Ma, C.; Borgatta, J.; Hudson, B. G.; Tamijani, A. A.; De La Torre-Roche, R.; Zuverza-Mena, N.; Shen, Y.; Elmer, W.; Xing, B.; Mason, S. E.; Hamers, R. J.; White, J. C., Advanced material modulation of nutritional and phytohormone status alleviates damage from soybean sudden death syndrome. *Nature Nanotechnology* **2020,** *15* (12), 1033-1042.

60. Deng, C.; Wang, Y.; Cantu, J. M.; Valdes, C.; Navarro, G.; Cota-Ruiz, K.; Hernandez-Viezcas, J. A.; Li, C.; Elmer, W. H.; Dimkpa, C. O.; White, J. C.; Gardea-Torresdey, J. L., Soil and foliar exposure of soybean (Glycine max) to Cu: Nanoparticle coating-dependent plant responses. *NanoImpact* **2022,** *26*, 100406.

61. Van Hise, C., Address before the Press Association. Madison, WI, 1905.

62. McCarthy, C., *The Wisconsin Idea*. MacMillan Company: New York, 1912.

63. Stark, J. O., The Wisconsin Idea: The university's service to the state. **1995**.

64. What is community-based learning? https://www.colorado.edu/cuengage/about-us/what-community-based-learning.

65. Furco, A., Service-learning: A balanced approach to experiential education. **1996**.

66. Sithole, A.; Chiyaka, E. T.; McCarthy, P.; Mupinga, D. M.; Bucklein, B. K.; Kibirige, J., Student Attraction, Persistence and Retention in STEM Programs: Successes and Continuing Challenges. *Higher Education Studies* **2017,** *7* (1), 46-59.

67. Flener-Lovitt, C., Using the Socioscientific Context of Climate Change To Teach Chemical Content and the Nature of Science. *Journal of Chemical Education* **2014,** *91* (10), 1587-1593.

68. Drury, B. J.; Siy, J. O.; Cheryan, S., When Do Female Role Models Benefit Women? The Importance of Differentiating Recruitment From Retention in STEM. *Psychological Inquiry* **2011,** *22* (4), 265-269.

69. Tomasko, D. L.; Ridgway, J. S.; Waller, R. J.; Olesik, S. V., Association of Summer Bridge Program Outcomes With STEM Retention of Targeted Demographic Groups. *Journal of College Science Teaching* **2016,** *45* (4).

70. Najmr, S.; Chae, J.; Greenberg, M. L.; Bowman, C.; Harkavy, I.; Maeyer, J. R., A Service-Learning Chemistry Course as a Model To Improve Undergraduate Scientific Communication Skills. *Journal of Chemical Education* **2018,** *95* (4), 528-534.

71. Nadkarni, N. M.; Weber, C. Q.; Goldman, S. V.; Schatz, D. L.; Allen, S.; Menlove, R., Beyond the Deficit Model: The Ambassador Approach to Public Engagement. *BioScience* **2019,** *69* (4), 305-313.

72. Fogg-Rogers, L.; Bay, J. L.; Burgess, H.; Purdy, S. C., "Knowledge Is Power" A Mixed-Methods Study Exploring Adult Audience Preferences for Engagement and Learning Formats Over 3 Years of a Health Science Festival. *Science Communication* **2015,** *37* (4), 419-451.

73. Hayhoe, K., When facts are not enough. American Association for the Advancement of Science: 2018; Vol. 360, pp 943-943.

Chapter 2: Reactivity passivation of red phosphorus with thin plasma-deposited carbon coating

The following chapter is adapted from the article published in *Applied Surface Science,* **2022** *587*, (DOI: 10.1016/j.apsusc.2022.152791), with the co-authors Aiping Zeng, Jenny K. Hedlund Orbeck, Shaun Debow, Zachary B. Zander, Patrick J. Heaney, Robert J. Hamers

All of the experiments, data acquisition and analysis, and manuscript preparation and revision were done by Paige C. Kinsley under the advisement of Robert J. Hamers expect for the following:

Aiping Zeng carbon coated the red phosphorus particles using a plasma source ion immersion implantation and deposition process designed by Patrick J. Heaney. Jenny K. Hedlund Orbeck made intellectual contributions to XPS analysis. Shaun Debow and Zachary B. Zander contributed to conceptualization of project.

2.1 Introduction

Red phosphorus (RP) is a phosphorus allotrope commonly used as a flame retardant in thermoplastics and as an obscurant to attenuate transmission in visible and IR regions in military applications [1]. It has also been used in composites for anodes for sodium ion batteries [2]. While its chemical properties make it well suited for these applications, its reactivity with water and oxygen is an obstacle for safe use. When red phosphorus reacts with water, it evolves phosphine (PH_3), a highly toxic gas even at low levels, and acidic phosphorus species, primarily phosphoric and phosphorous acids [3-5]. Formation and accumulation of phosphine due to storage conditions of red phosphorus can potentially lead to human health hazards because of the high toxicity of phosphine. Further decomposition can form phosphorous and phosphoric acids on surfaces, leading to corrosion and failure of components or electronic connections [6-8]. To mitigate degradation of red phosphorus, some manufacturers have added in components that sequester phosphine as it is generated or neutralizes acid species using alkaline compounds [1, 9, 10]. Alternatively, red phosphorus can be mixed with amides and ester-based polymers to protect the surface of the phosphorus particles from direct contact with water or air. However, these polymer coatings are less effective at suppressing phosphine formation at elevated temperatures. Furthermore, phosphorus must be burned when used as a smoke obscurant, and these coatings produce toxic carbon-based byproducts under these conditions. [1, 11]. Additionally, many additives require a high additive-to-red-phosphorus ratio to be effective, decreasing the amount of active species by mass.

An alternative approach to mitigating the reactivity of phosphorus is coating the individual phosphorus particles with a thin protective layer, forming a core-shell structure. Carbon coatings are chemically and thermally stable [12] and have been successfully used in the battery industry as a way to improve electrical properties for active anode and cathode powders, reducing reactivity with liquid electrolytes [13]. Additionally, we predict these thin carbon coatings will not impact desired red phosphorus combustion properties because of their small heat capacity compared to polymer counterparts. While carbon coatings can be applied using several approaches [14-16], plasma deposition methods can be applied to both planar and powder samples and can be scaled up to kilogram ranges [17, 18]. The resulting layers can be conformal, with controlled thickness and are typically hydrophobic, thereby resisting entrapment of water in powdered samples.

Here, we report an investigation of the surface transformations of red phosphorus with water vapor. Using a combination of gas-phase infrared spectroscopy (IR) and x-ray photoelectron spectroscopy (XPS), we demonstrate the ability to characterize and quantify red phosphorus transformation as it ages, as well as the impact of plasma-deposited carbon surface coatings on the transformation. Tracking PH_3 generation by IR and oxidized phosphorus species production by XPS and IR, we gain insight into how RP degrades as it ages in humid environments. This study provides insight into the efficacy of plasma-deposited carbon on passivation of RP as well as building a picture of the mechanism of RP degradation.

2.2. Materials and methods

2.2.3. Materials

Red phosphorus (Manufacturer: <100 μm, 98%, MIL DTL 211 F Class 4) was purchased from Italmatch Chemicals. Zinc sulfide (10 μm, 99.99% trace metals basis), zinc phosphide (≥19% active phoshor (P) basis, powder), sodium hydroxide (ACS reagent, ≥97.0%, pellets), and hydrochloric acid (ACS reagent, 37%) were all purchased from Sigma Aldrich. Acetylene (99.6%) was purchased from Airgas. Aging conditions for red phosphorus and titrations were done using ultrapure water (18.2 MΩ).

2.2.4. Red phosphorus preparation and plasma-deposited carbon (PDC) coating

Red phosphorus particles were cleaned and coated using a plasma source ion immersion implantation and deposition process with a pulsed DC power supply. The apparatus used for carbon coating is similar to deposition systems reported previously. [19, 20]. Specifically, we employed a rotating cathodic plasma tank installed at NCD Technologies. The RP particles were first dried in vacuum to remove adsorbed moisture, and then cleaned using an argon/hydrogen plasma followed by an argon plasma. Following plasma cleaning, cathodic plasma tank parameters are adjusted to deposit a carbon coating on the RP particles using an acetylene precursor gas. The plasma tank design allows for ball milling during plasma cleaning and carbon deposition to further separate RP clumps and reduce particle size to avoid particle aggregation during carbon deposition. The PDC deposition times were 0, 4, 8, and 24 min/g, where the exposure to the plasma was normalized by the mass of RP sample in the reactor to help compensate for differences in surface coverage due to slightly varying amounts of phosphorus. Samples will be referred to RP-uncoated (0 min/g) and for coated red phosphorus, RP@C-short (4 min/g), RP@C-medium (8 min/g), and RP@C-long (24 min/g) throughout the paper. Specifics on flow rate and reactor set up can be found in a patent soon to be published.

2.2.5. Characterization of non-aged red phosphorus particles

Scanning electron microscopy (SEM) measurements were taken on a Leo Supra55 VP SEM at 1 kV using a secondary electron detector. SEM samples were prepared by making a red phosphorus and isopropyl alcohol solution that was then drop-cast on a boron-doped silicon wafer. To prepare samples for surface area characterization using Brunauer-Emmet-Teller (BET) analysis, ~170 mg of sample was weighed and degassed at 120°C for 2 hours under vacuum. Samples were analyzed using a Micrometrics Gemeni VII 2390 surface analyzer, measuring nitrogen absorption isotherms. BET analysis gave an average particle size on the order of several microns, and SEM showed a broad distribution of sizes. Raman measurements were taken using a Thermo-Fischer Scientific DXRxi Raman imaging microscope using 532 nm laser excitation at 2 mW power and 10x objective. Samples were prepared as described in section 2.2.6 (using the same preparation as XPS samples).

2.2.6. Gas-phase infrared spectroscopy

Gas-phase infrared (IR) spectra were collected using a Bruker Vertex 70 spectrometer at a resolution of 0.5 cm^{-1} and collected from 5000 to 700 cm^{-1}, with 100 scans per spectrum. Spectra were collected in a transmission geometry with a 10 cm path length (see Figure A2.1 for gas phase IR cell dimensions). For each phosphine generation experiment, 0.500 g of red phosphorus was added to one sample bulb (Figure A.2.1b) and 1.000 mL of nanopure water to the other. After sealing bulbs onto cell with vacuum grease and parafilm, a 0-hour baseline spectrum was taken for each sample using the above instrument parameters. The cells were then stored in an incubator at 50°C between time points. To prevent accumulation of water condensation on the red phosphorus particles, the cells were stored in a custom-made aluminum holder and tilted at an angle (see Figure A.2.1c). Three replicates for each sample were measured for statistical analysis.

For experimental phosphine calibration of IR instrument, zinc phosphide powder was dissolved in 5N hydrochloric acid to produce pure phosphine gas. A gas tube, filled with HCl and capped with a septum, was used to collect PH_3 bubbles produced by dissolving zinc phosphide. A known volume of PH_3 was collected by syringe and transferred to a septum-capped gas phase IR cell filled with air at atmosphere. Spectra were measured using the same instrument parameters as gas-phase IR PH_3 experiments with red phosphorus.

2.2.7. Diffuse reflectance infrared spectroscopy

Diffuse reflectance infrared spectroscopy (DRIFTS) spectra were collected using a Bruker Vertex 70 at a resolution of 4 cm^{-1} and collected between 5000 to 700 cm^{-1}, with 500 scans collected each spectrum. Uncoated red phosphorus was mixed with dry zinc sulfide at a 1:100 mass ratio and placed in to a Praying Mantis^{TM} High Temperature Reaction Chamber, which provides a hermetically sealed environment for gas-solid interactions. The RP/ZnS sample was added to the chamber along with 0.800 mL of nanopure water, and the chamber was then sealed. After taking a spectrum at 0 hours, the reaction chamber was stored at 50°C for 24 hours and another spectrum was taken for comparison.

2.2.8. X-ray photoelectron spectroscopy

X-ray photoelectron spectroscopy (XPS) data were obtained on a Thermo K-alpha XPS using an Al Kα source (1486.6 eV photon energy) at a 45° take-off angle. Survey spectra were taken at a pass energy of 200 eV and resolution of 1 eV/step. For the C(1s), P(2p), and O(1s) peaks, we used a 50 eV pass energy and 0.200 eV/step resolution. Data were analyzed using CasaXPS; peak-fitting was performed using a Shirley background fit and a GL(30) mixed Gaussian-Lorentzian line shape [21]. All energies were calibrated to the 284.8 eV binding energy of adventitious carbon [22].

Samples were prepared by pressing sample powder into indium foil mounted on a copper substrate. To remove any residual moisture, aged samples from gas-phase IR experiments were first dried in a vacuum oven at 35°C for 2 hours before pressing. Three replicates were taken for statistical analysis, with three points taken per replicate.

To calculate the carbon thickness for each deposition rate, we used a model that includes the influence of electron scattering within the phosphorus and within the graphite layer, as reported previously [23].

$$\frac{1-e^{-t_c/\lambda_{C1s,graphite}}}{e^{-t_c/\lambda_{P2p,graphite}}}=\frac{Area_{C1s}}{Area_{P2p}}\cdot\frac{\rho_P}{\rho_C}\cdot\frac{SF_{P2p}}{SF_{C1s}}\cdot\frac{\lambda_{P2p,Red\,P}}{\lambda_{C1s,graphite}} \quad (2.1)$$

Where t_c = carbon coating thickness in nm, *Area* = integrated peak area, ρ = density of element in atoms/nm^3 (ρ_p = 42 atoms/nm^3 for P in red phosphorus, ρ_C = 130.5 atoms/nm^3 for C in amorphous carbon [24]), *SF* = elemental sensitivity factor ($SF_{P(2p)}$ = 1.3529, $SF_{C(1s)}$ = 1), $\lambda_{A,B}$ represents the inelastic mean free path of electrons "A" through the material "B". We used $\lambda_{P2p,\ Red\ P}$ = 2.90 nm, $\lambda_{P2p,\ graphite}$ = 1.99 nm, and $\lambda_{C1s,\ graphite}$ = 1.81 nm (based on calculations using the NIST Electron Inelastic-Mean-Free-Path Database [25]). This equation cannot be solved analytically but can be solved numerically or graphically to determine the carbon layer thickness t_c [26].

The atomic percent of specific species in the region probed by XPS was calculated using the following equation:

$$Atomic\ \% = 100 * \frac{\frac{Area_A}{N_A SF_A}}{\frac{Area_A}{N_A SF_A}+\frac{Area_B}{N_B SF_B}} \quad (2.3)$$

Where *Area* = integrated peak area, *SF* = elemental sensitivity factor ($SF_{P(2p)}$ = 1.3529, $SF_{C(1s)}$ = 1) and *N* = number of summed sweeps acquired for a specific element.

To calculate the percent oxidized phosphorus composition based on P(2p) emission intensity, we used equation 2.4:

$$PO_x\%\ of\ P(2p) = \frac{Area_{PO4}}{Area_{PO4} + Area_{Elemental\ P,corrected}} * 100 \qquad (2.4)$$

See Appendix 2 for equation and explanation for corrected elemental P area in equation 2.4.

2.2.9. Acid-base titration

To quantify the acid species adsorbed to the surface of red phosphorus particles after aging for gas-phase IR data collection, each RP specimen was suspended in its corresponding 1.000 mL of water used in the gas-phase IR experimental methods section (from the water bulb in Figure A.2.1) and centrifuged at 14,500x rpm for 5 min. The supernatant was then taken, diluted to 10.0 mL, and titrated with 37.60 mL of 0.0100 M NaOH to determine the identity and concentration of phosphorus acid species.

2.3. Results and discussion

2.3.1. Influence of carbon coating on particle properties

Before testing the efficacy of the carbon coating on the suppression of red phosphorus transformations, we characterized the effect of carbon deposition time on carbon composition and coverage. Increasing carbon deposition affected both the size and surface area of the particles. Figure A.2.2 shows increasing deposition time corresponds to an increase in surface area, as measured by BET surface area analysis. Specifically, the surface area of the particles increased 10-fold from uncoated particles (0 min) compared with particles coated for the longest deposition time, at 24 min. To understand the origin of this increase, particles were imaged using scanning electron microscopy (Figure 2.1a and 2.1b and Figure A.2.3). Because the secondary electron (SE) yield of phosphorus is greater than carbon, phosphorus appears brighter in SEM images, providing a way to distinguish between carbon and phosphorus. Based on the examination of many images, we observe that particle appearances changes with increasing deposition time. Specifically, uncoated particles appear smooth with high SE yield, while RP@C-long have a rougher surface with lower SE yield. This suggests that, with increasing deposition time, smoother phosphorus is covered with rougher carbon. Compared to the relatively smooth surface of uncoated red phosphorus, the carbon coating is rough at the submicron scale, leading to a further increase in surface area of each particle, corresponding to BET surface area analysis data.

While SEM shows that the coating appears particle-like, we used Raman to identify the nature of the carbon coating. Uncoated RP particles show strong phosphorus bands between 300-500 cm^{-1} (Figure 2.1c) [27]. As the duration of carbon deposition increases, the phosphorus bands at 350 cm^{-1}, 396 cm^{-1}, and 444 cm^{-1} decrease in intensity (for RP@C-short) and then disappear (for RP@C-long), while new bands arise near 1385 cm^{-1} and 1586 cm^{-1}. Bands in this region are well known and are frequently referred to as the D band and G band, respectively [28, 29]. Ferrari and Robertson introduced a three-stage model of carbon ordering (transitioning from graphite to tetrahedral amorphous carbon) based on the Raman shift of the G band and the ratio of intensities I(D)/I(G) [29]. Our measurements (Table A.2.1) show that regardless of PDC deposition time, the G band remains between 1585-1590 cm^{-1} and the I(D)/I(G) remains approximately 0.45. These results correspond to stage 1 carbon, indicating more graphite than nanocrystalline graphite on the surface with mostly sp^2 hybridization, and no measurable presence of amorphous carbon [29]. Characterization of the pristine carbon coating can provide insight into the passivation of the red phosphorus surface.

We quantified PH_3 generation using infrared analysis of phosphine generated from red phosphorus samples. Two PH_3 vibrational bands are conveniently located in mid-infrared regions and do not overlap with CO_2, H_2O, or other infrared-active contaminants. The PH_3 □$_2$ band is centered near 992.1 cm^{-1} and the υ_4^1 band is centered at 1118.3 cm^{-1} [30, 31]. Due to its odd number of electrons, PH_3 has allowed Q branch transitions (e.g., □J=0), leading to a strong, slightly broad peak centered at each band head, along with sharper but weaker lines due to P (□J=-1) and R (□J=+1) transitions in the adjacent regions. A sealed IR cell allowed us to intentionally expose red phosphorus to high temperature, high humidity environments while safely measuring PH_3 generation over time. To establish how the amount of phosphine produced depends on aging conditions, we acquired spectra every 12 hours for 48 hours. Figure 2.2a shows typical phosphine spectra for uncoated RP particles aged over 48 hours. Using the linear calibration curve in Figure A.2.4, we quantified the amount of PH_3 by comparing the peak intensity of the υ_4^1 band at 1118.3 cm^{-1} of the uncoated and coated red phosphorus samples, seen in Figure 2.2c at the 48-hour timepoint, to the peak intensities measured for samples of dilute PH_3 gas. We further verified the validity of our calibration by comparing integrated absorption intensities of our self-generated calibrations with integrated absorbance values of individual infrared transitions at 944.4 cm^{-1}, published previously [30, 31].

To determine the impact of the plasma-deposited carbon coating on the suppression of phosphine generation, RP samples that were exposed to the plasma for increasing lengths of time were aged for 48 h (100% humidity, 50°C). Figure 2.2b shows the resulting spectra. Figure 2.2b and 2c shows that the samples exposed to the DC plasma for greater lengths of time produced less PH_3, and the sample having the longest exposure (RP@C-long) showed no detectable PH_3 generation after 48 hours of aging.

We converted the IR absorbance values to PH_3 volume percent, giving the result shown in Figure 2.3. While the cumulative amount of PH_3 formed continually increases as the samples are aged, the rate of PH_3 formation appears to decrease at longer aging times. Table 2.1 shows the initial PH_3 generation rate, obtained from the initial slope between 0 and 12 hours of the data in Figure 2.3. With increasing deposition time, both the initial rate of PH_3 generation and the final amount of PH_3 generated are suppressed. Increasing deposition of plasma-deposited carbon coating suppresses generation of phosphine as measured by infrared spectroscopy.

2.3.2. Surface analysis of non-aged red phosphorus samples

XPS measurements provided useful information to show how RP particle surface chemistry was altered as an effect of coating and aging. Given that the phosphine generation from coated particles is significantly suppressed with the carbon coating, we first characterized the surface of non-aged particles using XPS to understand the starting surface chemistry of each sample.

Figure 2.4a and 2.4b show the effect of deposition time on C(1s) and P(2p) intensities for non-aged samples. Figure 2.4a shows that as the absolute intensity for C(1s) increases, the intensity of the P(2p) intensity decreases, indicating attenuation of phosphorus by a carbon coating. Figure A.2.5 shows a corresponding decrease in the O(1s) and Na(1s) regions, as the cleaning and then carbon coating treatments remove sodium and oxygen species left from RP synthesis [3]. We attribute carbon present on the uncoated particles to contaminants adsorbed from the environment (frequently referred to as "adventitious carbon"). We anticipate that surface contaminants are likely removed during the plasma deposition process such that their presence on the uncoated particles should not interfere with the intentional formation of carbon coatings or subsequent measurements on carbon-coated powders. We have calculated the apparent thickness of the plasma-deposited carbon on the red phosphorus particles by applying equation 2.1. Figure 2.4b shows the carbon thickness obtained from samples exposed to the PCD for different lengths of time. These data show that a carbon coating of only ~ 8 nm thick on average can almost completely suppress the production of PH_3 based on calculated PH_3 volumes in Figure 2.3. Increasing the PDC coating rate does not correspond to linear increase of apparent thickness of carbon on red phosphorus surface but does follow a trend of PH_3 suppression with increasing carbon thickness.

2.3.3. Evolution of phosphorus chemical state

Prior studies have shown that reduction of P to produce PH_3 is accompanied by oxidation to form different phosphate and phosphonate species [3]. To probe the transformations of red phosphorus after being exposed to the high humidity, high temperature conditions used for the phosphine generation IR experiments, we used XPS to probe the P(2p) region of samples aged at 50°C for 48 hours.

Figure 2.5a and 2.5b show the changes in the P(2p) and C(1s) regions as an effect of 48 hours of aging for uncoated particles and particles coated over the “short” time period (RP@C-short). The P(2p) region shows that before aging, the elemental P peak (130.2 eV) is larger for uncoated RP. After aging for 48 hours, the elemental peak decreases, while the peak corresponding to oxidized phosphorus species at 134.3 eV grows for both samples. Figure 2.5b shows a decrease in the C(1s) peak height for both uncoated and coated particles after aging.

To quantify these changes in relative species abundance, we used equation 2.3 to calculate the atomic percentage of the probed region for carbon, elemental phosphorus, and oxidized phosphorus (PO_x species). Figure 2.5c shows the changes in the atomic percent of each species as a function of deposition time for both non-aged and aged red phosphorus particles. Focusing first on non-aged samples, we see the surface composition increase from roughly 50% carbon on uncoated particles to 99.0±0.3% for particles coated for the longest period of time. The increase in carbon corresponds to a decrease in phosphorus, which is mostly made up of elemental P species for non-aged samples regardless of carbon deposition time. After aging, the atomic percent of carbon decreases for all samples, but most substantially for RP@C-short, decreasing from 87.1±2.1%C to 74.8±1.5%C (all values presented in Table A.2.2). The decrease in atomic percent of carbon corresponds to only a slight increase in elemental phosphorus signal but a significant increase in PO_x signal for all aged samples. This indicates that the decrease in carbon signal is due to attenuation from a PO_x top layer, instead of the removal of carbon coating due to particle aging. While there is some formation of new PO_x species on the surface for all aged samples, for RP@C particles with the longest deposition time, only 2.0±0.9% of the elemental species in the analyzed region can be attributed to the PO_x species, compared to 24.8±3.7%PO_x for the uncoated sample. Analysis of the atomic percent composition indicates that longer carbon deposition times reduce the formation a PO_x top layer on the carbon coating, indicated by the larger attenuation of the carbon signal and an increase in PO_x signal in the P(2p) region for RP@C-short.

To first understand oxidation of the phosphorus surface, we quantified the percentage of P(2p) signal arising from oxidized phosphorus using equation 2.4. Using the adjusted area (equation A.2.2), we normalize out any attenuation of the elemental phosphorus signal (130 eV) by the carbon coating. Figure 2.6a presents the impact of both aging and PDC deposition time on the PO_x composition measured using changes in the P(2p) region seen in Figure 2.5a. For non-aged samples, uncoated red phosphorus starts with more phosphate on the surface compared with samples that were carbon coated. As the deposition time increases, the initial phosphate on the surface decreases from 14±3% (RP-uncoated, non-aged) to 1.7±0.4% (RP@C-long, non-aged), indicating a level of protection that is only made more apparent after aging at 50°C for 48 hours.

For uncoated aged RP, almost 50% of the phosphorus probed by XPS is oxidize phosphorus, while for RP@C-long, only 6.5±2.3% of the P(2p) region is attributed to oxidized species. All samples show a 3-4x increase in phosphate compared to non-aged. After aging in the IR cell, all samples show increased oxidized phosphorus on the surface, but PDC coated particles show suppression of the PO_x signal.

To understand the type of oxidized phosphorus on the surface of the particles, we investigated both the shifts in PO_x P(2p) binding energy and the ratio of O(1s) to PO_x P(2p) XPS intensities. As previously mentioned, after particles are aged, a distinct peak emerges at 134.2 eV (Figure 2.5a). This binding energy aligns with PO_3-containing compounds [32]. Additional confirmation of the phosphorus oxide species on the red phosphorus surface was provided by comparing the relationship of oxygen on the surface from the O(1s) region to the PO_x species on the surface from the P(2p) region. After taking the integrated area of O(1s) and the integrated area of the peak at ~134 eV of the P(2p) region, points for both non-aged and aged samples were graphed. Shown in Figure 2.6b, a slope of 3.04 was found, indicating the ratio of oxygen to phosphorus in PO_x form on the surface is 3:1, the ratio of phosphonate. XPS binding energy shifts in P(2p) region and oxygen-to-PO_x ratio indicates that the phosphorus oxide species is phosphonic acid and its derivatives.

Diffuse reflectance infrared spectroscopy was used to obtain a more comprehensive understanding of oxidized phosphorus species formed in situ during the aging process. Figure 2.7 shows IR spectra for uncoated red phosphorus suspended in zinc sulfide before and after aging for 24 hours. The non-aged sample does not show peaks in the phosphate region of the spectrum (below 1300 cm^{-1}). However, after aging at 50°C and 100% humidity, peaks grow in between 700-1200 cm^{-1} along with a strong peak at 1653 cm^{-1}, which can be attributed to OH deformation vibrations [33]. The peaks between 900-1200 cm^{-1} indicate the presence of both phosphoric acid (H_3PO_4) and phosphonic acid (H_3PO_3). The peak at 1135.1 cm^{-1} is attributed to P=O stretch for phosphonic acid in which an OH is replaced with an R group, likely P on the red phosphorus surface [34]. The peak at 1092.7 cm^{-1} is also attributed to a P=O stretch, but for that of phosphoric acid [34, 35]. The peak at 1010.7 cm^{-1} is also evidence for phosphoric acid on the surface, corresponding to the asymmetric P-O-(H) stretch for H_3PO_4 [36, 37]. Finally, the peak at 950.9 cm^{-1} signals a P-O-(H) stretch for phosphonic acid [36]. The DRIFTS spectrum of aged red phosphorus indicates the production of phosphoric acid and phosphonic acid on the surface.

While gas-phase IR can quantify the amount of PH_3 produced, we used acid-base titration to quantify the acid species that are also produced during the reaction. Figure 2.8a shows the titration curve obtained by extracting the supernatant from aged uncoated RP and titrating with NaOH, revealing two clear equivalence points. Taking the derivative of the titration curve (Figure 2.8b) more clearly shows two equivalence points near pH = 4.7 and pH = 9.5. Equivalence points for phosphoric acid at 25°C have previously been reported to occur at pH = 4.67 and pH = 9.79, while phosphonic acid shows a peak at pH = 4.89 [38]. Based on volumes from the titration, we calculated the solution contains 5.05×10^{-5} moles of H_3PO_4. From gas-phase IR, 1.78×10^{-5} mol of PH_3 was produced during the 48-hour aging process. Thus, our experiments imply formation of approximately 3 moles of H_3PO_4 for each mole of PH_3 produced under the conditions of our experiment. Identifying a specific mechanism for PH_3 degradation is challenging because oxidation can be induced by both O_2 and by H_2O in amounts that depend on experimental conditions. A previous study of red phosphorus degradation upon exposure to water and air [5] reported an overall approximate stoichiometry of:

$$3.5P_4 + 21H_2O + 11.275O_2 \rightarrow 5.2H_3PO_4 + 7.15H_3PO_3 + 0.65H_3PO_2 + PH_3$$

However, under oxygen-deficient conditions, a simpler stoichiometry can be identified:

$$2P_4 + 12\ H_2O \rightarrow 3H_3PO_4 + 5\ PH_3$$

Notably, the relative amounts of H_xPO_y species increases as the contribution from O_2 increases. Our data indicate a larger proportion of H_3PO_4 than could be produced by water alone. This in turn suggests that under the conditions of our experiments, using a stagnant reservoir of water equilibrated with the atmosphere, both H_2O and O_2 are important in controlling the overall reaction. This conclusion is further supported by DRIFTS measurements showing the presence of phosphoric (H_3PO_4) and phosphonic (H_3PO_3) species on the surface. The presence of both species is consistent with prior studies using ion chromatography [5] and can be considered as a natural evolution of the surface starting with elemental P that is then successively oxidized to form surface -PO, -PO_2, and -PO_3 species prior to release into the aqueous medium as fully oxidized -PO_4 species, with appropriate levels of protonation. Notably, however, the effective thickness of the PO_3 layers measured by XPS can significantly exceed the thickness of a monolayer film; this shows that the formation of liquid H_3PO_4 and/or polyphosphate surface species is insufficient to halt further reactions of red phosphorus with water vapor and/or O_2. The kinetic data found from Figure 2.3 and presented in Table 2.1 show that the rate of reaction appears to decrease somewhat, suggesting that the liquid H_3PO_4 surface film reduces further reactions but does not halt them altogether.

The influence of the carbon coating is summarized in Figure 2.9. Our FTIR data show that phosphine production is suppressed by the presence of a surface carbon coating. Using a longer plasma deposition time leads to particles with larger average carbon thicknesses (as measured by XPS) that are more resistant to reacting with water and oxygen to form PH_3. This increase in carbon coating thickness protects the red phosphorus from degradation, suppressing phosphine production (as measured by FTIR), and slowing the formation of a top layer of PO_x species that forms as the particles age (as measured by XPS). While very thin carbon films inhibit the reaction with water, the amount of surface -PO_x species observed from XPS is still larger than would be expected from a simple monolayer. While experiments cannot directly show a detailed mechanism of residual reactivity, we hypothesize that in the case of an imperfect coating with small pinholes, reaction with water vapor at the pinholes produces liquid H_3PO_4 than can then spread beyond the pinhole, forming a thin layer extending across the entire particle surface. Longer deposition times have a higher probability of covering these pinholes, as seen in SEM images, reducing the exposed RP surface, leading to less measured phosphine and PO_x species.

2.4. Conclusion

We have demonstrated the efficacy of thin plasma-deposited carbon coatings of red phosphorus as a method of suppressing the production of toxic phosphine gas and acidic phosphorus-based byproducts. Using a combination of infrared spectroscopy and x-ray photoelectron spectroscopy, we quantified the production of phosphine, phosphoric acid, and phosphonic acid upon the exposure of red phosphorus to high humidity environments. XPS, diffuse reflectance IR, and titrations have provided data to construct a model of how plasma-deposited carbon is able to suppress phosphine and phosphoric-based acid generation (Figure 2.9). The plasma deposition method provides a thin, non-reactive carbon coating that provides a solution to long-term stability of red phosphorus regardless of the application.

2.5. Figures

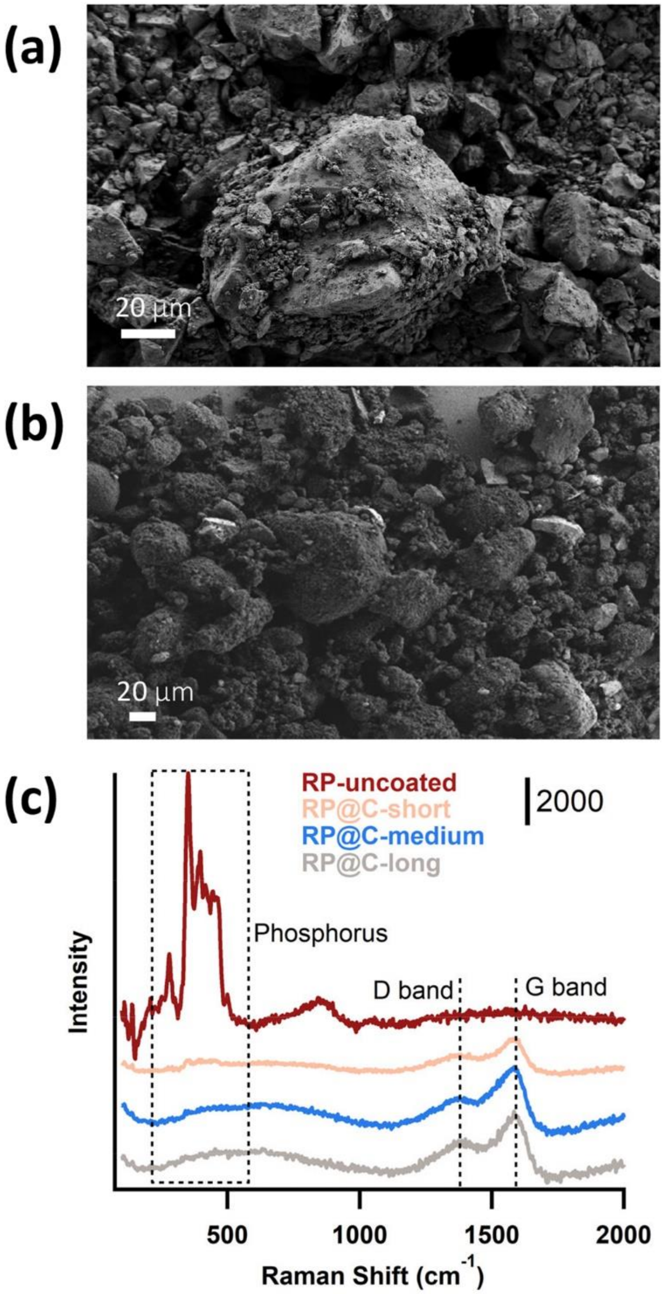

Figure 2.1. SEM micrographs of (a) non-aged uncoated red phosphorus and (b) RP@C-long and (c) Raman spectra for non-aged red phosphorus with various carbon deposition times.

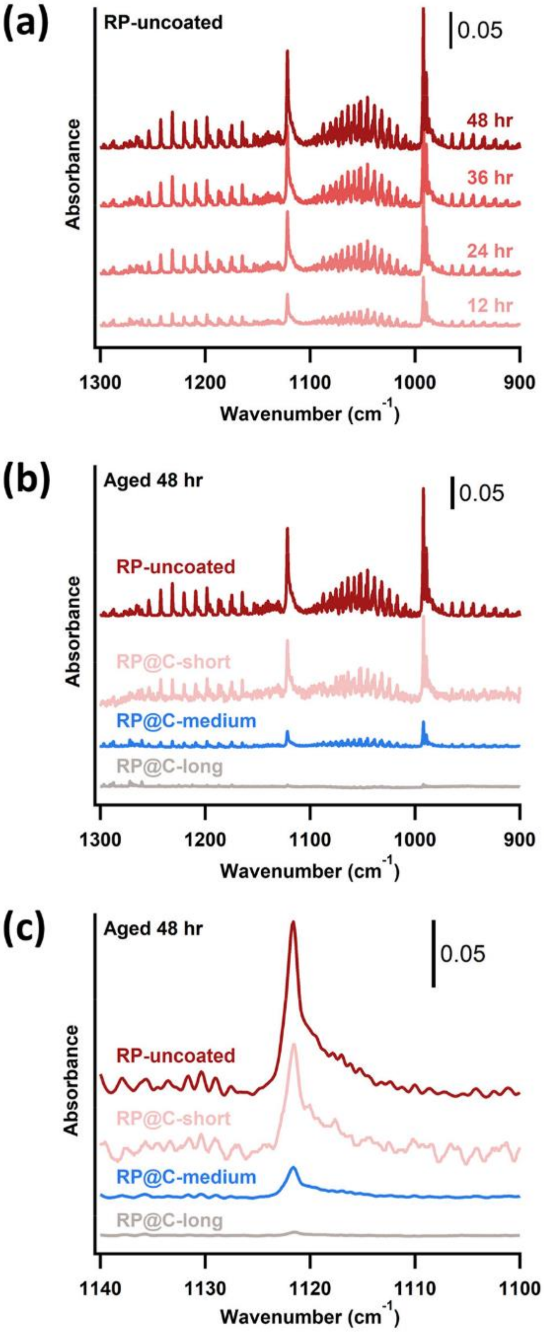

Figure 2.2. IR headspace spectra showing changes in PH3 as a function of time and of RP coating. (a) Uncoated RP after exposure to H2O vapor over 48h; (b) IR spectra for RP samples with coated at varying PDC deposition times after 48h aging at 50°C, 100% humidity, and (c) same as (b) except higher-resolution examination of the spectral region used for quantitative analysis.

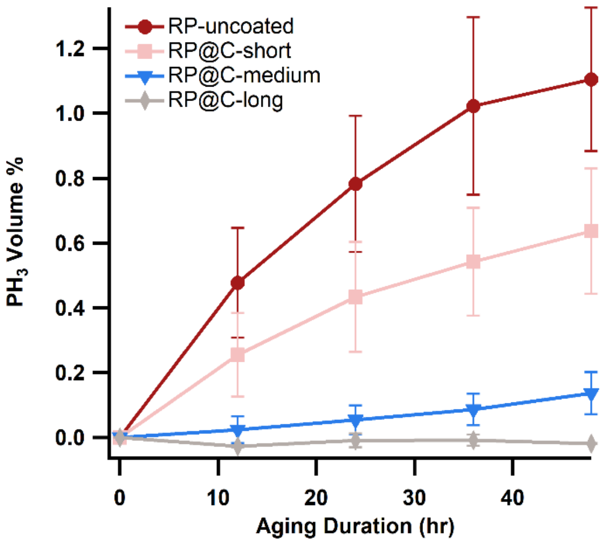

Figure 2.3. Cumulative production of PH3 vs. duration of aging, for bare RP (0 min) and for samples exposed to the carbon plasma for increasing lengths of time.

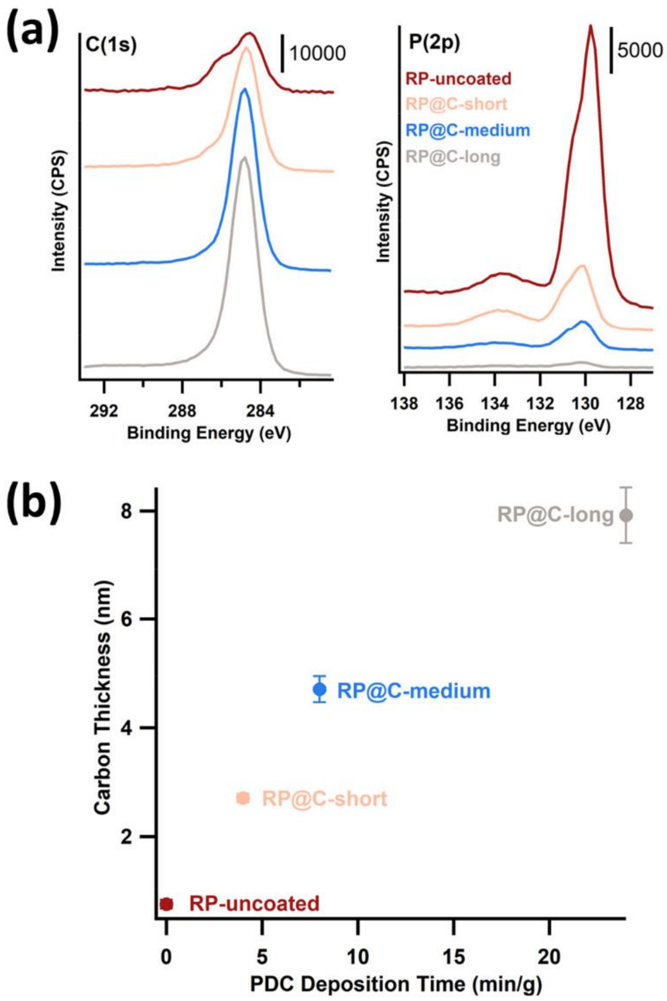

Figure 2.4. (a) XPS C(1s) and P(2p) intensities (in counts per second) for non-aged RP samples prepared using indicated carbon plasma deposition times and (b) thickness of carbon layer calculated from XPS attenuation data for nonaged samples.

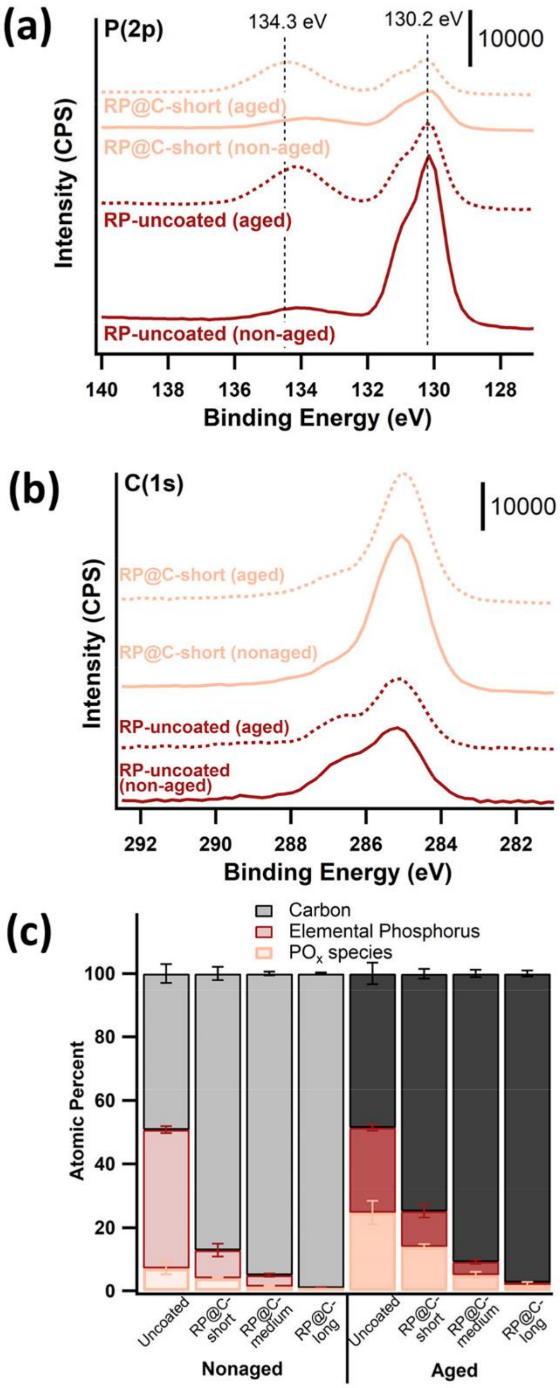

Figure 2.5. XPS of (a) C(1s) and (b) P(2p) intensities (in counts per second) for uncoated and RP@C-short particles before and after aging and (c) calculated atomic percent for carbon, elemental phosphorus, and oxidized phosphorus as affected by aging and carbon coating deposition time.

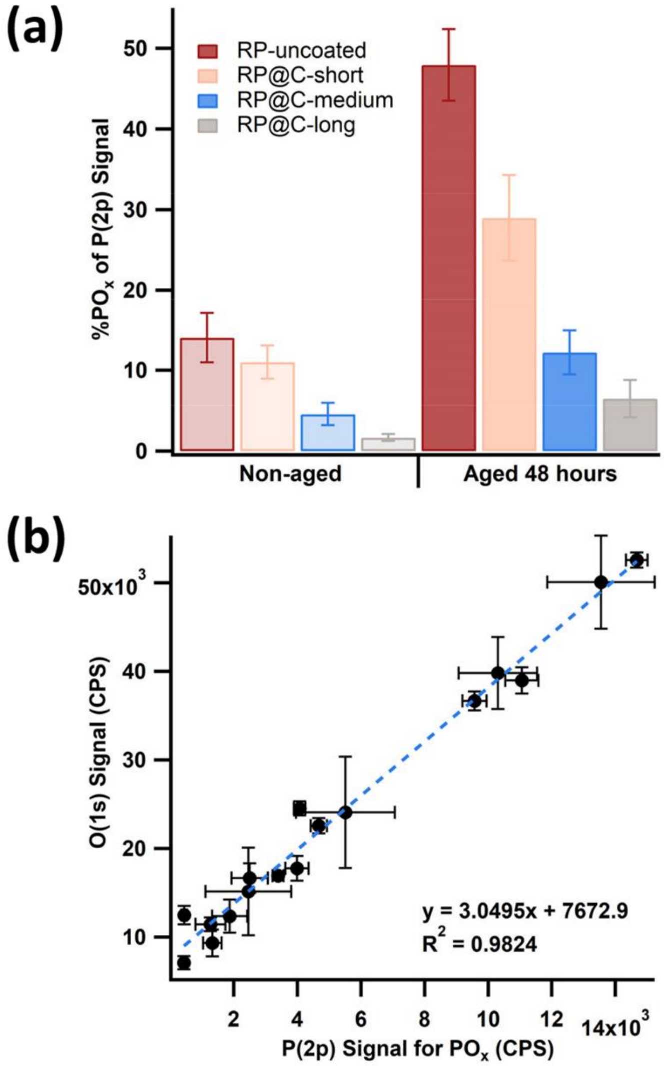

Figure 2.6. (a) Effect of aging and coating deposition time on area under the phosphate region of the P2p curve and (b) plot of integrated area for O(1s) vs. P(2p) phosphate region for all samples (non-aged and aged, uncoated and coated).

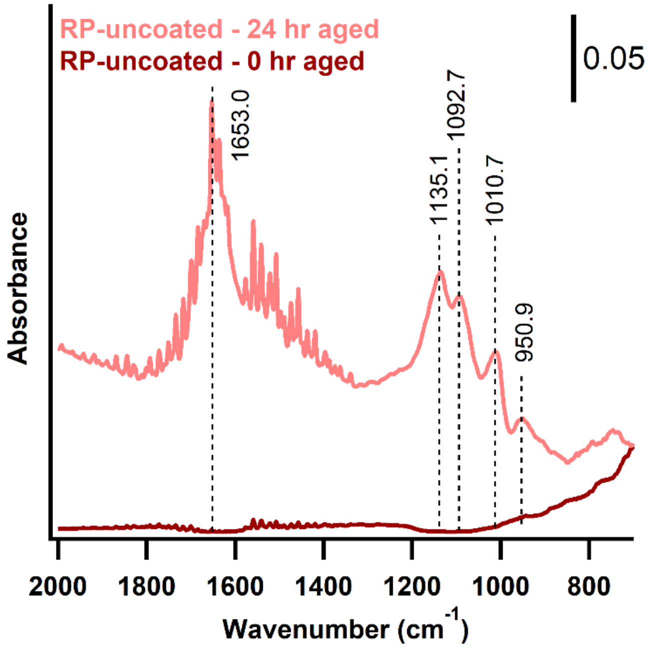

Figure 2.7. DRIFTS spectra of bare red phosphorus before and after aging in 100% humidity at 50°C.

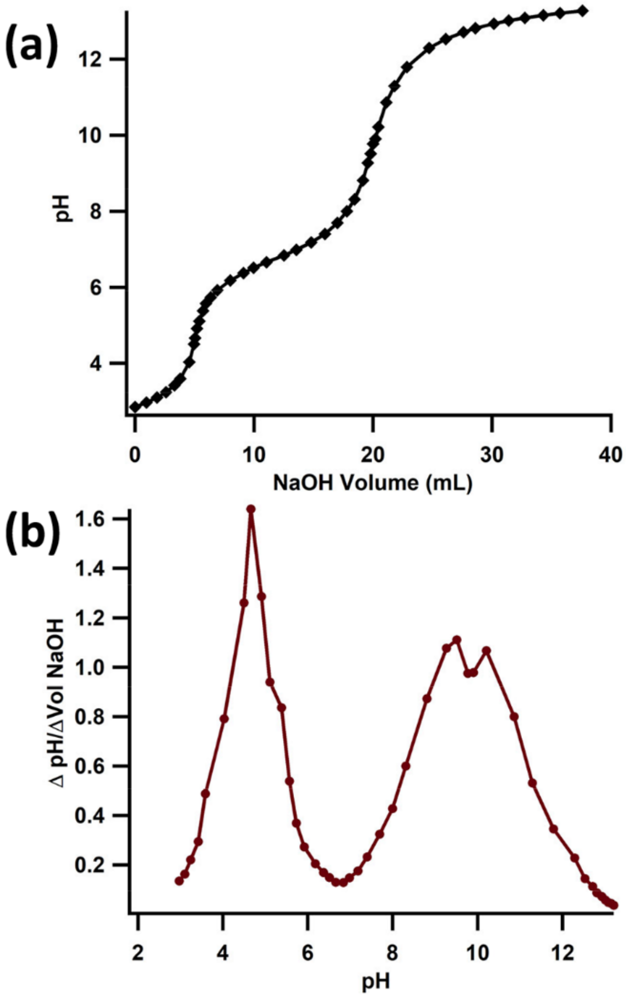

Figure 2.8. (a) Titration curve of supernatant of bare, aged RP and (b) derivative of titration curve from (a).

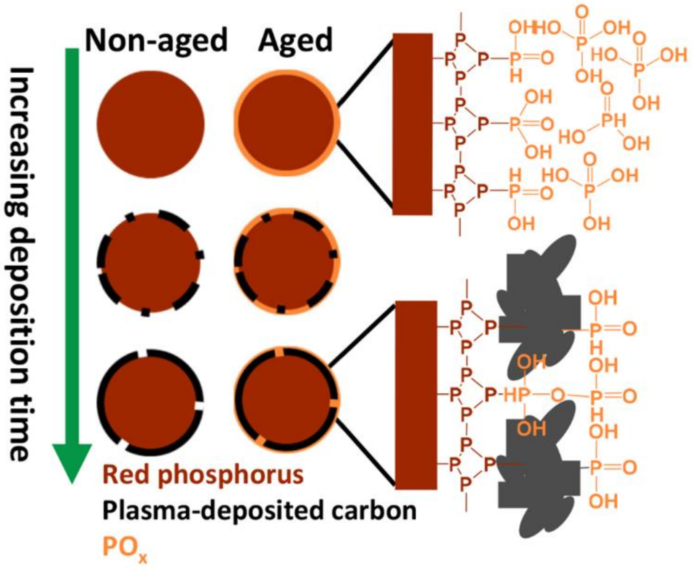

Figure 2.9. Proposed surface of red phosphorus after aging with and without plasma-deposited carbon protective coating. (*monolayer shown for simplification).

Table 2.1. Effect of carbon deposition time on initial rate of PH3 production from IR for first 12 hours.

Duration of plasma deposition	Initial PH_3 production rate (Vol %/hr)	Normalized PH_3 production rate, relative to uncoated P
Uncoated	0.040 ± 0.014	1
Short	0.021 ± 0.011	0.5
Medium	0.002 ± 0.003	0.05
Long	-0.0023 ± 0.0003	-0.05

2.6. References

[1] N. Davies, Red Phosphorus for Use in Screening Smoke Compositions, in, Royal Military College of Science Shrivenham (United Kingdom), 1999.

[2] Y.H. Liu, Q.Z. Liu, C. Jian, D.Z. Cui, M.R. Chen, Z. Li, T. Li, T. Nilges, K. He, Z. Jia, C.W. Zhou, Red-phosphorus-impregnated carbon nanofibers for sodium-ion batteries and liquefaction of red phosphorus, Nat Commun, 11 (2020).

[3] M.R. Somayajulu, G.K. Gautam, A.S. Rao, Stabilisation of red phosphorus to prevent moisture absorption and suppression of phosphine release, Defence Sci J, 57 (2007) 817-824.

[4] United Nations Environment Programme., International Labour Organisation., World Health Organization., International Program on Chemical Safety., Phosphine and selected metal phosphides, World Health Organization; WHO Publications Center USA distributor, Albany, N.Y., 1988.

[5] V.J. Norris, Investigation of the Mechanism of the Oxidation of Red Phosphorus, in: Proceedings of the 27th International Pyrotechnics Seminar, IPSUSA, Inc., Grand Junction, CO, USA, 2000, pp. 207-216.

[6] C. Wilharm, F.E. Montgomery, M819 Red Phosphorus Smoke Reformulation Study, in: Proceedings of the 31st International Pyrotechnics Seminar, IPSUSA, Inc., 2004, pp. 11-16.

[7] J.A. Conner, J.A. Davenport, M819 Corrosion Study, in: Proceedings of the 27th International Pyrotechnics Seminar, IPSUSA, Inc, 2000, pp. 435-444.

[8] A.E. Cardell, T.T. Griffiths, T.A. Vine, Design Guide for Munitions Containing Red Phosphorus, in: Proceedings of the 31st International Pyrotechnics Seminar, IPSUSA, Inc., Ft. Collins, CO, USA, 2004.

[9] H. Staendeke, F.-J. Dany, J. Kandler, W. Klose, Stabilized red phosphorus and process for making it, in: USPTO (Ed.), Hoechst Aktiengesellschaft, United States, 1977.

[10] W. Racky, H. Cherdron, Moulding composition of thermoplastic materials, in: USTPO (Ed.), Hoechst Aktiengesellschaft, United States, 1974.

[11] F. Eisenträger, Key Parameters for the Stability of Red Phosphorus, in: Proceedings of the 31st International Pyrotechnics Seminar, IPSUSA, Inc., Fort Collins, CO, USA, 2004.

[12] J. Robertson, Properties of diamond-like carbon, Surface and Coatings Technology, 50 (1992) 185-203.

[13] H.Q. Li, H.S. Zhou, Enhancing the performances of Li-ion batteries by carbon-coating: present and future, Chem Commun, 48 (2012) 1201-1217.

[14] Q. Cao, H.P. Zhang, G.J. Wang, Q. Xia, Y.P. Wu, H.Q. Wu, A novel carbon-coated LiCoO2 as cathode material for lithium ion battery, Electrochemistry Communications, 9 (2007) 1228-1232.

[15] R. Saroha, A.K. Panwar, Effect of in situ pyrolysis of acetylene (C2H2) gas as a carbon source on the electrochemical performance of LiFePO4 for rechargeable lithium-ion batteries, Journal of Physics D: Applied Physics, 50 (2017).

[16] M.L. Marcinek, J.W. Wilcox, M.M. Doeff, R.M. Kostecki, Microwave Plasma Chemical Vapor Deposition of Carbon Coatings on LiNi[sub 1⁄3]Co[sub 1⁄3]Mn[sub 1⁄3]O[sub 2] for Li-Ion Battery Composite Cathodes, Journal of The Electrochemical Society, 156 (2009).

[17] M. Noborisaka, T. Hirako, A. Shirakura, T. Watanabe, M. Morikawa, M. Seki, T. Suzuki, Synthesis of Diamond-Like Carbon Films on Planar and Non-Planar Geometries by the Atmospheric Pressure Plasma Chemical Vapor Deposition Method, Japanese Journal of Applied Physics, 51 (2012) 090117.

[18] J.H.J. Scott, S.A. Majetich, Z. Turgut, M.E. McHenry, M. Boulos, Carbon Coated Nanoparticle Composites Synthesized in an RF Plasma Torch, MRS Proceedings, 457 (1996) 219.

[19] J.R. Conrad, J.L. Radtke, R.A. Dodd, F.J. Worzala, N.C. Tran, Plasma source ion-implantation technique for surface modification of materials, Journal of Applied Physics, 62 (1987) 4591-4596.

[20] S. Miyagawa, S. Nakao, M. Ikeyama, Y. Miyagawa, Deposition of diamond-like carbon films using plasma based ion implantation with bipolar pulses, Surface and Coatings Technology, 156 (2002) 322-327.

[21] D.A. Shirley, High-resolution X-ray photoemission spectrum of valence bands of gold, Physical Review B, 5 (1972) 4709-&.

[22] T.L. Barr, S. Seal, Nature of the use of adventitious carbon as a binding-energy standard, J. Vac. Sci. Technol. A-Vac. Surf. Films, 13 (1995) 1239-1246.

[23] R.A. Franking, E.C. Landis, R.J. Hamers, Highly stable molecular layers on nanocrystalline anatase TiO2 through photochemical grafting, Langmuir, 25 (2009) 10676-10684.

[24] D.P. Monaghan, K.C. Laing, P.A. Logan, P. Teer, D. Teer, How to Deposit DLC Successfully, Materials World, 1 (1993) 347-349.

[25] C.J. Powell, A. Jablonski, NIST Electron Effective-Attenuation-Length Database Version 1.3, in, National Institute of Standards and Technology, Gaithersburg, MD, 2011.

[26] P.J. Cumpson, The Thickogram: a method for easy film thickness measurement in XPS, Surf. Interface Anal., 29 (2000) 403-406.

[27] J.R. Durig, J.M. Casper, On the vibrational spectra and structure of red phosphorus, Journal of Molecular Structure, 5 (1970) 351-358.

[28] A.C. Ferrari, Raman spectroscopy of graphene and graphite: Disorder, electron-phonon coupling, doping and nonadiabatic effects, Solid State Commun, 143 (2007) 47-57.

[29] A.C. Ferrari, J. Robertson, Raman spectroscopy of amorphous, nanostructured, diamond-like carbon, and nanodiamond, Philosophical Transactions of the Royal Society A, 362 (2004) 2477-2512.

[30] L.R. Brown, R.L. Sams, I. Kleiner, C. Cottaz, L. Sagui, Line Intensities of the Phosphine Dyad at 10 μm, Journal of Molecular Spectroscopy, 215 (2002) 178-203.

[31] C. Sousa-Silva, A.F. Al-Refaie, J. Tennyson, S.N. Yurchenko, ExoMol line lists - VII. The rotation-vibration spectrum of phosphine up to 1500 K, Mon. Not. Roy. Astron. Soc., 446 (2015) 2337-2347.

[32] C. Wagner, A. Naumkin, A. Kraut-Vass, J. Allison, C. Powell, J. Rumble Jr, NIST X-ray Photoelectron Spectroscopy Database, NIST standard reference database 20, Version 3.4 (Web version), National Institute of Standards and Technology: Gaithersburg, MD, 20899 (2003).

[33] G. Socrates, Infrared and Raman Characteristic Group Frequencies: Tables and Charts, 3rd ed., Wiley, 2004.

[34] L.C. Thomas, R.A. Chittenden, Characteristic infrared absorption frequencies of organophosphorus compounds—I The phosphoryl (P=O) group, Spectrochimica Acta, 20 (1964) 467-487.

[35] W.W. Rudolph, Raman-and infrared-spectroscopic investigations of dilute aqueous phosphoric acid solutions, Dalton Transactions, 39 (2010) 9642-9653.

[36] L.C. Thomas, R.A. Chittenden, Characteristic infrared absorption frequencies of organophosphorus compounds—II. P-O-(X) bonds, Spectrochimica Acta, 20 (1964) 489-502.

[37] W. Jastrzbski, M. Sitarz, M. Rokita, K. Bułat, Infrared spectroscopy of different phosphates structures, Spectrochimica Acta Part A: Molecular and Biomolecular Spectroscopy, 79 (2011) 722-727.

[38] D.C. Harris, Quantitative chemical analysis, 8th ed., W.H. Freeman and Company, 2010.

Chapter 3: Thin carbon scaffold on metal oxide nanomaterials for stable covalent functionalization

A manuscript of this work is in preparation and will be submitted to *ACS Nanoscience Au* with co-authors Curtis M. Green, Jaya Borgatta, Catherine E. Kruszunski, Elizabeth D. Laudadio, and Robert J. Hamers

All of the experiments, data acquisition and analysis, and manuscript preparation and revision were done by Paige C. Kinsley under the advisement of Robert J. Hamers except for the following:

Curtis M. Green assisted in synthesis of nanoruby and collected transmission electron micrographs in Figure A.3.2. Jaya Borgatta assisted in the synthesis of Fe_3O_4 nanoparticles. Elizabeth D. Laudadio assisted in conceptualization of atomic force microscopy experiments.

3.1 Introduction

Metal oxide nanomaterials have numerous uses both as analytical tools and in applications for fields such as batteries and agriculture. Control over the surface chemistry of these materials can enhance and broaden their applications. Nanoruby (Al_2O_3:Cr^{3+}) can be used for long-term imaging and tracking in complex system.[1] Iron oxide nanoparticles are superparamagnetic, making them ideal for use as retrievable nanoparticles, providing a tool to study all components of protein corona formation on nanoparticles, both soft and hard.[2] Metal oxide nanoparticles are also being used broadly in a number of different industries, from agriculture[3] to medicine[4] to personal care products.[5] Control over the particle surface could increase their efficiency and effectiveness, targeting specific parts of plants or bodies for delivery of nutrients or drugs.

Common methods to functionalize metal oxides are often either using a silica coating that can be further functionalized or direct bonding through the metal-oxide bond, often using a phosphoric acid or carboxylic acid.[6] Currently, long-term functionalization is challenging, especially if the particles are exposed to complex biological systems, where pH, temperature, and ionic strength variations can cause desorption or hydrolysis of bound species from the surface, resulting in a loss of control of the intended surface chemistry.[7, 8] Binding intended ligands to the surface through carbon-carbon bonds will increase chemical stability and longevity on the nanoparticle surface. Carbon coatings are commonly used for metal oxide battery materials to improve material conductivity and battery performance.[9] Methods such as chemical vapor deposition[10] and calcining in acetylene gas[11] can form graphitic-like carbon coatings but controlling the uniformity of the layers can be challenging when not all particle surfaces are exposed to the carbon source. Additionally, methods such as calcining particles after ball milling in sucrose[12] make it challenging to limit the amount of carbon on the surface. Producing a thin, stable carbon coating on the surface of metal oxides would provide a platform for long-term functionalization, allowing us to broaden understanding and control exposure of metal oxides in biological systems.

We have developed a method that forms a thin, stable carbon layer on metal oxide nanoparticle surfaces, providing a platform for further chemical modification using thermal radical initiation of molecules (Scheme 3.1).[13] Linoleic acid was chosen as the carbon source, as the carboxylic head provides a binding site on the molecule such that a monolayer of molecules will initially adsorb to the metal oxide surface.[14] Linoleic acid also contains two points of unsaturation in the alkyl tail, providing potential sites for thermal crosslinking between molecules. After forming an adsorbed layer of linoleic acid on the metal oxide surface, the particles are heated in a closed system in a slightly reducing atmosphere (5% H_2:95% N_2) to produce a thermally stable carbon shell containing sp^2 and sp^3 carbon. The carbon surface formed after thermal treatment provides a platform for covalent attachment of vinyl molecules with various chemical properties. This carbonization treatment of metal oxides offers a general method to tune the surface chemistry of metal oxide nanomaterials for long-term surface functionalization. Stable, covalent functionalization of metal oxides will give control over chemical species present on their surface and allow for deeper insights into nano-bio interactions.

3.2 Materials and Methods

3.2.1. Materials

Aluminum oxide nanoparticles (alpha, 27-43 nm) were purchased from Nanostructured and Amorphous Materials Inc. Zinc oxide nanoparticle (10-30 nm) were purchased from US Research Nanomaterials, Inc. Iron (II,III) oxide nanoparticles (11 ± 3 nm, from TEM) were synthesized as previously reported, described in the supporting information.[15] Nanoruby (27 ± 14 nm, from TEM) synthesis was adapted from previous work[16], also described in the supporting information. Planar aluminum oxide wafers were purchased from MTI corporation. 1H,1H-undecafluorohexylamine (>97.0%), arachidonic acid (99%), oleic acid, and cis-11-eicosenoic acid were purchased from Fisher Scientific. Cis-11,14-eicosadienoic acid was purchased from Santa Cruz Biotechnology. Forming gas (95% N_2: 5% H_2) was purchased from Airgas. All other chemicals were purchased from Sigma-Aldrich. Stainless steel Swagelok cell (parts SS-600-6 and SS-600-C) used for thermal carbonization was purchased from Kurt J. Lesker Company. All water used was nanopure water (18.2 MΩ).

3.2.2. Nanomaterial Synthesis and Functionalization

Aluminum oxide nanoparticles were prepared by first adsorbing a linoleic acid monolayer in solution, and then sealed and heated in a closed vessel to decompose linoleic acid, forming a carbon shell. This carbon shell can be further functionalized with ligands, as described in subsequent paragraphs. To prepare aluminum oxide nanoparticles for carbonization, shown in Scheme 3.1, 1.000 g Al_2O_3 nanoparticles were added to hexadecane (20 mL). Linoleic acid (20 uL) was added, and the mixture was stirred for 24 hours at room temperature. To wash, the particles were collected from solution by centrifugation (10 min at 3780xg). The particles were then resuspended and spun down (10 min at 3780xg) twice in 10 mL hexadecane and twice in 10 mL hexane. The particles were dried in a vacuum at 30°C for 2 hours. To carbonize the linoleic acid layer, dry LA-Al_2O_3 particles were placed in steel Swagelok cell sealed under argon atmosphere. The cell was heated in at tube furnace at 450°C under a forming gas (95% N_2: 5% H_2) flow of 50 standard cubic centimeters per minute (0.83 atm·cc/s) for 2 hours and cooled overnight, producing Al_2O_3@C NP.

Formation and carbonization of carbon films using other fatty acids used the same ratios of Al_2O_3 NP, solvent, and fatty acid (1.000 g Al_2O_3 NP: 20 mL hexadecane: 0.128 mmol fatty acid).

Functionalization of carbonized Al_2O_3 nanoparticles (Al_2O_3@C) with 4-pentenoic acid was adapted from a previously reported method, functionalizing carbon materials using the thermal radical initiator benzoyl peroxide (BPO).[13] Briefly, Al_2O_3@C NP (200 mg) was weighed into a 20 mL headspace vial. In a glove box under argon, 6 mL benzene was added to vial containing 0.980 mmol of 4-pentenoic acid and 70 mg of BPO along with 4Å molecular sieves and left to dry for 30 min. Dry solvent, ligand, and BPO were transferred to headspace vial containing Al_2O_3@C NP and the vial was sealed, vortexed to suspend particles, and heated for 3.5 hr at 80°C under constant stirring. Particles were washed 2x with 10 mL acetone (breaking down any residual polymer products) by centrifugation at 3048xg, then washed 3x with 15 mL ethanol, centrifuging at 3048xg. The particle pellet was dried in vacuum oven at 30°C overnight.

Further functionalization of Al_2O_3@C-COOH was done using EDC coupling, forming an amide linkage on the surface (Scheme 3.2). The functionalization was adapted from previous literature,[17, 18] and details can be found in the supporting information.

Details on the synthesis of nanoruby and Fe_3O_4 nanoparticles can be found in the supporting information, including characterization of nanoparticles (Figures A.3.1 and A.3.2). Ruby, Fe_3O_4, and ZnO nanoparticles were carbonized and functionalized following the same procedure as that of Al_2O_3 nanoparticles.

3.2.3. Nanomaterial Characterization

X-ray photoelectron spectroscopy data were taken using a Thermo K-alpha XPS with an Al Kα source (1486.6 eV photon energy) at a 45° take-off angle. XPS samples were prepared by suspending nanoparticles in ethanol and the dropcasting on to a clean boron-doped silicon wafer. Three points were taken per sample for statistical analysis.

Data was worked up in CasaXPS using a Shirley background fit[19] and mixed Gaussian-Lorentzian line shape GL(30). All spectra were calibrated to the adventitious carbon C(1s) peak at 284.8 eV.[20] Carbon thickness calculations were calculated using areas under Al(2p) and C(1s) peaks, using a model that address the influence of electron scattering within the substrate and carbon layer, reported previously[21]:

$$\frac{1 - e^{-t_c / \lambda_{C,C}}}{e^{-t_c / \lambda_{Al,C}}} = \frac{A_{C(1s)}}{A_{Al(2p)}} \cdot \frac{\rho_{Al2O3}}{\rho_C} \cdot \frac{SF_{Al(2p)}}{SF_{C(1s)}} \cdot \frac{\lambda_{Al(2p),Al2O3}}{\lambda_{C(1s),C}} \qquad (3.1)$$

A: peak area; ρ: density of layer (ρ_{Al2O3} = 46.66 Al atoms/nm^2, ρ_C = 75.3 C atoms/nm^2 [estimated from density of amorphous carbon, 1.5 g/cm^3]^{22}; SF: atomic sensitivity factor (for Thermo XPS, $SF_{Al(2p)}$ =0.56, $SF_{C(1s)}$=1); λ: inelastic mean free path, calculated using NIST Effective Attenuation Length Database[23] ($\lambda_{C1(s),C}$ = 3.798 nm, $\lambda_{Al(2p),C}$ = 4.61 nm, $\lambda_{Al(2p),Al2O3}$ = 2.826 nm); t_c: carbon layer thickness (calculated value). The substrate values to calculate carbon thickness on zinc oxide and iron oxide particles were adjusted as follows: ρ_{ZnO}=41.51 Zn atoms/nm^2, $SF_{Zn(2p)}$ = 31.86, $\lambda_{Zn(2p),C}$ = 3.716 nm, $\lambda_{Zn(2p), ZnO}$ =2.285 nm; ρ_{Fe3O4} = 40.34 Fe atoms/nm^2, $SF_{Fe(2p)}$ = 14.35, $\lambda_{Fe(2p),C}$ = 2.741 nm, $\lambda_{Fe2p, Fe3O4}$ =2.196 nm.

To understand the density of functionalized ligands on the carbon surface, the surface coverage of specific elements of interest was calculated using the following equation:

$$Coverage\ (\frac{atoms}{nm^2}) = \frac{Area_{Element}}{Area_{Sub}} * \frac{SF_{Sub}}{SF_{Element}} * \rho * \lambda * \cos(45°) \qquad (3.2)$$

A; peak area, ρ: density of atoms in substrate (ρ_{Al2O3} = 46.66 Al atoms/nm^2), SF: sensitivity factor (for Thermo XPS: $SF_{Al(2p)}$ = 0.56, $SF_{C(1s)}$ = 1, $SF_{N(1s)}$= 1.68, $SF_{F(1s)}$ = 4.12. $SF_{S(2p)}$ = 1.88), λ: inelastic mean free path of electron through substrate, calculated using NIST Effective Attenuation Length Database[23] ($\lambda_{Al(2p),Al2O3}$ = 2.826 nm).

Infrared data was taken using a Bruker Vertex 70 spectrometer at a 4 cm^{-1} resolution from 5000 to 700 cm^{-1}. Nanoparticle spectra were taken using diffuse reflectance IR, prepared in a pellet at 1 wt% NP in KBr, with 500 scans per spectrum. Attenuated total reflectance IR was used to take spectra of organic small molecules using a diamond ATR crystal and 100 scans per spectrum.

Dynamic light scattering (DLS) and laser Doppler electrophoresis were taken with a Malvern Zetasizer Nano ZS. Samples were prepared at 0.1 mg/mL, suspending by 1-hour ultrasonication (10 sec on, 10 sec off). Size and zeta potential (ZP) values reported are averages of 5 DLS measurements per sample and 10 ZP measurements per sample.

Atomic force microscopy scratching experiments were done on a Bruker FastScan AFM using a TAP 300 DLC-10 tip (purchased from Budget Sensors). Planar Al_2O_3 wafers (0001 face) were prepared following the same procedure used for Al_2O_3, adjusting linoleic acid ratios such that ~10x linoleic acid was in solution for alumina surface area, with wafers suspended vertically for linoleic acid adsorption to avoid settling. Scratching was first done in tapping mode with a deflection set point of 0.200 V, scratching a 500 nm x 500 nm area. Topography after scratching was measured in ScanAsyst mode, scanning 1 μm x 1 μm area using same tip.

To prepare fluorescence samples, 1 mg/mL of nanoruby (bare or carbonized) was suspended via 30 min bath sonication in 1% TWEEN-20 solution to ensure nanoparticle suspension during analysis. Using an ISS K2 photo-counting spectrofluorometer, samples were excited at 410 nm[24] and emission was collected from 670 nm – 710 nm (0.5 nm step size).

Thermogravimetric analysis measurements were done using a TA Q500 thermogravimetric analyzer, measuring mass change for 10-15 mg of sample under N_2 gas flow from 25°C – 800°C.

Raman measurements were taken using a Thermo-Fischer Scientific DXRxi Raman imaging microscope using 532 nm laser excitation and 10x objective. The laser used for planar Al_2O_3 was 2.0 mW, and for Fe_3O_4 NP was 3.0 mW.

Scanning electron micrographs were taken on a Leo Supra55 VP SEM at 1-3 kV electron voltage using a secondary electron detector.

Transmission electron microscopy was done on a Tecnai T12 at an accelerating voltage of 120 kV. Iron oxide nanoparticles were suspended in ethanol via bath sonication. An aliquot of the suspension was then dropped onto a Si_3N_4 grid with 8 nm thick windows (Ted Pella) and allowed to dry overnight. Image analysis was conducted using ImageJ open-source software. The size reported is the average of 142 particles.

3.3. Results and Discussion

3.3.1. Formation and characterization of a thin carbon layer

To understand the transformation of the carbon layer on the aluminum oxide surface, we first look at X-ray photoelectron spectroscopy to determine the thickness of the carbon layer of aluminum oxide nanoparticles before and after carbonization. Figure 3.1 shows the Al(2p) and C(1s) regions of Bare-Al_2O_3, LA-Al_2O_3, and Al_2O_3@C NP. The adsorption of the linoleic acid to the surface significantly increases the C(1s) intensity, while slightly decreasing Al(2p). Carbonization decreases the carbon peak once more. Using Equation 3.1, the carbon thickness can be calculated based on the attenuation of Al(2p) electrons from the substrate by the carbon overlayer vs. C(1s) electrons from the carbon overlayer. Bare, untreated Al_2O_3 NP had a carbon thickness of 0.28±0.04 nm, likely arising from the adsorption of adventitious carbon. LA-Al_2O_3 NP had a calculated carbon thickness of 1.23±0.06 nm, while Al_2O_3@C had a carbon thickness of 0.40±0.06 nm. As a secondary confirmation of thickness, we performed scratching experiments by atomic force microscopy on planar Al_2O_3 prepared in the same way as Al_2O_3 NP. Figure 3.2 shows the AFM images of bare planar alumina (Fig 3.2a) and planar alumina after linoleic acid adsorption and carbonization (Fig 3.2b). The line scans in Figure3.2c show a significant divot for the carbonized sample where carbon has been scratched away by the AFM tip. Comparing the values measured in AFM and XPS for planar samples and XPS values for nano-samples, shown in Table 3.1, we see some variation but overall agreement in thicknesses. Differences between nanoparticles and planar samples can be attributed to the lower density packing of linoleic acid on the nanoparticle surface.[25] Differences between AFM and XPS for bare planar samples can be ascribed to the assumption of the XPS thickness equation that there is greater than a monolayer of carbon on the surface, which is not necessarily the case on the bare sample. Based on both AFM and XPS analysis, we can conclude that a carbon layer on the nanometer scale is being formed on the surface of the aluminum oxide for both planar and nano samples. While XPS can give us some understanding of the type of carbon on the surface after carbonization, infrared spectroscopy, thermal gravimetric analysis, and Raman spectroscopy will give a clearer picture of the form of carbon.

The diffuse reflectance IR spectra in Figure 3.3a show upon adsorption of linoleic acid to Al_2O_3, C-H peaks grow in (3000-2800 cm^{-1}) along with carboxylic acid (1701 cm^{-1}) and carboxylate (1585 $cm^{-1)}$) peaks,[26] suggesting binding through deprotonated carboxylic acid head of linoleic acid. For further confirmation that carbon on surface comes from linoleic acid, the adsorption experiment was repeated using partially deuterated linoleic acid (Fig A.3.3). Along with the presence of C-H, COOH, and COO^- peaks, like LA-Al_2O_3, d11-LA-Al_2O_3 spectrum also shows C-D peaks at 2219 cm^{-1} and 2200 cm^{-1}, corresponding to those seen in the IR spectrum of neat d11-linoleic acid.[27] After carbonization, C-H and COOH peaks are reduced in intensity, but the carboxylate peak persists. The disappearance of the COOH peak points to the desorption of linoleic acid molecules not bound to the surface through the COO^--Al interaction, supporting the carbon thickness changes seen in XPS after heating. Reduction of the C-H peak at 2900 cm^{-1} indicates that the slightly reducing atmosphere of the thermal treatment (95% N_2:5% H_2) is likely breaking C-H bonds and reforming them as C-C bonds, which is supported by Raman spectroscopy and thermal gravimetric analysis (Fig 3.3b and 3.3c).

Thermal gravimetric analysis (TGA) on the Al_2O_3 NP gives insight to the thermal stability of the carbon species on the surface. Figure 3.3b shows linoleic adsorption increases the mass of molecules on the Al_2O_3 surface compared to bare Al_2O_3 NP. After carbonization, the mass on the surface is reduced, agreeing with XPS, while the thermal stability of the species still on the surface increases, degrading starting at 450℃ compared to 150℃-250℃ seen for LA-Al_2O_3.[28] A decomposition temperature of around 450℃ is indicative of more graphite-like carbon on the surface.[29] Carbonization temperature controls the thermal stability of the carbon layer on the surface. Figure A.3.4 shows that with increasing carbonization temperature (250°C, 350°C, or 450°C), the resultant carbon mass on the surface decreases, but the temperature at which it begins to decompose increases by almost 100°C, indicating graphitization of carbon on surface during carbonization.

Raman spectroscopy in Figure 3.3c confirms the carbon on Al_2O_3@C is graphitic. Al_2O_3 NP proved challenging to image using Raman spectroscopy because the large amount of scattering of the 532 nm laser by the white particles, so we used planar Al_2O_3 for Raman analysis. Ferrari and Robertson[30] proposed a three-stage model (from graphitic to tetrahedral amorphous carbon) based on the shift the carbon G band and the ratio of intensities of the D and G bands. For planar Al_2O_3@C, the G band arises at 1600±2 cm^{-1}, and I(D)/(G) is 0.60±0.04. These measurements correspond to stage 1 carbon, indicating the presence of mainly graphitic carbon on the alumina surface after carbonization. We also observe that the Al_2O_3 Raman shifts at 418, 579 and 731 cm^{-1} decrease as they are attenuated by the carbon overlayer we put down with the adsorption of linoleic acid.[31] This graphitization of carbon indicated by TGA and Raman spectroscopy can be seen by eye after carbonization (Figure A.3.5) as the particles go from white to gray.

To further understand the control we experimentally have over the carbon coating, we used fatty acids with varying chain length and degree of saturation as the carbon source (identified in Table A.3.1). While chain length (varied from 18 to 22 carbon) did not have a statistically different impact on carbon thickness calculated from XPS using Equation 3.1 (Figure A.3.6a), degree of saturation for 20-carbon fatty acids showed a noticeable trend. Figure 3.4 shows that while there is no obvious trend for fatty acids physisorbed to the surface, upon carbonization, with increasing number of double bonds, there is an increasing persistence in carbon on the surface. This increase may be due to contributions from the increased number of double bonds available for thermal crosslinking and the bent carbon tails of the molecules with more cis double bonds, increasing the surface area of the molecule lying next to the surface of the alumina.

Information from X-ray photoelectron spectroscopy, atomic force microscopy, infrared spectroscopy, thermal gravimetric analysis, and Raman spectroscopy, when looked at in tandem, indicate the formation of a 1-2 nm monolayer of fatty acid on the surface of alumina upon adsorption. Upon carbonization, this monolayer graphitizes to a carbon shell less than 1 nm thick. Aluminum oxide has been used as a model metal oxide for initial experiments, but success of this process is predicated on the application of this thin carbon coating on metal oxides of interest.

3.3.2. Application of carbonization on other metal oxides

Nanoruby has a long, stable fluorescence lifetime, with a sharp emission at 694 nm.[32] While confirmation of successful carbonization aluminum oxide is important, ensuring that the carbon layer does not quench or overly attenuate the phosphorescence from nanoruby is also necessary. Upon linoleic acid adsorption and subsequent carbonization, the carbon coating on nanoruby particles shows similar thicknesses to those measured on Al_2O_3 nanoparticles (Table 3.2). Slight variations in measured thickness are likely due to differences in nanoparticle size, affecting both the ligand packing density and apparent thickness of the carbon coating calculated from XPS.[25] We measured the impact of this ~1 nm carbon layer on the fluorescence of the nanoruby (Figure 3.5). Ruby has a fluorescent lifetime of ~3 ms,[33] while typical autofluorescence in a living system is on the order of $10^{-9} – 10^{-7}$ seconds. This means that even with slight attenuation of ruby emission brightness, time-gated imaging can still be used to pick out ruby even in complex biological systems, measuring ruby emission after waiting for autofluorescence to decay away.[1] Therefore, while the fluorescence intensity decreases after carbonization, it is not quenched, making carbonized nanoruby a valid fluorescent probe.

We broadened the application of the carbon coating process to other metal oxides of interest to see if it could be done on non-aluminum-based metal oxides. Figure 3.6 shows XPS spectra for the C(1s) region and the metal 2p region of interest. For both Fe_3O_4 NP and ZnO NP, there is an increase in the C(1s) intensity corresponding to the attenuation of Fe(2p) and Zn(2p), respectively, upon the adsorption of linoleic acid to the particle surface. After carbonization, the C(1s) intensity decreases and the metal 2p intensities increase. These changes follow the same patterns as Al_2O_3 NP (Figure 3.1), and the carbon coating thickness on Fe_3O_4 and ZnO are similar to those of Al_2O_3 NP (Table 3.2), with 1-2 nm of carbon on the surface after linoleic adsorption, and a reduction in thickness upon carbonization. Raman analysis of Fe_3O_4@C NP (Figure A.3.7) shows the appearance of strong D and G bands, just as those observed on planar Al_2O_3@C. Analysis of the G position (1592.0 ± 1.1 cm^{-1}) and D/G intensity ratio (0.71 ± 0.08) denotes stage 1 graphitic carbon on the surface, the same as Al_2O_3@C, indicating similar graphitization of the carbon on the surface during carbonization. There is a weak presence of Fe_3O_4 and Fe_2O_3 Raman peaks below 500 cm^{-1}.[34, 35] The low intensity of these peaks likely is due both their attenuation by the carbon coating and the scattering due to their nanoparticle morphology. The presence of Fe_2O_3 in the spectrum is due to oxidation by the focused laser.[36] Lastly, the yellow-white ZnO NP darken significantly after carbonization (Figure A.3.8), similar to Al_2O_3@C, indicating formation of more graphitic carbon on the surface as the linoleic acid thermally decomposes. Compared to Al_2O_3@C NP, the ZnO@C NP appear darker by eye, which is likely due to their smaller size (10 nm ZnO vs 35 nm Al_2O_3).

XPS and Raman analysis indicates that this carbonization method can be applied to other metal oxides of interest. Additionally, because of the thinness of the carbon layer, it can be applied to fluorescent metal oxides like nanoruby without quenching fluorescent properties.

3.3.3. Secondary functionalization of thin carbon layer on metal oxide nanoparticles

The stable, thin carbon surface on the aluminum oxide provides a platform for covalent functionalization using the thermal radical initiator benzoyl peroxide (BPO) and EDC coupling. Initial functionalization to the carbonized surface on Al_2O_3 NP was done using 4-pentenoic acid.

To confirm functionalization, we performed controls, running the reaction without benzoyl peroxide and without 4-pentenoic acid. Figure 3.7a shows that functionalization with 4-pentenoic acid in the presence of BPO increases the carbon content on the surface (from 0.40±0.06 nm for Al_2O_3@C to 1.34±0.010 nm for Al_2O_3@C-COOH). Additionally, the peak at 288.8 eV indicates the presence of C=O species on the surface. Without BPO or 4-pentenoic acid, this peak does not grow in, and the carbon thickness does not increase significantly (0.603±0.006 nm for Al_2O_3@C-COOH without acid and 0.595±0.013 nm Al_2O_3@C-COOH without BPO). The infrared spectra in Figure 3.7b, show the appearance of a COOH peak at 1706 cm^{-1} as well as C-H deformation peaks at 1409 cm^{-1} and C-C twisting vibrations at 1275 cm^{-1} seen in the 4-pentenoic acid IR spectrum.[26] These peaks are not present in control samples without BPO or 4-pentenoic acid. Functionalization with 4-pentenoic acid also changes the zeta potential from +40.5 ± 0.4 mV for Al_2O_3@C to -28.1 ± 0.2 mV for Al_2O_3@C-COOH (Figure 3.10). With the successful binding of a carboxylic acid group to the surface of carbonized Al_2O_3 NP, we can further modify the surface using EDC coupling (Scheme 3.2), linking molecules with various chemical properties through a stable amide linkage.

N-BOC-ethylenediamine, 1H, 1H-undecafluorohexylamine, and (2-aminoethyl)trimethylammonium chloride hydrochloride (pictured in Scheme 3.2) were selected as ligands as they provide a range of surface charges. We label the resulting functionalized Al_2O_3 NP as Al_2O_3@C-BOC, Al_2O_3@C-Fluro, and Al_2O_3@C-N^+. As was done with 4-pentenoic acid, we confirmed success of EDC coupling reaction using controls that were lacking EDC and sulfo-NHS, the components that form unstable intermediates that allows coupling between the carboxylic acid on the particle surface and primary amine of the ligand.

Al_2O_3@C-COOH has no nitrogen or fluorine on the surface. Figure 3.8 shows that the reaction run with EDC and sulfo-NHS using quaternary amine and BOC ligands, nitrogen peaks appear in the N(1s) XPS region (Fig 3.8b and 3.8d), along with an increase in carbon coverage (Fig 3.8a and 3.8c, with values in Table A.3.2). For Al_2O_3@C-N^+, there are two distinct N(1s) peaks appear at binding energies for amide and quaternary amine N species.[37] Without EDC, there is no noticeable nitrogen on the surface. Similarly, upon functionalization with EDC of the perfluorinated ligand, we see a growth of N(1s) and F(1s) peaks in XPS (Fig 3.9b and 3.9c), along with distinct C=O and C-F peaks in the C(1s) region. Without EDC, there is no nitrogen detected in the N(1s) region, but a small about of fluorine in F(1s), which is likely from residual fluorine from a small amount of physisorbed ligand. The expected F/N ratio for Al_2O_3@C-Fluro is 13:1. Based on surface coverage calculations (Table A.3.3), the ratio of F/N is 7.7:1, about half that expected based on molecular formula. The MES buffer used also contains nitrogen, along with a sulfur in a 1:1 ratio. Surface coverage calculations from S(2p) for Al_2O_3@C-Fluro indicate 4.3 ± 0.6 S atoms/nm^2 on the surface. Subtracting nitrogen for the MES buffer from total N coverage, the F/N ratio is 10.1:1, closer to the expected ratio based on the molecule.

As we did with Al_2O_3@C-COOH, further confirmation of functionalization was done using zeta potential to measure surface charge of particles (Figure 3.10). For all three controls without EDC, particles have zeta potentials around -15 mV, indicating the continued presence of exposed carboxylic acid species on the surface since the starting particle was Al_2O_3@C-COOH. Al_2O_3@C-Fluro NP has a zeta potential 3.18 ± 0.10 mV, which is expected for a hydrophobic, fluorinated surface species. Al_2O_3@C-N^+ has a zeta potential of -7.2 ± 0.5 mV, while it was expected to have a positive surface charge. XPS surface coverage of nitrogen indicates ~1 ligand/nm^2 of particle, so EDC coupling conditions could have led to lower ligand attachment of the quaternary ammonium, molecule, leaving some COOH exposed on the particle surface. Al_2O_3@C-BOC was deprotected using trifluoroacetic in dichloromethane to produce Al_2O_3@C-NH_2, with a zeta potential of +36.0 ± 0.8 mV.

The carbon coating on Al_2O_3 nanoparticles can be successfully functionalized using thermal-radical initiation and EDC coupling to produce a variety of particles with varying surface charges and chemical species.

3.4. Conclusion

The long-term control of chemical surface species on metal oxide nanoparticles is an important aspect when using them in complex biological systems. We have shown that a thin graphitic carbon surface can be applied to a variety of metal oxide nanoparticles through the thermal decomposition of adsorbed fatty acids without significant impact to core properties such as fluorescence. This carbon coating can then be further functionalized with ligands of varying charge and chemical composition through stable carbon and amide bonding. This carbon scaffold is an effective method for the long-term surface control of metal oxides, providing a powerful tool for further understanding the interactions of nanoparticles in biological systems.

3.5. Figures

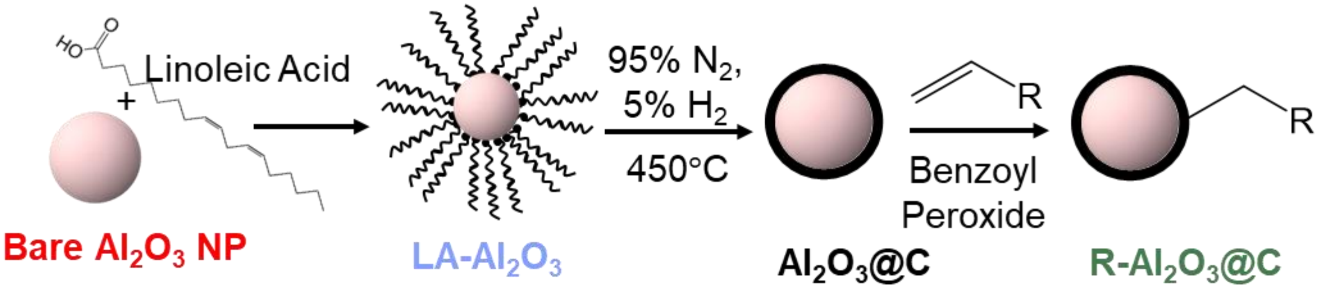

Scheme 3.1. Method to form stable carbon coating on metal oxide that can be further covalently functionalized using thermal radical initiator benzoyl peroxide.

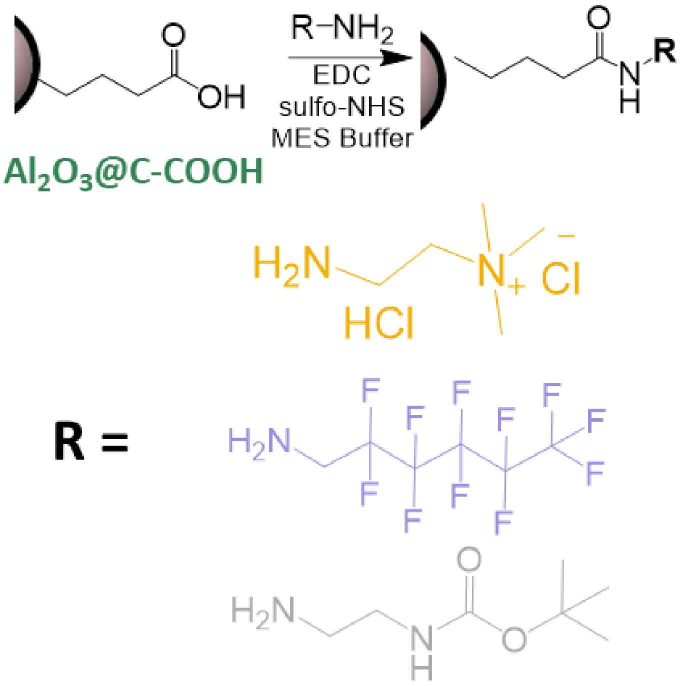

Scheme 3.2. EDC coupling of amine-terminated ligands to COOH on Al_2O_3@C surface forming stable amide bond.

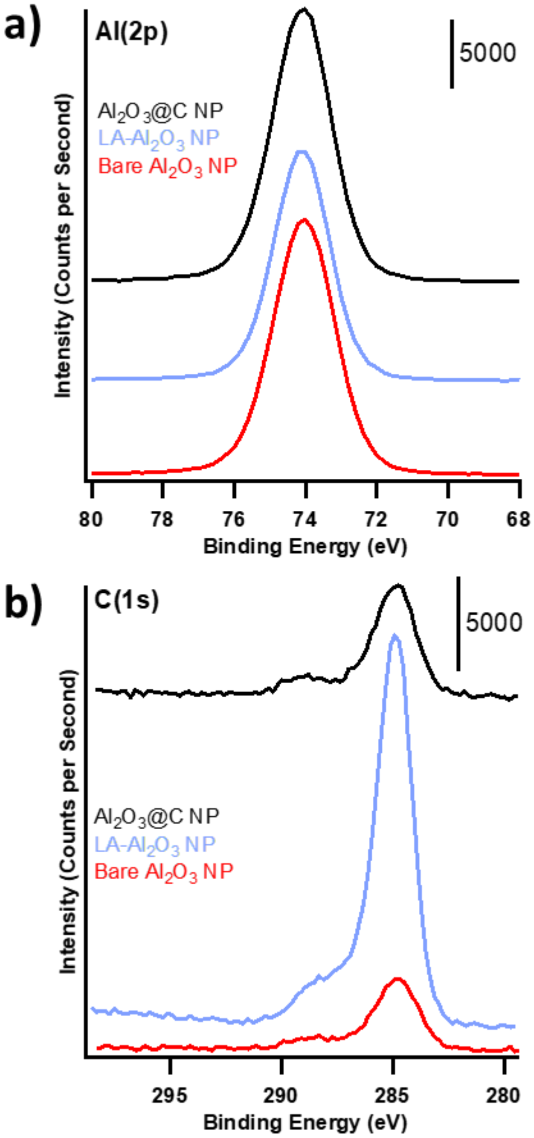

Figure 3.1. XPS spectra of (a) the Al(2p) region and (b) the (C(1s) region of Al_2O_3 NP untreated, after linoleic acid adsorption, and after carbonization.

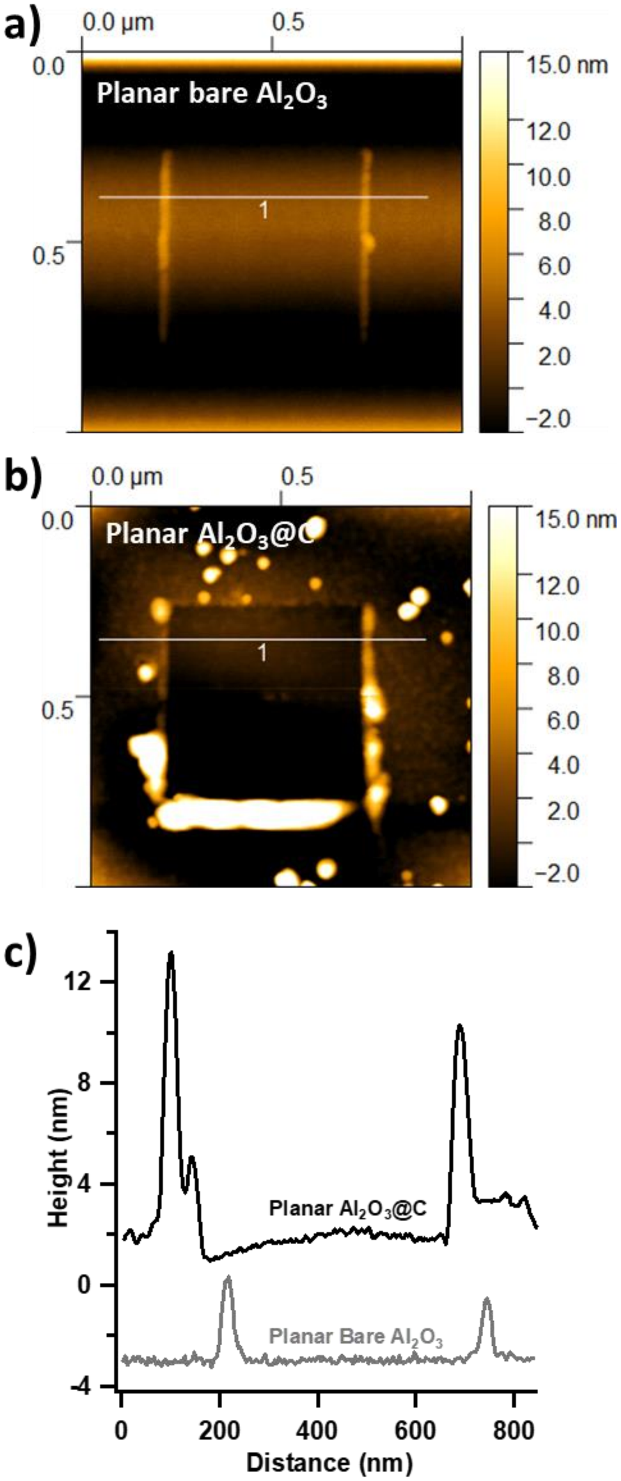

Figure 3.2. AFM images of (a) bare planar Al2O3 and (b) planar Al_2O_3@C, and (c) the corresponding lines scans.

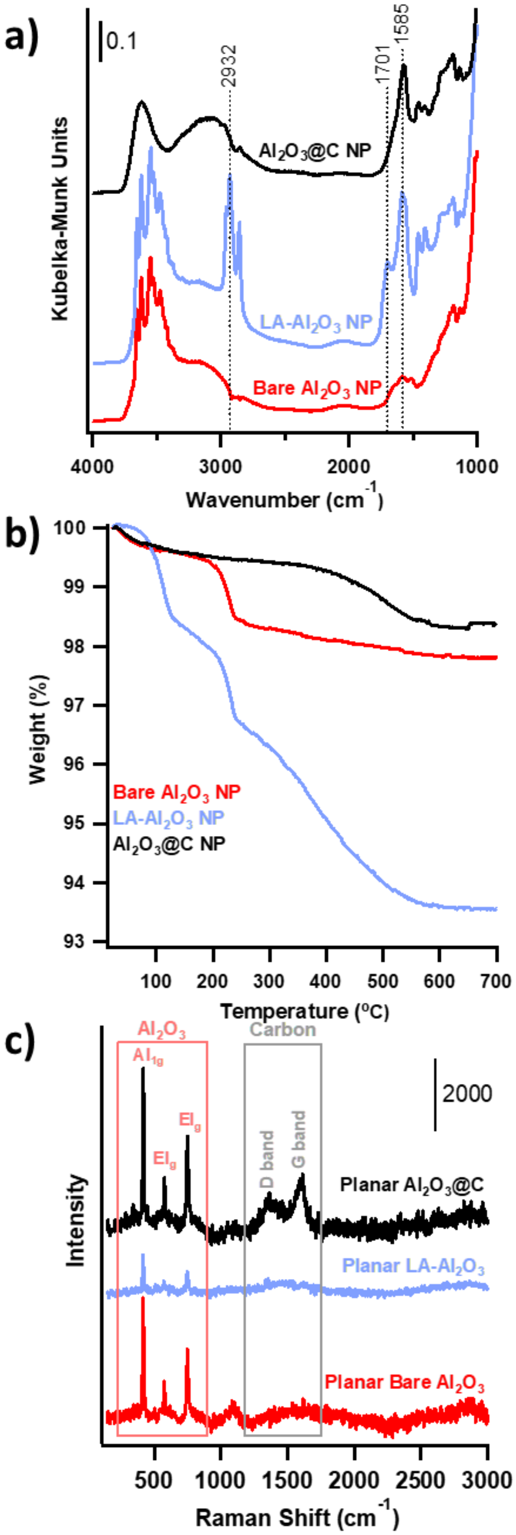

Figure 3.3. Analysis of Bare, LA-Al_2O_3, and Al_2O_3@C NP by (a) diffuse reflectance IR, (b) thermal gravimetric analysis, and (c) Raman spectroscopy.

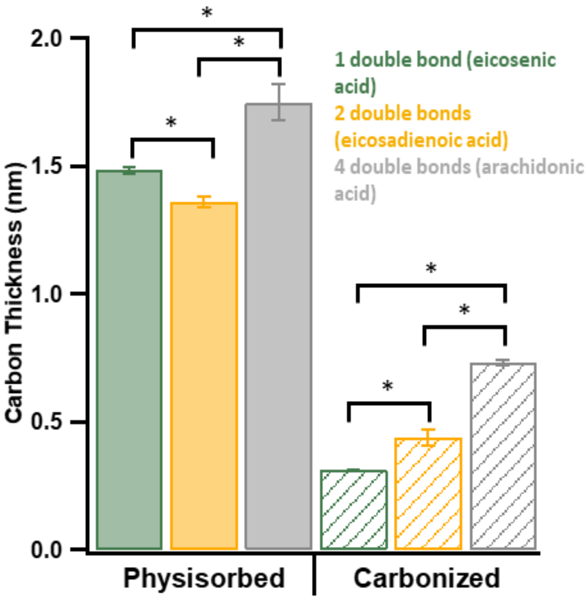

Figure 3.4. Carbon thickness calculated from XPS for fatty acids with chain lengths of 20 carbons and varying degrees of saturation before and after carbonization.

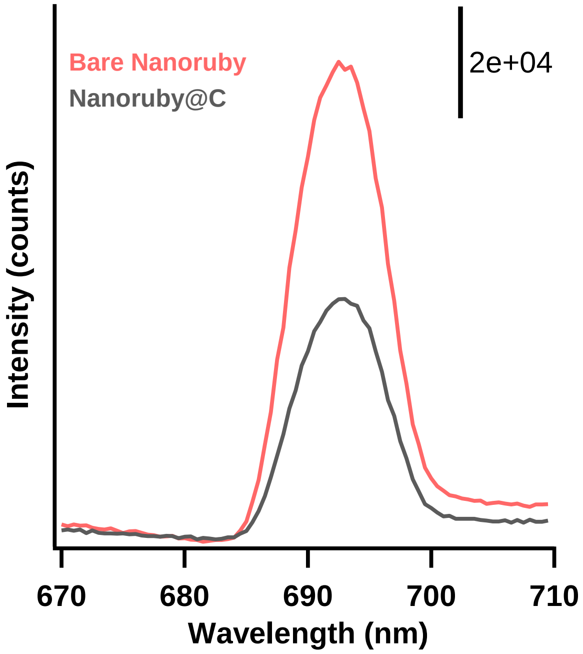

Figure 3.5. Fluorescence spectra of bare and carbonized nanoruby at ruby emission line.

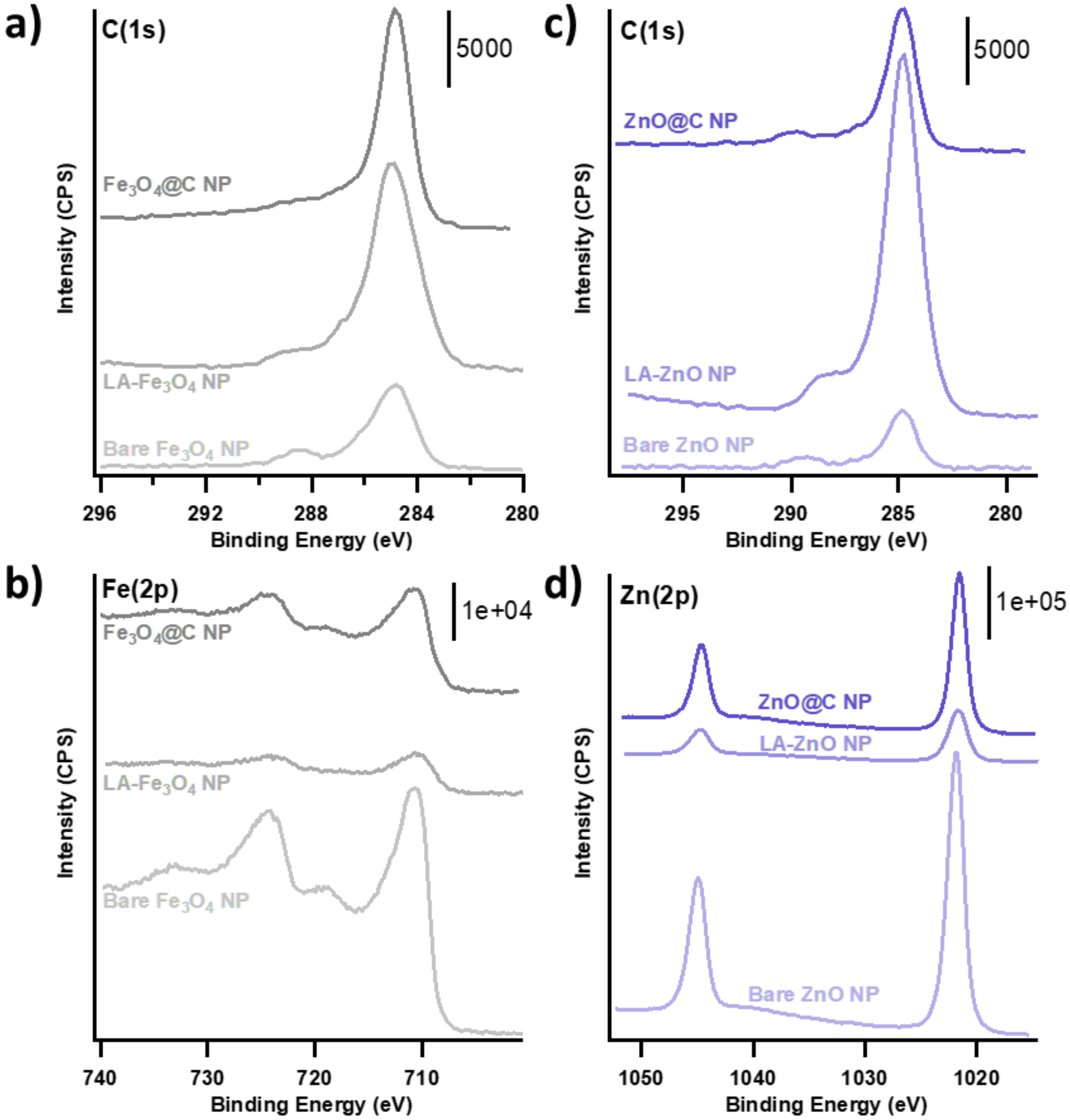

Figure 3.6. XPS spectra of Fe_3O_4 NP (a) C(1s) and (b) Fe(2p) regions and ZnO NP (c) C(1s) and (d) Zn(2p) regions for bare, LA-adsorbed, and carbonized particles.

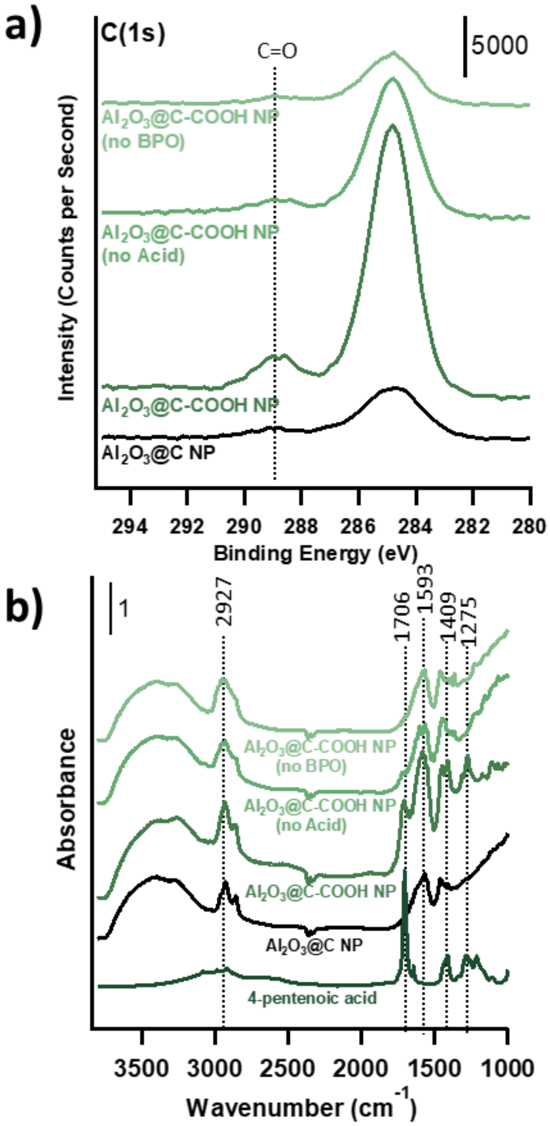

Figure 3.7. (a) XPS C(1s) region and (b) IR spectra for Al_2O_3@C NP and carboxylic acid functionalized Al2O3@C NP with controls.

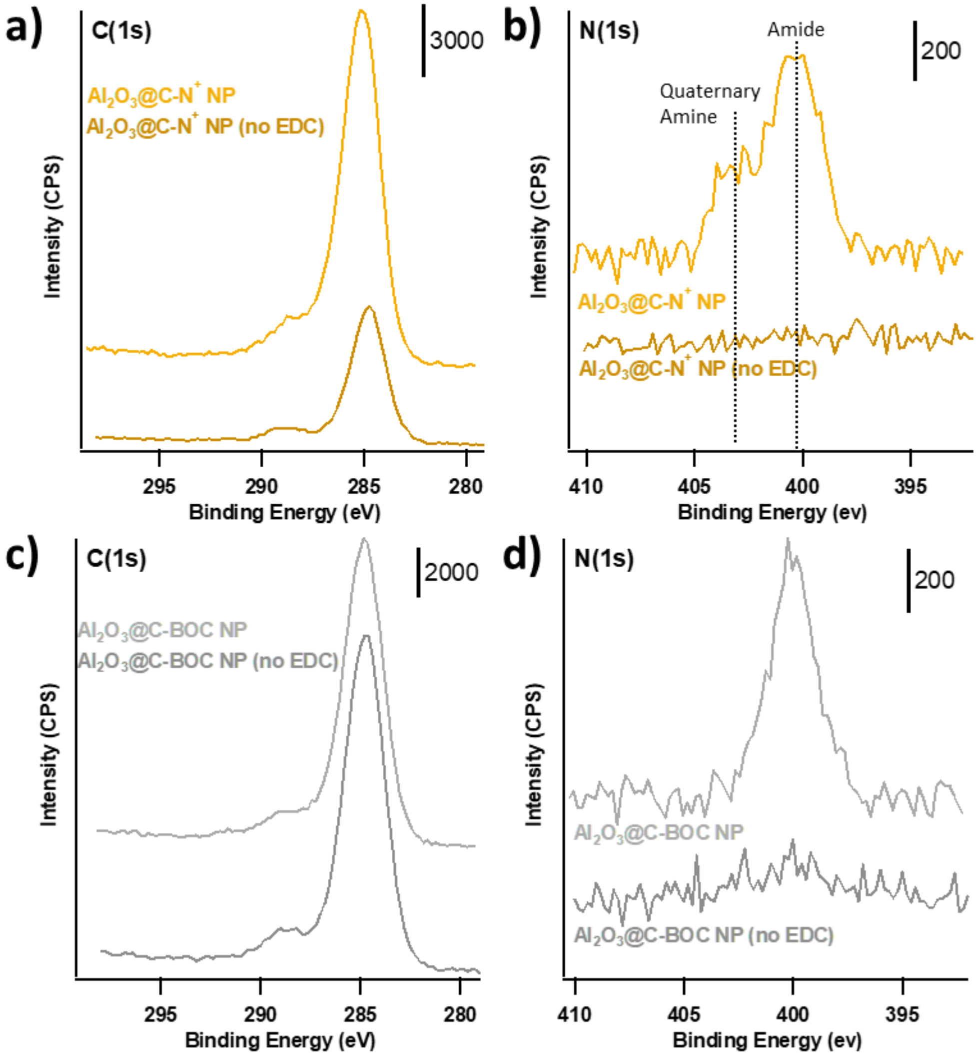

Figure 3.8. XPS spectra for Al$_2$O$_3$@C-N$^+$ NP (a) C1(s) and (b) N(1s) regions and Al$_2$O$_3$@C-BOC NP (c) C(1s) and (d) N(1s) regions.

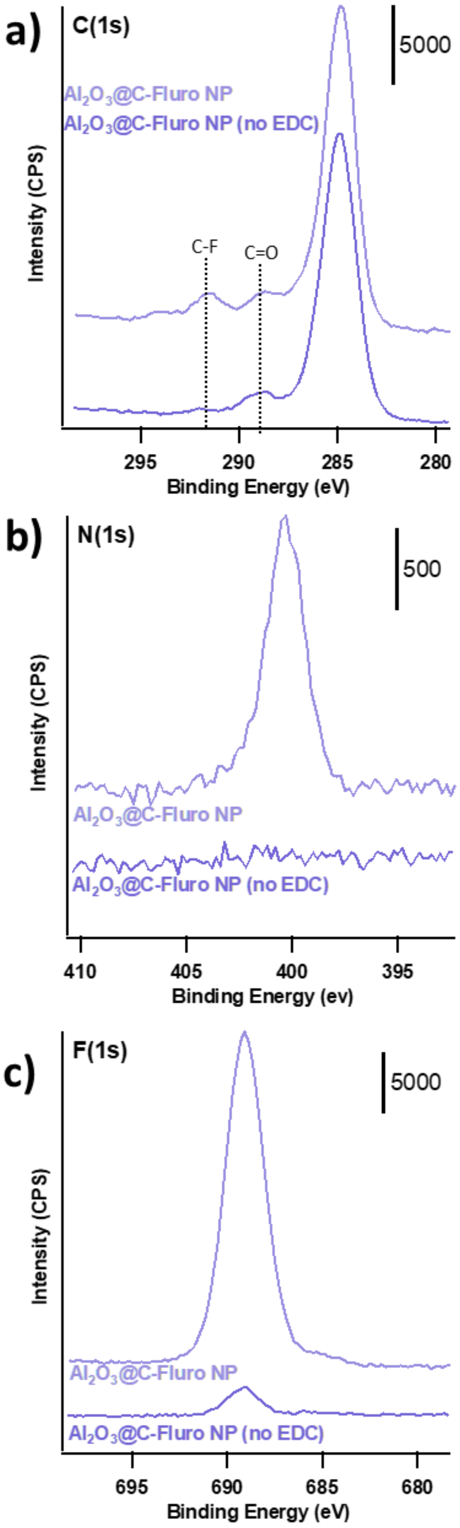

Figure 3.9. XPS spectra for (a) C(1s), (b) N(1s), and (c) F(1s) regions for Al_2O_3@C-Fluro NP.

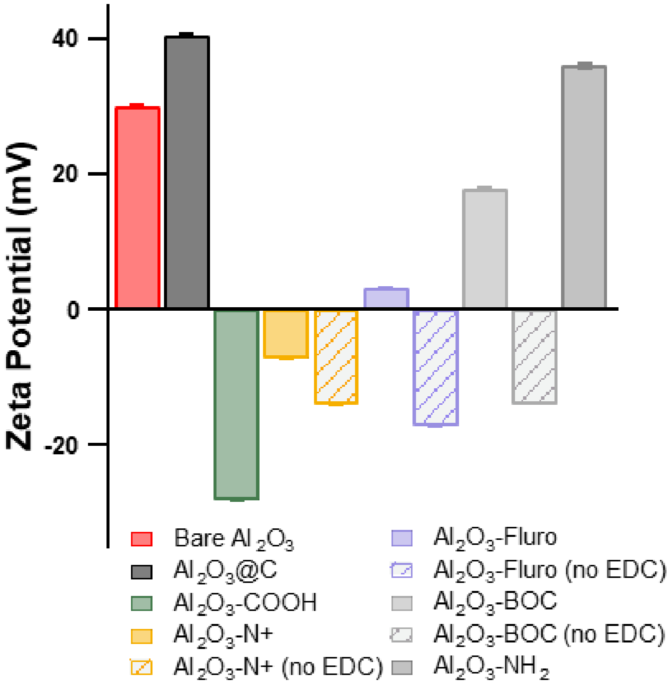

Figure 3.10. Comparison of zeta potentials for various secondary functionalizations of Al_2O_3@C NP.

Table 3.1. Comparison of carbon thicknesses measured from AFM and XPS for both planar and nanoparticle Al_2O_3

Sample	**Carbon thickness (nm)**		
	XPS – NP	**XPS – planar**	**AFM – planar**
Bare Al_2O_3	0.28±0.04	0.36±0.04	0.06±0.06
LA-Al_2O_3	1.23±0.06	2.33±0.3	--------------
Al_2O_3@C	0.40±0.06	0.77±0.16	0.82±0.42

Table 3.2. Carbon shell thickness calculated from XPS for nanoruby, Fe_3O_4 NP, and ZnO NP.

	Carbon Thickness (nm)		
Treatment	**Nanoruby**	**Fe_3O_4 NP**	**ZnO NP**
Bare/as-synthesized	0.44 ± 0.12	0.138 ± 0.006	0.16 ± 0.01
LA adsorbed	1.52	2.42 ± 0.11	2.03 ± 0.03
Carbonized (@C)	0.73 ± 0.13	2.04 ± 0.07	0.53 ± 0.02

3.6. References

1. Edmonds, A. M.; Sobhan, M. A.; Sreenivasan, V. K. A.; Grebenik, E. A.; Rabeau, J. R.; Goldys, E. M.; Zvyagin, A. V., Nano-Ruby: A Promising Fluorescent Probe for Background-Free Cellular Imaging. *Particle and Particle Systems Characterization* **2013,** *30* (6), 506-513.
2. Hoang, K. N. L.; Wheeler, K. E.; Murphy, C. J., Isolation Methods Influence the Protein Corona Composition on Gold-Coated Iron Oxide Nanoparticles. *Analytical Chemistry* **2022,** *94* (11), 4737-4746.
3. Servin, A.; Elmer, W.; Mukherjee, A.; De la Torre-Roche, R.; Hamdi, H.; White, J. C.; Bindraban, P.; Dimkpa, C., A review of the use of engineered nanomaterials to suppress plant disease and enhance crop yield. *Journal of Nanoparticle Research* **2015,** *17* (2), 1-21.
4. Mitchell, M. J.; Billingsley, M. M.; Haley, R. M.; Wechsler, M. E.; Peppas, N. A.; Langer, R., Engineering precision nanoparticles for drug delivery. *Nature Reviews Drug Discovery* **2021,** *20* (2), 101-124.
5. Weir, A.; Westerhoff, P.; Fabricius, L.; Hristovski, K.; von Goetz, N., Titanium Dioxide Nanoparticles in Food and Personal Care Products. *Environmental Science & Technology* **2012,** *46* (4), 2242-2250.
6. Neouze, M.-A.; Schubert, U., Surface Modification and Functionalization of Metal and Metal Oxide Nanoparticles by Organic Ligands. *Monatshefte für Chemie - Chemical Monthly* **2008,** *139*, 183-195.
7. Davis, K.; Cole, B.; Ghelardini, M.; Powell, B. A.; Mefford, O. T., Quantitative Measurement of Ligand Exchange with Small-Molecule Ligands on Iron Oxide Nanoparticles via Radioanalytical Techniques. *Langmuir* **2016,** *32* (51), 13716-13727.
8. Deblock, L.; Goossens, E.; Pokratath, R.; De Buysser, K.; De Roo, J., Mapping out the Aqueous Surface Chemistry of Metal Oxide Nanocrystals: Carboxylate, Phosphonate, and Catecholate Ligands. *JACS Au* **2022,** *2* (3), 711-722.
9. Kim, H.-S.; Kong, M.; Kim, K.; Kim, I.-J.; Gu, H.-B., Effect of carbon coating on LiNi1/3Mn1/3Co1/3O2 cathode material for lithium secondary batteries. *Journal of Power Sources* **2007,** *171*, 917-921.
10. Marcinek, M. L.; Wilcox, J. W.; Doeff, M. M.; Kostecki, R. M., Microwave Plasma Chemical Vapor Deposition of Carbon Coatings on LiNi1/3Co1/3Mn1/3O2 for Li-Ion Battery Composite Cathodes. *Journal of the Electrochemical Society* **2009,** *156* (1), A48-A51.
11. Saroha, R.; Panwar, A. K., Effect of in situ pyrolysis of acetylene (C2H2) gas as a carbon source on the electrochemical performance of LiFePO4 for rechargeable lithium-ion batteries. *Journal of Physics D: Applied Physics* **2017,** *50*, 255501.
12. Cao, Q.; Zhang, H. P.; Wang, G. J.; Xia, Q.; Wu, Y. P.; Wu, H. Q., A novel carbon-coated LiCoO2 as cathode material for lithium ion battery. *Electrochemistry Communications* **2007,** *9* (5), 1228-1232.

13. Zhang, Y.; Tamijana, A. A.; Taylor, M. E.; Zhi, B.; Haynes, C. L.; Mason, S. E.; Hamers, R. J., Molecular Surface Functionalization of Carbon Materials via Radical- Induced Grafting of Terminal Alkenes. *Journal of the American Chemical Society* **2019,** *141*, 8277-8288.
14. Allara, D. L.; Nuzzo, R. G., Spontaneously organized molecular assemblies. 1. Formation, dynamics, and physical properties of n-alkanoic acids adsorbed from solution on an oxidized aluminum surface. *Langmuir* **1985,** *1* (1), 45-52.
15. Kang, Y. S.; Risbud, S.; Rabolt, J. F.; Stroeve, P., Synthesis and characterization of nanometer-size Fe3O4 and γ-Fe2O3 particles. *Chemistry of Materials* **1996,** *8* (9), 2209-2211.
16. Rani, G.; Sahare, P. D., Structural and photoluminescent properties of Al2O3:Cr3+ nanoparticles via solution combustion synthesis method. *Advanced Powder Technology* **2014,** *25* (2), 767-772.
17. Bachman, B. F.; Jones, Z. R.; Jaffe, G. R.; Salman, J.; Wambold, R.; Yu, Z.; Choy, J. T.; Kolkowitz, S. J.; Eriksson, M. A.; Kats, M. A.; Hamers, R. J., High-Density Covalent Grafting of Spin-Active Molecular Moieties to Diamond Surfaces. *Langmuir* **2021,** *37* (30), 9222-9231.
18. Sehgal, D.; Vijay, I. K., A Method for the High Efficiency of Water-Soluble Carbodiimide-Mediated Amidation. *Analytical Biochemistry* **1994,** *218* (1), 87-91.
19. Shirley, D. A., High-Resolution X-Ray Photoemission Spectrum of the Valence Bands of Gold. *Physical Review B* **1972,** *5* (12), 4709-4714.
20. Barr, T. L.; Seal, S., Nature of the use of adventitious carbon as a binding energy standard. *Journal of Vacuum Science & Technology A: Vacuum, Surfaces, and Films* **1995,** *13* (3), 1239-1246.
21. Franking, R. A.; Landis, E. C.; Hamers, R. J., Highly Stable Molecular Layers on Nanocrystalline Anatase TiO2 through Photochemical Grafting. *Langmuir* **2009,** *25* (18), 10676-10684.
22. Iwaki, M., Estimation of the atomic density of amorphous carbon using ion implantation, SIMS and RBS. *Surface and Coatings Technology* **2002,** *158-159*, 377-381.
23. Powell, C. J.; Jablonski, A., NIST Electron Effective-Attenuation-Length Database Version 1.3. National Institute of Standards and Technology: Gaithersburg, MD, 2011.
24. Seat, H. C.; Sharp, J. H., Dedicated Temperature Sensing With C-Axis Oriented Single-Crystal Ruby (Cr3+:Al2O3) Fibers: Temperature and Strain Dependences of R-Line Fluorescence. *IEEE Transactions on Instrumentation and Measurement* **2004,** *53* (1), 140-154.
25. Torelli, M. D.; Putans, R. A.; Tan, Y.; Lohse, S. E.; Murphy, C. J.; Hamers, R. J., Quantitative Determination of Ligand Densities on Nanomaterials by X-ray Photoelectron Spectroscopy. *ACS Applied Materials & Interfaces* **2015,** *7* (3), 1720-1725.
26. Socrates, G., *Infrared and Raman Characteristic Group Frequencies: Tables and Charts*. 3rd ed.; Wiley: 2004.
27. Nolin, B.; Jones, R. N., The infrared absorption spectra of deuterated esters: II. ethyl acetate. *Canadian Journal of Chemistry* **1956,** *34* (10), 1392-1404.

28. Li, J.; Liu, J.; Sun, X.; Liu, Y., The mathematical prediction model for the oxidative stability of vegetable oils by the main fatty acids composition and thermogravimetric analysis. *LWT* **2018,** *96*, 51-57.

29. Lewis, I., Chemistry of pitch carbonization. *Fuel* **1987,** *66* (11), 1527-1531.

30. Ferrari, A. C.; Robertson, J., Raman spectroscopy of amorphous, nanostructured, diamond–like carbon, and nanodiamond. *Philosophical Transactions of the Royal Society of London. Series A: Mathematical, Physical and Engineering Sciences* **2004,** *362* (1824), 2477-2512.

31. Pezzotti, G.; Zhu, W., Resolving stress tensor components in space from polarized Raman spectra: polycrystalline alumina. *Physical Chemistry Chemical Physics* **2015,** *17* (4), 2608-2627.

32. Seat, H. C.; Sharp, J. H., Dedicated temperature sensing with c-axis oriented single-crystal ruby (Cr/sup 3+/:Al/sub 2/O/sub 3/) fibers: temperature and strain dependences of R-line fluorescence. *IEEE Transactions on Instrumentation and Measurement* **2004,** *53* (1), 140-154.

33. Zhang, Z.; Grattan, K. T. V.; Palmer, A. W., Temperature dependences of fluorescence lifetimes in ${\mathrm{Cr}}^{3+}$-doped insulating crystals. *Physical Review B* **1993,** *48* (11), 7772-7778.

34. Shebanova, O. N.; Lazor, P., Raman spectroscopic study of magnetite (FeFe2O4): a new assignment for the vibrational spectrum. *Journal of Solid State Chemistry* **2003,** *174* (2), 424-430.

35. Owens, F. J.; Orosz, J., Effect of nanosizing on lattice and magnon modes of hematite. *Solid State Communications* **2006,** *138* (2), 95-98.

36. Shebanova, O. N.; Lazor, P., Raman study of magnetite (Fe3O4): laser-induced thermal effects and oxidation. *Journal of Raman spectroscopy* **2003,** *34* (11), 845-852.

37. Chastain, J.; King Jr, R. C., Handbook of X-ray photoelectron spectroscopy. *Perkin-Elmer Corporation* **1992,** *40*, 221.

Chapter 4: Impact of multifaceted interactions in community-engaged learning course on personal and professional STEM identity growth in undergraduates

A manuscript of this work is in preparation and will be submitted to *Science Education & Civic Engagement*, in collaboration with Evan Heintz (UW-Madison, Physics) and Anna M. Bishop Courtier (UW-Madison, WISCIENCE).

4.1. Introduction and Course Overview

Community-engaged learning (CEL) integrates student learning in courses with community experiences. CEL is based upon partnerships between the university and community that are mutually beneficial for students and community, deepening students' understanding of and connection to their local community and addressing community-identified needs.[1,2] For undergraduate STEM majors, this community connection is of particular importance. As currently taught, many undergraduate STEM courses focus on learning fundamentals and foundations of a subject, infrequently turning outward to think about implications and connections to the broader world.[3] This societal connection not only enhances engagement and learning of students, but also pushes students to think about why science is done and who it ultimately serves.

Service with Youth in STEM (SWYiS) is a sequence of undergraduate courses offered by the Wisconsin Institute for Science Education and Community Engagement (WISCIENCE) and is designated as a community-engaged learning course at the University of Wisconsin-Madison (UW). The sequence is designed to teach students best practices in community engagement and partnership. This is paired with experiencing the importance of relationship building and reflection in science communication and teaching. Alongside learning these tools, students develop a better understanding of their personal and STEM identities and the interplay of service and science.

4.2. Course Description and Context

Students are introduced to SWYiS through Integrated Science (IntegSci) 240. This course is structured with three main components: lecture, lab, and community engagement. In this case, the community engagement portion is through student-led after-school science clubs at local elementary schools or community centers. To distinguish the difference between "students," participants in SWYiS will be referred to as "UW students" and children in the after-school science clubs will be referred to as simply "students" or "elementary students," depending on the context.

Academically, a primary goal of the lecture component of this course is to provide the communication skills, cultural competency, and personal and social awareness necessary to build effective community partnerships. The course is a seminar-style, active-learning environment where UW students discuss the practices and examples of community engagement, as well as explore their own personal identities and communities through reflection. It is intentionally limited to a small number of students with a goal that a learning community will be developed, and UW students become willing to be more vulnerable and authentic in their conversation.[a]

---

[a] Due to the small size of the classes in the SWYiS sequence, any analyses or quotes included here are from anonymous course evaluations over multiple semesters and redacted, if necessary, to protect student anonymity and avoid any potentially identifiable information.

During the lab portion of the course, the UW students learn and experiment with science activities that they will teach elementary students during after-school science clubs. The activities are structured around an annual (academic year) theme, such as Energy, Astronomy, or Water. The themed structure allows the UW students to engage with concepts that are part of their general requirements as STEM majors but may be ideas that they have not worked with recently. It also pushes them to think about activities from a multi-disciplinary lens by collaborating with students who come from other STEM disciplines.

Finally, each UW student is partnered with a local community center or elementary school to lead a weekly after-school science club, generally attended by groups of 5 to 15 elementary students. The annual scientific themes allow elementary students to see topics that they may have struggled with (or not had an opportunity to learn about) in school, to explore and engage with the concepts in a new way, and to connect weekly activities to previous ones. Ideas that they may have seen as disconnected are threaded throughout the students' experiences and they often refer back to an older activity in the middle of discovering how a new idea works. While the course is only a semester long, the next group of UW students continues with new activities within the annual theme, because the same elementary students are in the after-school program for the entire academic year. A different UW student often works at the site the following semester, and at that point the students are engaged in the science clubs and excited to meet a new leader for the semester.

In preparation for the after-school science clubs, activities the UW students learn each week in lab are designed to be open ended. Often, they will be handed the materials in lab with the instruction of "just play and see what you find." While the activities may seem basic or very short, UW students are given this "play-time" with the activities, both through role play and individual discovery, and often come up with new ways to structure the activity or connect it to another activity that has been used before. This allows the lab to become much less based upon rigid lesson plans, but rather uses those lesson plans as a starting point for the UW students to further develop and customize how they may do an activity in an after-school club. They get a feel for how much structure is needed to successfully implement an activity with elementary students, or where creativity can be harnessed to let kids explore and discover. Instructors dedicate the last part of lab to discuss and debrief lessons learned about the activity, both in regards initial engagement strategies, types of experiments they could lead, and how to ensure the activity is accessible to community members (with regard to language, physical ability, cultural context, and age, among others).

The weekly format of SWYiS provides the opportunity for UW students to directly and intentionally connect lessons learned in lecture and lab to the local community. The course is structured such that UW students bring back stories of successes and failures to class to share with their peers. Each week, the UW student has the agency to select which activity will be done in their science club. This means that all clubs engage in the same activities but not always in the same order. The discussion often originates as something related to the activity itself, and connections back to lecture content are also made. Since the specific weekly activity done at each club is chosen by the UW student, the opportunity for this debrief of successes and failures is a crucial component of lab discussions and improves the success of activities used in the future at other sites:

> *"New people bring new ideas …. In a course like this, discussion with other people about their experiences can greatly improve my technique. With more people to talk with, there is a greater chance of somebody finding tricks and tips that are very successful."*

4.3. Continued Academic Involvement and Mentoring

Many IntegSci 240 students enjoy the off-campus community component and want to continue involvement with after-school science clubs. After taking IntegSci 240, students are able to come back in following semesters and take IntegSci 341 ("Service with Youth in STEM Practicum"). This allows UW students to continue participating with after-school science clubs that are part of the community-based learning component, applying practical application of concepts learned in 240, without duplicating material learned in the IntegSci 240 lecture. Returning UW students also work with different community partners, allowing them to face new challenges and opportunities for growth. Since the themes of the activities change from year to year, the returning UW students are introduced to new lesson plans and can explore and develop activities in the same way as students who are taking the course for the first time. Returning students have gained strategies to pose meaningful questions to the students in the after-school clubs and more independently assess understanding and impact of lessons that focus on new topics. They are asked to provide insight about leading clubs and teaching activities to the 240 students based on their past experiences, and in doing so, gain informal mentoring experiences.

Another option for returning students is to participate as Peer Leaders in the class. Peer Leaders (PL; enrolled in IntegSci 320: "Independent Study") attend both lecture and lab for 240, acting as mentors for new students and facilitating small group discussion. Peer Leaders also have the opportunity to develop and lead lectures and labs alongside the instructor. In order to become a PL, the student must have already completed the introductory level of SWYiS and must also take another class offered by WISCIENCE: Integrated Science 230: Discipline-Based Leadership and Mentoring. They have weekly preparation meetings or discussions with the instructor and do brief weekly post-class reflections. These post-class reflections are a collaborative conversation held either in-person or through a messaging system like Slack. Peer Leaders may choose to run an after-school science club if they would like, but it is not a requirement. The curricular SWYiS course sequence, community-involvement, and leadership is outlined in Table 4.1.

4.4. Fluidity of the Lab, Lecture, Community, and Mentoring Structure

The course is not unidirectional but an intertwined experience that varies from week to week and student to student. While the course description above may imply a hierarchical system of (UW) student, informal mentor, peer leader, and instructor, the content and style of the course is student-driven, illustrated in Figure 4.1. Those with more experience facilitate and encourage others only when needed. A key to this interconnectedness is that it can happen in any order and loop through any component or by any member of the class community at any time. Personal reflection is emphasized early in lecture and appears in some form in almost every component of the UW students' experiences.

The structure of "Lecture - Lab - Community" mentioned above may be more accurately described as a fully integrated experience of "*Learn, Experience, Reflect, Grow, Continue*." The key to the growth of the UW students participating in SWYiS students during the semester is the interconnectedness of the course components as well as the students' willingness to be open, vulnerable, and respectful, whether it be in discussions in lecture or breaking down the way an activity was implemented.

Because UW students lead 6-10 weeks of after-school science clubs, they have the opportunity to apply ideas from lecture and lab multiple times, adapting and improving as they go, and incorporating new lessons learned and discussed throughout the semester. Perhaps more importantly, most clubs have students that return every week. UW students who participate in SWYiS are equipped to develop relationships with these students, building trust and more impactful connections. By returning to the same site every week, the UW students also develop a better understanding about the local community, the backgrounds of their students, as well as their individual interests. UW students can then adapt the activities learned in lab to the needs and interests of their students to make a more engaging and meaningful science learning experience.

Principles of engagement and science communication that are discussed in both lecture and lab can also be practiced and honed at the after-school science clubs. Discussions about identity, stereotype threat, and microaggressions in lecture help students to realize their own positionality and to be both self-aware and actively present in the community. Students have recognized this in course evaluation reflections.

> *"I was … reminded of how students first react to concepts surrounding privilege, understanding who you serve, and the complexity that can go into running after-school science clubs."*
>
> *"Having a good understanding of self-identity and who we serve has allowed me to continue to focus on honing practical skills when running clubs."*

Recognition of the importance of identity in the context of this program, and science in general, is also seen in quantitative course evaluations. Over the course of several semesters, 100% of students in the participating in the SWYiS program report that the course has broadened their understanding in this area (Figure 4.2).

Alongside making connections between identity and science participation in general, over 95% of students who participate in SWYiS strengthened their own STEM identities, regarding their abilities as either STEM teachers or researchers (Figure 4.3), with potential long-term impact of whether they decide to stay within in STEM field in the future. Based on the reports of identity shift, we will continue to incorporate those components in the class and ensure they are included in course outcomes.

Along with the on-going informal reflections discussed earlier, the class has a number of guided reflections built in throughout the semester. Early in the semester, students reflect on their previous service experiences and are asked to look at them through the lens of community engagement and understanding who you serve. They consider how those thoughts might inform their relationships with students and staff at their after-school site. Later, students may reflect on such things as communication or leadership, and the growth they have seen in themselves. At the end of the semester they are asked to reflect on one of several possibilities where they felt the most growth or impact: self-awareness, interpersonal communication, honoring culture and context, decision making, or fostering collaborations, which are components of the UW Leadership Framework.[4]

As part of a final portfolio, the students are asked to put together a 5-minute presentation on their experiences during clubs presented to the class as well as community partners. They reflect on connections with their club students and what made them so impactful, as well as influence on their own personal and professional identities. These presentations push the students to connect lessons learned in class and experiences participating in the after-school science clubs in the community. The second part of their portfolio asks students to design an activity based on the scientific theme of the year. They are pushed to think about initial engagement strategies, accessibility, and experimental design, and how they might present all these things to future instructors. Finally, the third part of the portfolio asks students to put together a public engagement plan, asking them to reflect how they will continue to engage with the community and do public service after the course is finished.

Through reflection and teaching and learning interactions both on- and off-campus, the UW students report growth in their confidence in STEM in general (Figure 4.4). This is particularly important for STEM undergraduate students who might only be taking classes and learning new information. Having confirmation of both their knowledge in a subject and being able to communicate that knowledge was impactful, and the return rate of students who continue on to participate in IntegSci 341 (approximately 33% pre-Covid) demonstrates motivation to continue to engage in the realm of science engagement.

> *"It was really empowering to experience how my confidence had grown over time, ... to experience being at least partially liberated from that fear, and then be able to actually just focus on implementing good teaching methods."*

Perhaps in part thanks to confidence gained and validation in their teaching and comprehension abilities in science, UW students report finding a sense of belonging in the STEM community (Figure 4.5). This is especially important for students who might be feeling imposter syndrome or have been struggling in challenging classes. The sense of belonging they develop as part of this class can have long-term effects on whether they decide to stay in science.[5, 6]

> *"I think this course was very beneficial to my growth as a STEM major and I am so happy I took this class."*

4.5. Conclusion

Service with Youth in STEM provides students frameworks of engagement and reflection that allow them to immediately apply them in the community. It gives students the opportunity to learn and reflect by implementing and iterating not only tangible activities from lab but also community-based concepts and communication strategies from lecture. Students can see real-time impacts and results of how they chose to engage with students and have the opportunity to reflect and assess how the engagement went. That they have many opportunities to go into the community throughout the semester means that they are able to grow as teachers, science communicators, and community members. Because the course is semester long, UW students are able to build relationships at community sites with students and staff, creating deeper more impactful connections for both UW students and the club students. If something unexpected happens while in the community, students can bring that to the class, reflect on what happened, and then brainstorm new possibilities and opportunities for next time - whether “next time” is implementing the next activity in their own club, a fellow student who will be doing the activity discussed in the future, or a topic for discussion in lecture. By building a community with their peers, they create a network of thinkers and learners who have the context to solve each other’s problems and provide creative solutions that one might not come to alone. Allowing students the freedom to workshop and think about how best to teach activities during lab, they are able to find pitfalls themselves and take ownership and find expertise on how to teach, lead, and have a positive impact in the local community.

4.6. Figures

Table 4.1. Sequence progression of Service with Youth STEM over multiple semesters.

IntegSci 240 (New Students)	2 Credits	Lecture	Lab	Club
IntegSci 341 (Returning students)	1Credit	-	Lab	Club
IntegSci 320 (Peer Leaders)	1 Credit	Lecture	Lab	Optional Club

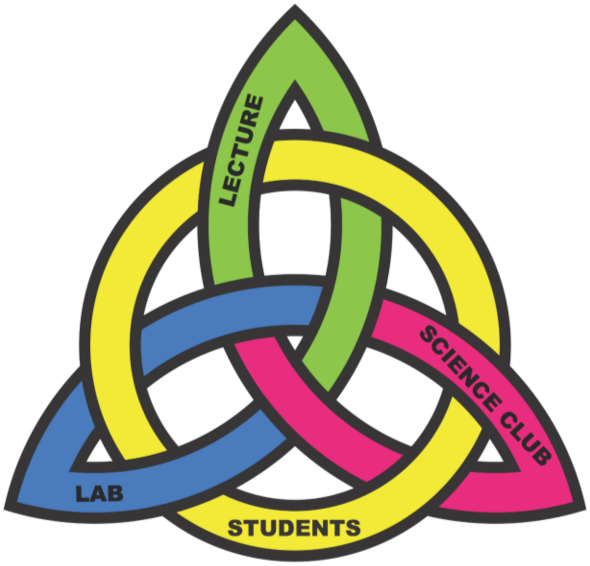

Figure 4.1. Illustration of the interconnectedness of SWYiS between all class components, driven by and focused around student participation.

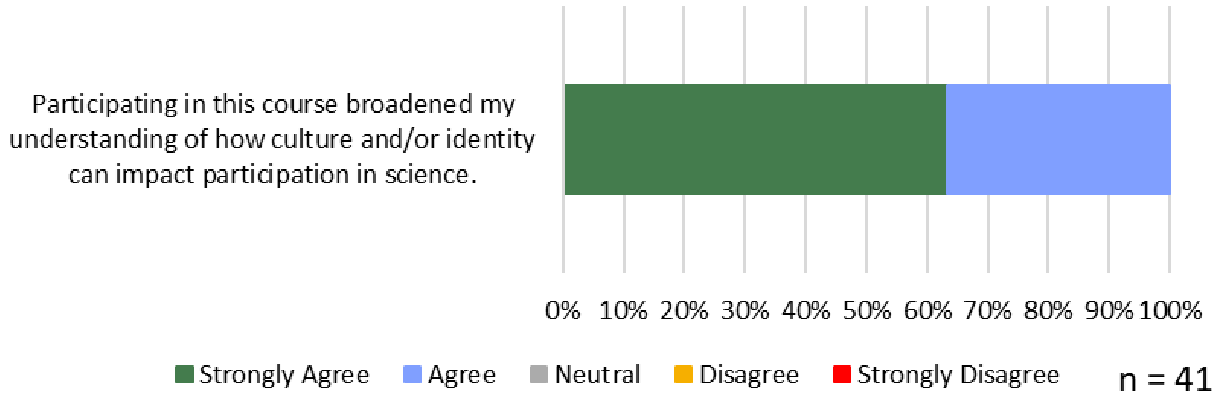

Figure 4.2. Student responses over 4 semesters when asked about the connection between identity and participation in science.

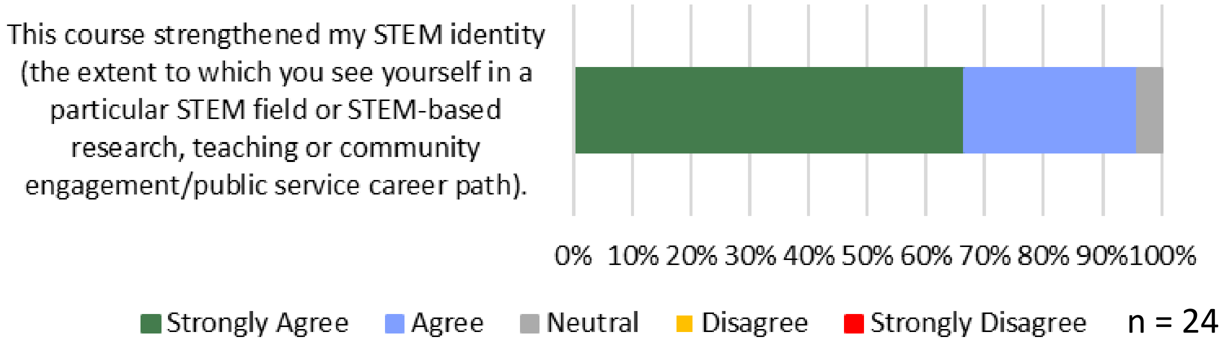

Figure 4.3. Student responses over 4 semesters when asked about the changes or growth in their STEM identities.

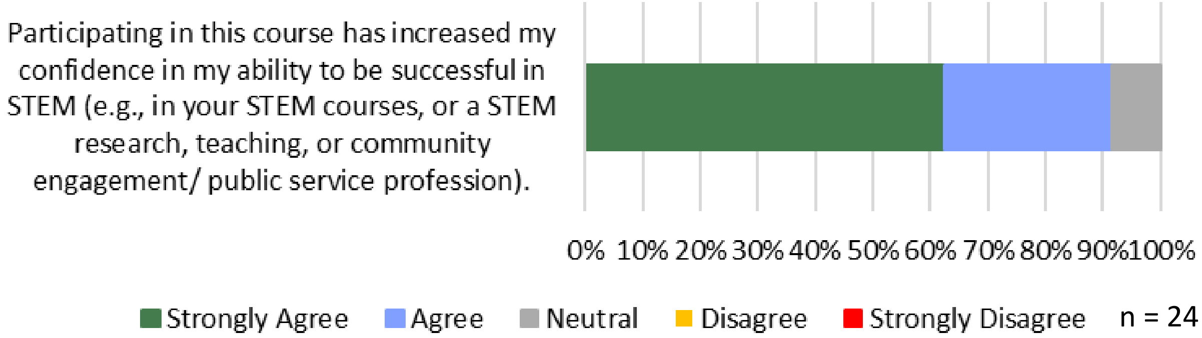

Figure 4.4. Student responses over 4 semesters when asked their confidence in the success in STEM in general.

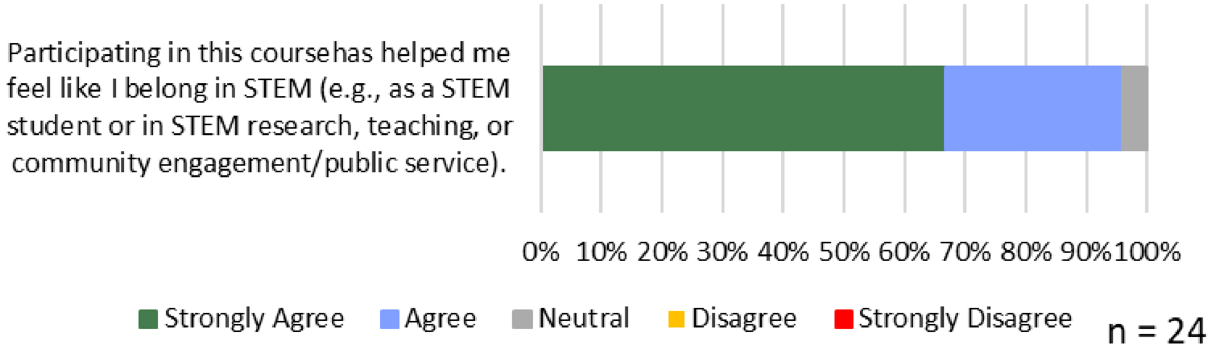

Figure 4.5. Student responses over 4 semesters when asked about their sense of belonging in STEM and how SWYiS has impacted it.

4.7. References

1. What is community-based learning? https://www.colorado.edu/cuengage/about-us/what-community-based-learning.

2. Furco, A., Service-learning: A balanced approach to experiential education. **1996**.

3. Flener-Lovitt, C., Using the Socioscientific Context of Climate Change To Teach Chemical Content and the Nature of Science. *Journal of Chemical Education* **2014,** *91* (10), 1587-1593.

4. Leadership Framework. https://leadership.wisc.edu/leadership-framework/.

5. Hoyt, J. E.; Winn, B. A., Understanding Retention and College Student Bodies: Differences Between Drop-Outs, Stop-Outs, Opt-Outs, and Transfer-Outs. *NASPA Journal* **2004,** *41* (3), 395-417.

6. Tomasko, D. L.; Ridgway, J. S.; Waller, R. J.; Olesik, S. V., Association of Summer Bridge Program Outcomes With STEM Retention of Targeted Demographic Groups. *Journal of College Science Teaching* **2016,** *45* (4).

Chapter 5: Conclusions and Future Directions

Carbon coatings provide a versatile handle on surface control of materials. The variability in deposition method and carbon precursors allows us to deposit tunable carbon coatings on different materials with entirely different functionalities. Application of carbon coatings allows us to control reactivity and functionality of material surfaces.

Red phosphorus falls on the side of reactivity for materials. It is a material used as a flame retardant and pyrotechnic obscurant but when exposed to a humid atmosphere, it begins to break down into toxic phosphine gas and acidic phosphorus species. We showed that the application of a nanometers-thick carbon coating by plasma deposition of acetylene gas has significant impact of slowing the degradation of red phosphorus powder. Combining the quantification of phosphine gas by infrared spectroscopy with chemical surface analysis by X-ray photoelectron spectroscopy, we built a picture of how the plasma-deposited carbon passivates the red phosphorus surface, providing a solution for long-term stability of red phosphorus.

In future experiments, we are interested in understanding the impact of the plasma-deposited carbon coating on the application of red phosphorus for its intended function. Specifically, we want to look out how the coating impacts the burnability of red phosphorus for its application of a pyrotechnic obscurant.

Carbon coatings can also be used to control the surface functionalization of materials. Metal oxide nanomaterials are of interest in studying the interactions of nanoparticles in complex biological systems, whether through optical tracking using fluorescent nanoruby, studying protein interactions using superparamagnetic iron oxide, or delivering micronutrients to plants using zinc oxide. However, long-term stable control of metal oxide surfaces is challenging. We developed a method to apply a thin graphitic carbon coating on various metal oxide nanoparticles through the adsorption and then carbonization of fatty acids. This carbon surface can be further functionalized with ligands of a variety of chemical and charge characteristics through stable carbon-carbon and amide linkages. This carbon platform offers a method for stable, long-term surface control of metal oxide nanomaterials, providing a powerful tool for gaining a deeper understanding of the interactions of nanomaterials in the environment.

For next steps, we are interested in using functionalized nanoruby as an optical tracker in plants. Nanomaterial uptake is plants is a challenge to track because of the complexity of the system. Using nanoruby, with its bright emission and long phosphorescence lifetime, would allow for in situ tracking of nanomaterial interactions. Nanoruby functionalized with positive and negative ligands could help us see how and where materials go once on a plant.

Finally, alongside my research on the impact of carbon coatings, I also looked at the impact of the community-engaged learning course Service with Youth in STEM. This course provides a multifaceted model for student learning, community engagement, and STEM identity growth, alongside opportunities for mentorship. We found that the structure of the course improved student confidence in science and their own science identities.

We want to broaden our understanding of the impact of the class in future assessments, tracking the retention of SWYiS alumni in STEM fields. Additionally, we want a deeper understanding of the impact of the course on our community partners and the students they serve.

Appendix 2: Supplementary Information for Chapter 2: Reactivity passivation of red phosphorus with thin plasma-deposited carbon coating

A.2.1. X-ray photoelectron spectroscopy: additional calculations

We needed to correct for passage of electrons through carbon shell in equation 2.4. For PDC RP, the elemental P emissions must pass through a carbon shell coating, resulting in some signal attenuation due to scattering and absorption. We have utilized a scaling factor, F, to correct for the attenuation induced by the carbon shell. This scaling factors enables us to directly compare emission intensities between coated and uncoated, and aged and nonaged RP. For this correction, we first experimentally determined the attenuation of the P(2p) emission intensity induced by the carbon layer of the appropriate thickness by measuring the absolute P(2P) intensity from uncoated and coated, non-aged samples:

$$F = \frac{Area_{P,coated}}{Area_{P,uncoated}} \qquad \text{(A.2.1)}$$

Dividing the experimentally obtained elemental P area (Area$_P$) by the scaling factor F gives a corrected area that corresponds to the elemental P(2p) signal without attenuation by carbon coating:

$$Corrected\ Area = \frac{Area_P}{F} \qquad \text{(A.2.2)}$$

This corrected area can then be used in equation 2.4 to calculate %POx of P(2p) signal and compare across samples (uncoated and coated, non-aged and aged).

A.2.2. Additional Figures

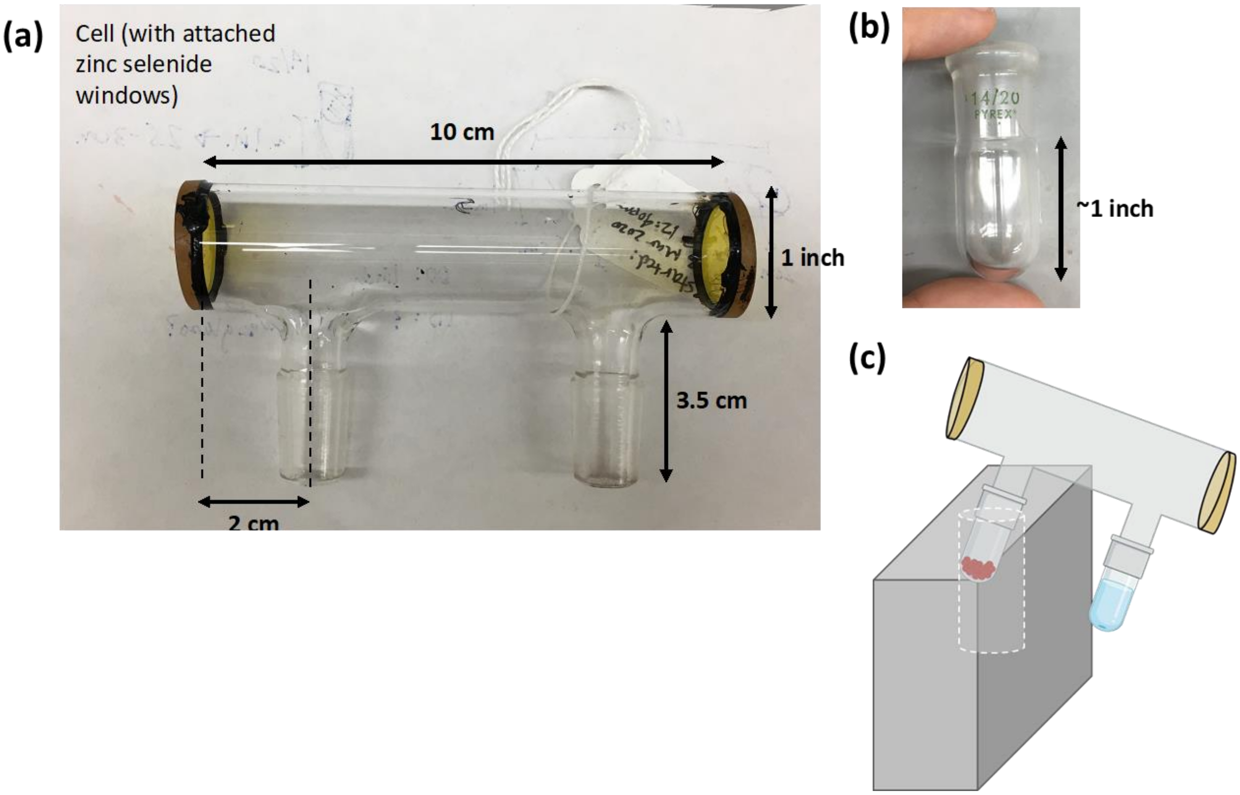

Figure A.2.1. (a) IR gas phase cell with dimensions, (b) sample bulb used to hold red phosphorus or ultrapure water during gas phase IR experiments, and (c) experimental set up for aging red phosphorus with IR cell placed in aluminum holder with cylindrical hole in which side of cell containing red phosphorus was set.

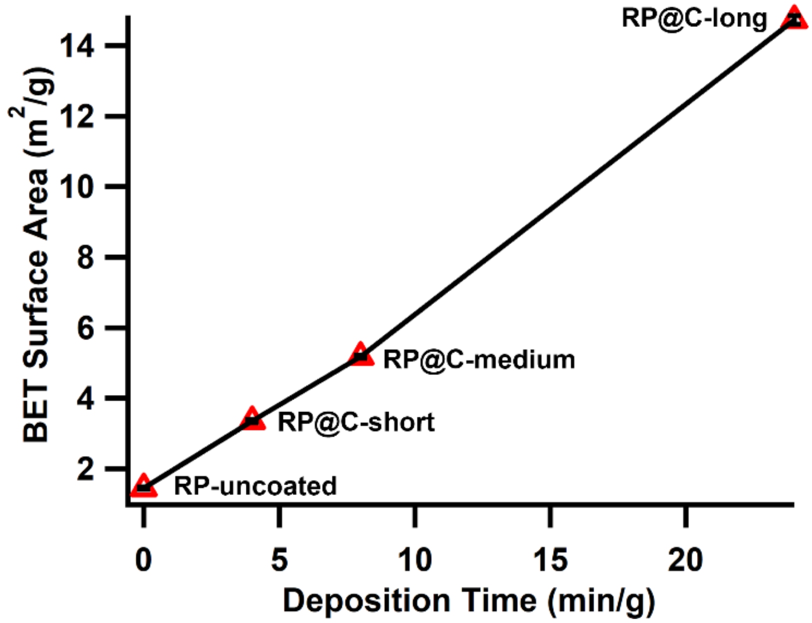

Figure A.2.2. BET surface for non-aged red phosphorus particles with increasing carbon deposition time.

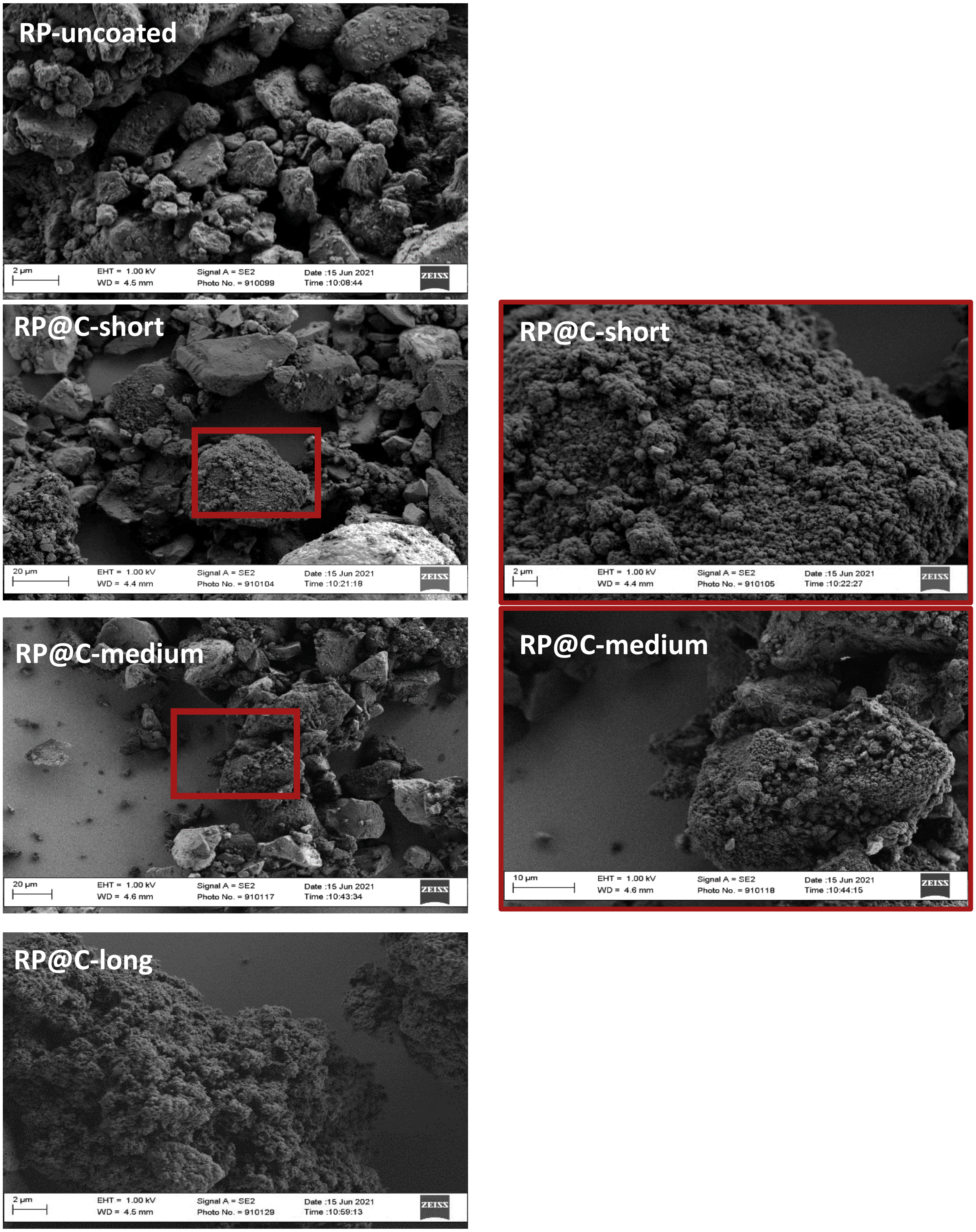

Figure A.2.3. SEM micrographs of non-aged red phosphorus samples with varying carbon deposition times.

Table A.2.1. Effect of PDC deposition time of G position and ratio of intensities of D and G bands from Raman for nonaged red phosphorus.

PDC Deposition Time	G position (cm^{-1})	I(D)/I(G)
Short	1586.8 ± 0	0.466 ± 0.004
Medium	1588.8 ± 3.3	0.44 ± 0.03
Long	1585.5 ± 1.1	0.45 ± 0.03

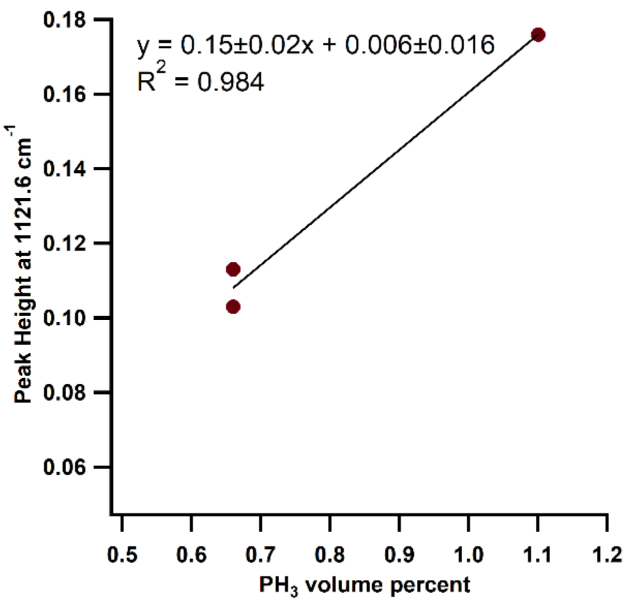

Figure A.2.4. Experimental calibration curve for gas-phase IR calculations.

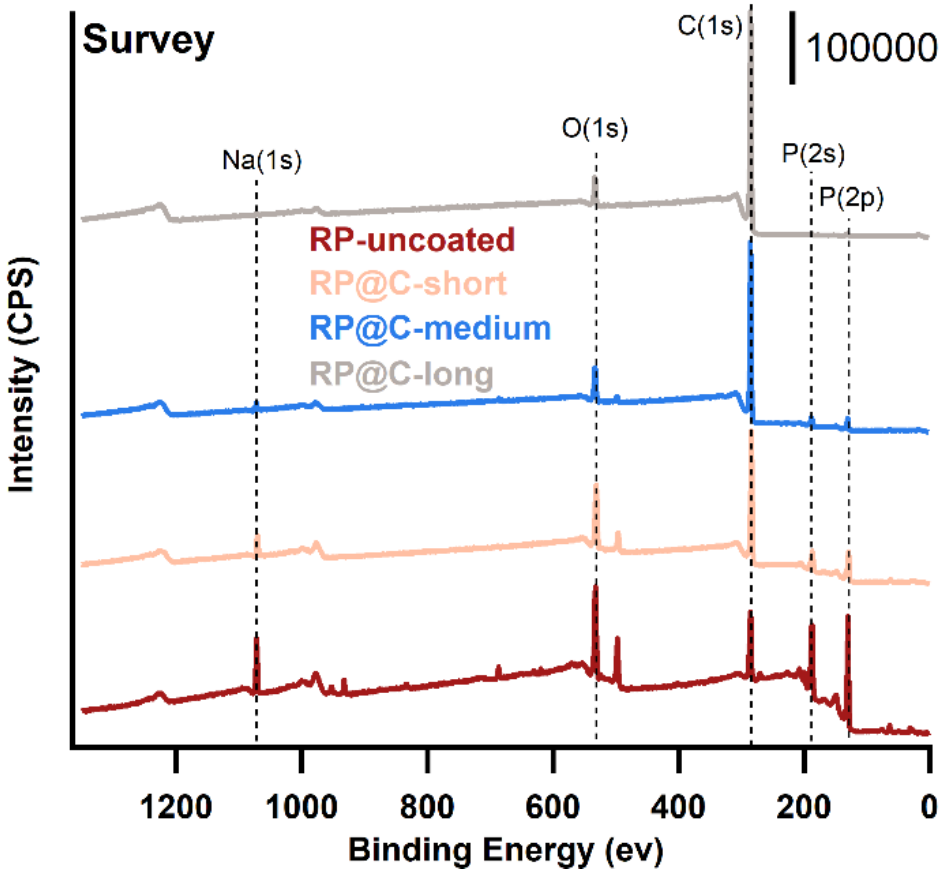

Figure A.2.5. XPS survey spectra and nonaged particles with carbon deposition times of 0-24 min.

Table A.2.2. Atomic percent from XPS for carbon, elemental phosphorus, and POx species as an effect of carbon deposition time and aging.

PDC Deposition Time (min/g)	Aging Time (hr)	% Carbon	%C Stan. Dev.	% Total P	%Total P Stan. Dev.	% PO_x	%PO_x Stan. Dev.	% Elemental P	% Elemental P Stan. Dev.
0 (Uncoated)	0	49.22	2.99	50.78	2.99	7.21	1.97	43.57	1.11
0 (Uncoated)	48	48.58	3.42	51.42	3.42	24.76	3.69	26.66	1.01
4 (short)	0	87.09	2.12	12.91	2.12	4.11	0.23	8.81	1.99
4 (short)	48	74.84	1.51	25.16	1.51	14.01	0.81	11.14	1.99
8 (medium)	0	94.98	0.60	5.02	0.60	1.53	0.24	3.49	0.50
8 (medium)	48	90.75	1.17	9.25	1.17	5.12	0.94	4.13	0.67
24 (long)	0	99.00	0.28	1.00	0.28	0.43	0.06	0.57	0.29
24 (long)	48	97.25	0.96	2.75	0.96	2.01	0.89	0.74	0.15

Appendix 3: Supplementary Information for Chapter 3: Thin carbon scaffold on metal oxide nanomaterials for stable covalent functionalization

A.3.1. Methods

A.3.1.1. EDC Coupling on Al_2O_3@C-COOH Nanoparticles

EDC coupling on Al_2O_3@C NP was done with N-BOC-ethylenediamine, 1H, 1H-undecafluorohexylamine, and (2-aminoethyl)trimethylammonium chloride hydrochloride using a procedure reported previously (Scheme 3.2).[1, 2] Briefly, 20 mM 2-(N-morpholino)ethanesulfonic acid (MES), 1 mM 1-Ethyl-3-(3-dimethylaminopropyl)carbodiimide (EDC), and 1mM N-Hydroxysulfosuccinimide (sulfo-NHS) were added to nanopure water, and the pH was adjusted to 6.5. An additional 20 mM buffer solution was made without EDC or sulfo-NHS as a control. MES buffer solution (7.37 mL), with and without EDC/sulfo-NHS, was added to a 15 mL falcon tube along with 15 mg of Al_2O_3@C-COOH (synthesized using BPO initiator as reported above). The solution was vortexed to suspend the particles. The R-group of interest was then added (1.1 uL N-BOC-ethylenediamine, 2.2 uL 1H,1H-undecafluorohexalamine, 1.29 mg (2-aminoethyl)trimethylammonium chloride hydrochloride)), and the solution was stirred at room temperature for 12 hours. To wash, each solution was diluted to 40 mL using nanopure water, then centrifuged at 10,000xg for 10 min, and the supernatant was decanted. Between each of the following wash steps, samples were centrifuged for 10 min at 10,000xg. Samples were washed three time with 40 mL H_2O. Samples with fluorine-containing compound were then washed two time with 10 mL hexanes. Samples were then washed in 10 mL of 100 mM KCl three times, and finally was two times in 40 mL H_2O.

After functionalizing Al_2O_3@C-COOH with N-BOC-ethylenediamine (Al_2O_3@C-BOC), the primary amine was deprotected upon removal of the BOC group, seen in Scheme A.3.1. To deprotect, 10 mg of Al_2O_3@C-BOC was suspended in 2 mL of dichloromethane and 2 mL of trifluoroacetic acid. The solution was stirred at room temperature for 30 min. The particles were then diluted to 40 mL using nanopure H_2O and centrifuged at 10,000xg for 20 min. Particles were then washed three times with H_2O, centrifuging at 10,000xg for 20 min between each step.

A.3.1.1. Synthesis of Fe_3O_4 Nanoparticles

Superparamagnetic Fe_3O_4 nanoparticles were synthesized as previously reported.[3] Briefly, 5.2 g $FeCl_3$ and 2.0 g $FeCl_2$ were dissolved in 25 mL deoxygenated nanopure water (18 MΩ·cm) containing 0.85 mL of 12.1 N HCl (37% wt). Iron solution was added dropwise into 250 mL 1.5 M NaOH solution under vigorous stirring, forming black precipitate. Particles were isolated by centrifugation at 13048xg, resuspended in deoxygenated water and isolated again at 13048xg. To neutralize anionic charge of particles, particles were washed with 500 mL 0.01 M HCl, then washed once more with water.

A.3.1.3. Synthesis of Ruby Nanoparticles

Ruby synthesis was adapted from a previously published method.[4] A stock solution of 1.33 M $Al(NO_3)_3\cdot 9H_2O$, 0.0133 M $Cr(NO_3)_3\cdot 9H_2O$, and 3.33 M urea was prepared and stirred for 3 h until a blue-green hue developed. After which, 5 mL of solution was transferred to an alumina crucible and placed in a pre-heated furnace at 750˚C, quickly boiling off water and igniting the remaining reagents. (DANGER: THIS IS A HIGHLY EXOTHERMIC REACTION THAT RELEASES TOXIC FUMES.) The 1-minute combustion yielded a solid pink foam which was ground in a mortar and pestle until 3 g of powder were obtained. The powder was transferred to a zirconia grinding cup (SPEX) along with 30 g of 0.2 mm zirconia grinding medium (Glen Mills) and 9 mL of pH 4 HCl. The sample was ground with a 8000M Mixer/Mill (SPEX) for 8 h, with ~300 µL of 1M HCl added every hour. The resulting mixture was passed through a stainless-steel mesh (2µm pore size, TWP) along with ~50 mL of 18.2 MΩ·cm water. The sample was pelleted via centrifugation at 4696x*g* for 10 min, and the supernatant was discarded. 10 mL of 80% H_2SO_4 was added to the pellet and left to sit for 10 min to remove any zirconia contaminants. The H_2SO_4 was poured off, and the resulting ruby pellet was washed 2× with 18.2 MΩ·cm water. The ruby was then washed with alkaline and acid washes to remove surface adsorbed species as described previously.[5] Briefly, the ruby nanoparticles were washed 2× with pH 12 NaOH (Sigma Aldrich), followed by 2× water rinses, and then washed 2× with pH 2 HCl (Sigma Aldrich). The ruby was rinsed 3× with 18.2 MΩ·cm water. To remove aggregates, the ruby was re-suspended in water and centrifuged at 1000xg for 2 minutes. The pellet was discarded, and the supernatant was the final ruby product.

A.3.2. Additional Figures

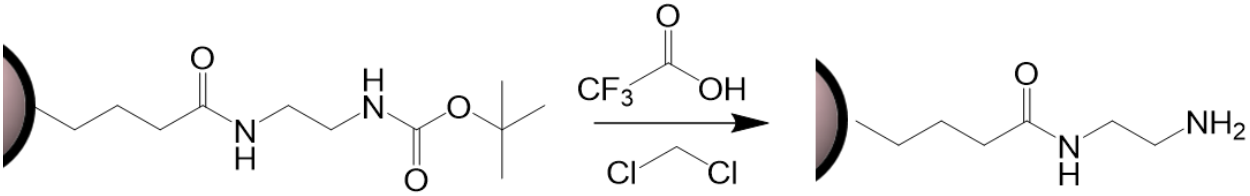

Scheme A.3.1. Deprotection of BOC-protected amine on Al_2O_3@C using trifluoroacetic acid.

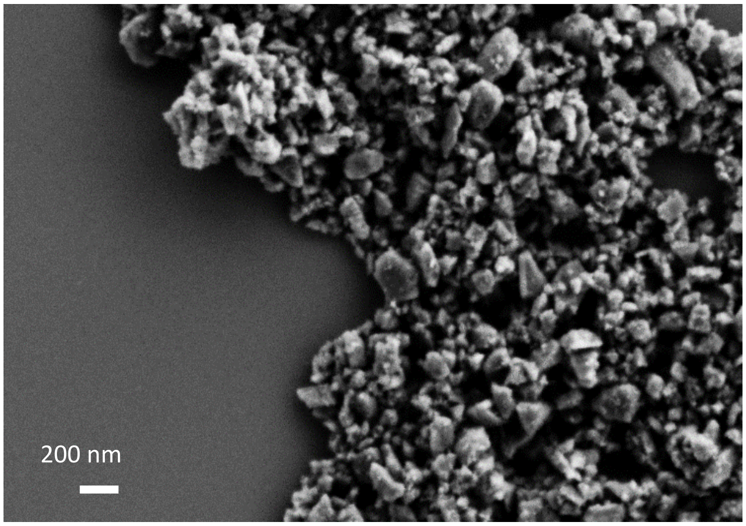

Figure A.3.1. Scanning electron microscopy of bare nanoruby.

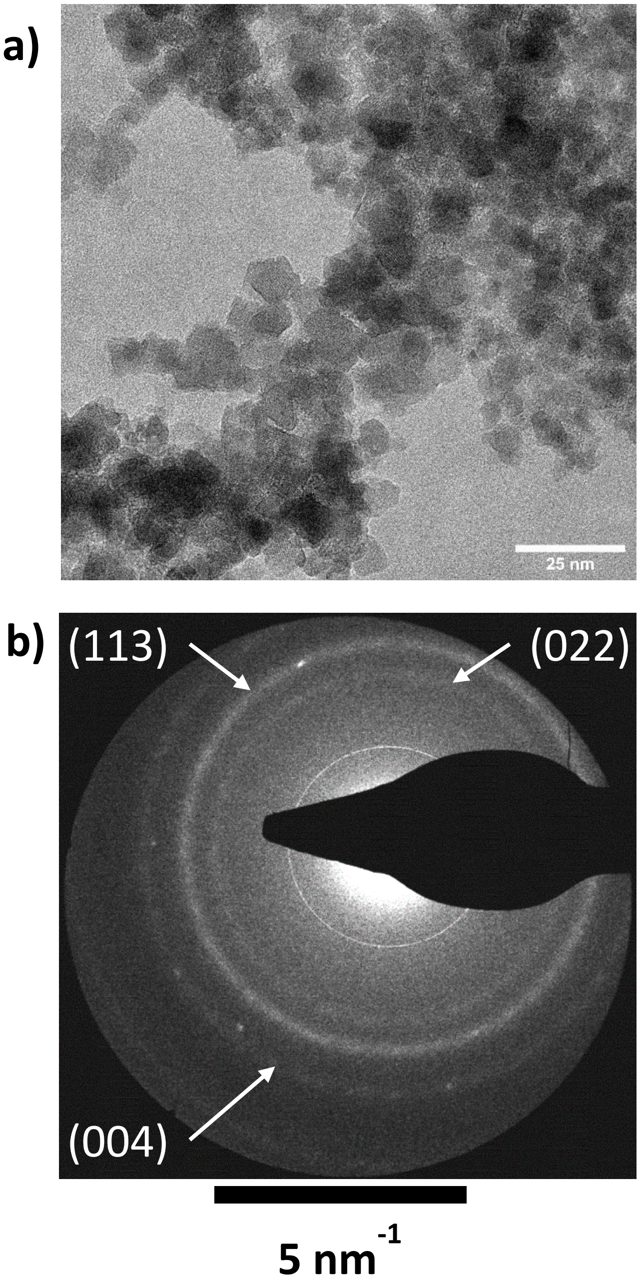

Figure A.3.2. (a) TEM of synthesized Fe3O4 nanoparticles and (b) selected area electron diffraction of Fe_3O_4 NP.

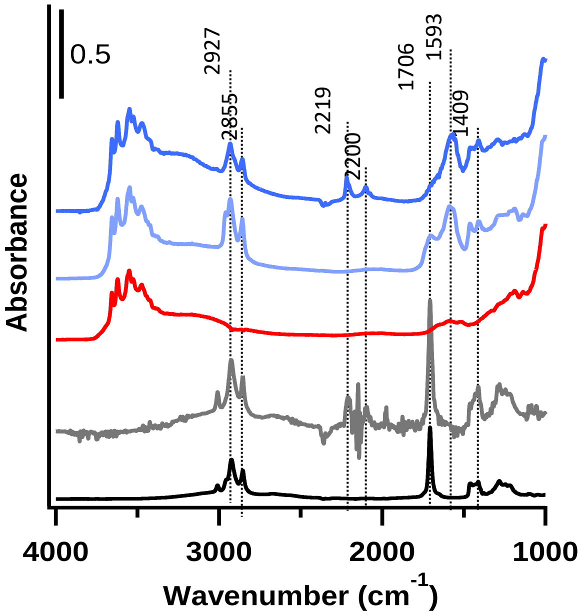

Figure A.3.3. IR spectra comparing LA-Al_2O_3 NP adsorbed linoleic acid and deuterated linoleic acid to neat linoleic acid and d11-linoleic acid.

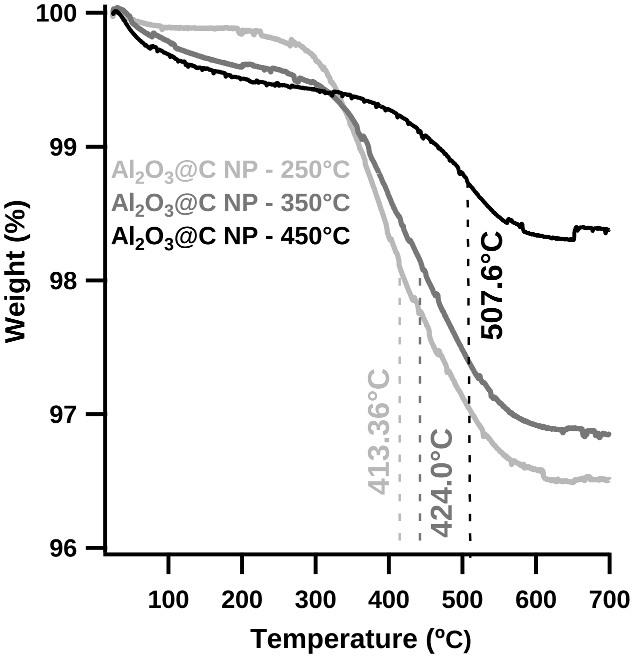

Figure A.3.4. Thermal gravimetric analysis of Al_2O_3@C NP carbonized at various temperatures.

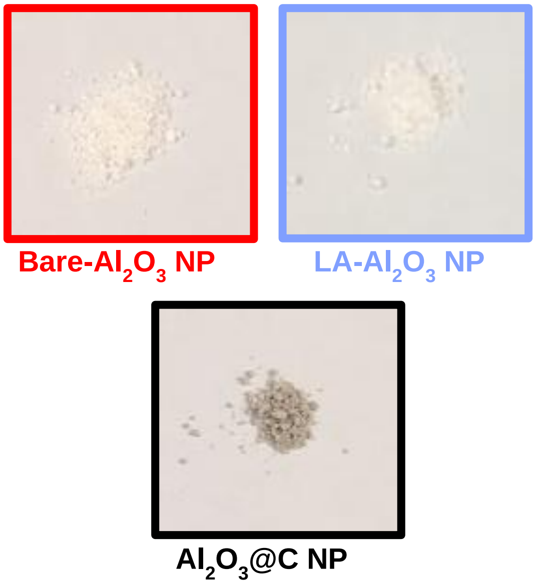

Figure A.3.5. Images of Al_2O_3 NP during the adsorption and carbonization process.

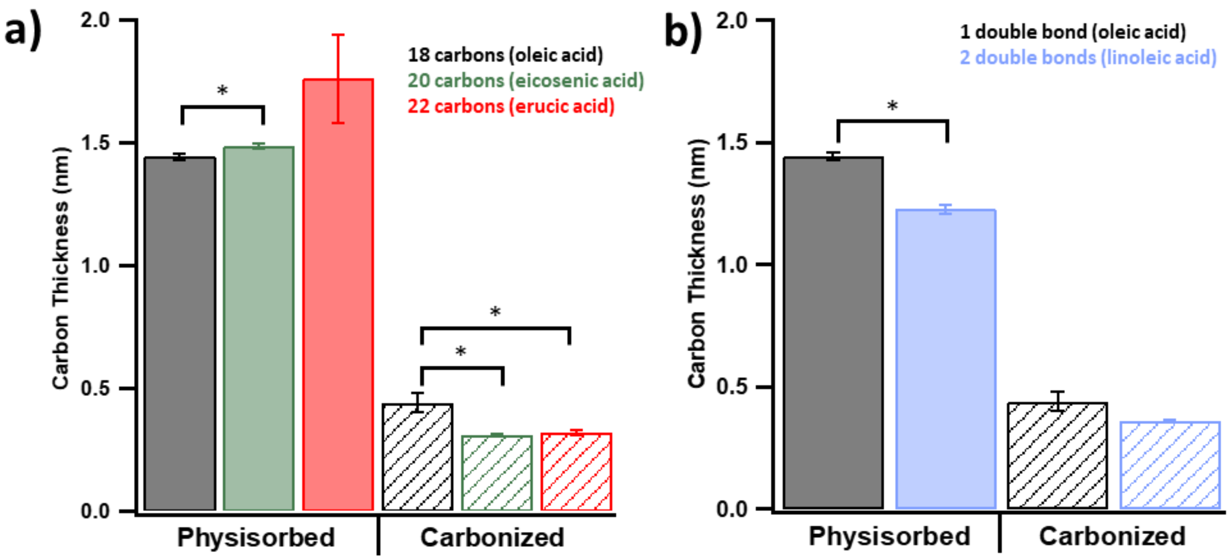

Figure A.3.6. Carbon thickness calculated from XPS for (a) fatty acids with varying chain length and one degree of saturation and (b) 18-carbon long fatty acids with varying degrees of saturation.

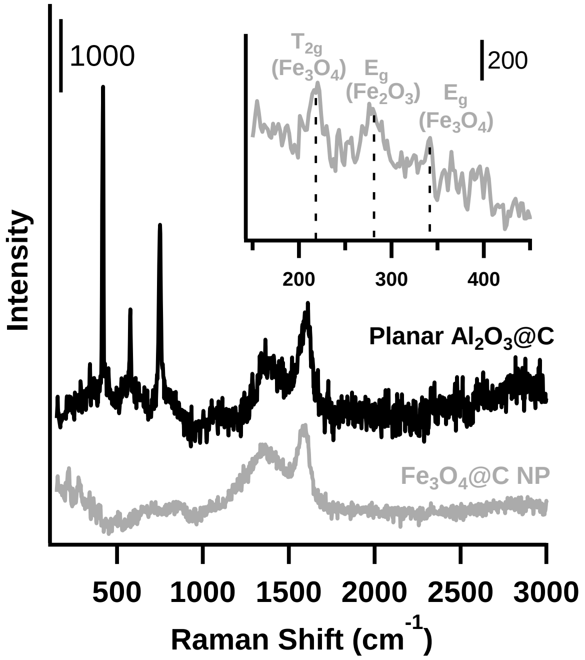

Figure A.3.7. Comparison of Raman spectra F$_e$3O$_4$@C NP and planar Al$_2$O$_3$@C.

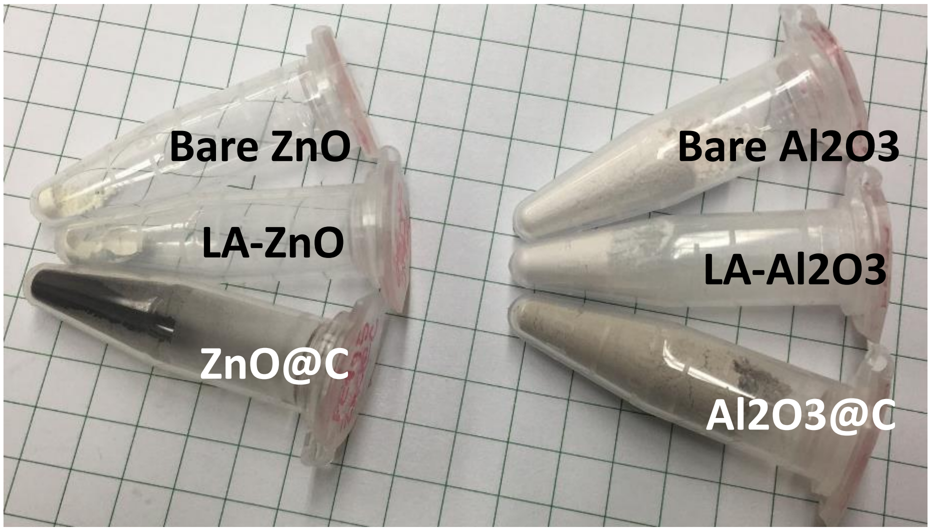

Figure A.3.8. Comparison of ZnO and Al2O3 NP before and after carbonization at 450C.

Table A.3.1. Fatty acids and their corresponding chain length and degree of saturation.

Name	Chain Length	# of double bonds
Linoleic acid	18 carbons	2
Eicosadienoic acid	20 carbons	2
Eicosenic acid	20 carbons	1
Arachidonic acid	20 carbons	4
Oleic acid	18 carbons	1
Erucic acid	22 carbons	1

Table A.3.2. Calculated carbon thickness from XPS for functionalized Al_2O_3@C NP with various ligands via EDC coupling.

Sample	Average Carbon Thickness (nm)
Al_2O_3@C-BOC	0.782 ± 0.008
Al_2O_3@C-BOC (no EDC)	0.872 ± 0.008
Al_2O_3@C-N^+	2.15 ± 0.06
Al_2O_3@C-N^+ (no EDC)	0.96 ± 0.02
Al_2O_3@C-Fluro	2.2 ± 0.3
Al_2O_3@C-Fluro (no EDC)	1.35 ± 0.08

Table A.3.3. Surface coverage of nitrogen, fluorine, and sulfur calculated from XPS on functionalized Al_2O_3@C NP via EDC coupling.

Sample	N Coverage (atoms/nm^2)	F Coverage (atoms/nm^2)	Sulfur Coverage (atoms/nm^2)
Al_2O_3@C-BOC	1.65 ± 0.11		0.42 ± 0.09
Al_2O_3@C-BOC (no EDC)	0.25 ± 0.01		0.50 ± 0.08
Al_2O_3@C-N+	2.65 ± 0.13		2.3 ± 1.5
Al_2O_3@C-N+ (no EDC)	0.19 ± 0.05		0.1 ± 0.6
Al_2O_3@C-Fluro	7.3 ± 0.8	56 ± 6	4.3 ± 0.6
Al_2O_3@C-Fluro (no EDC)	0.08 ± 0.08	2.68 ± 0.19	2.4 ± 2.7

A.3.3. References

1. Bachman, B. F.; Jones, Z. R.; Jaffe, G. R.; Salman, J.; Wambold, R.; Yu, Z.; Choy, J. T.; Kolkowitz, S. J.; Eriksson, M. A.; Kats, M. A.; Hamers, R. J., High-Density Covalent Grafting of Spin-Active Molecular Moieties to Diamond Surfaces. *Langmuir* **2021,** *37* (30), 9222-9231.

2. Sehgal, D.; Vijay, I. K., A Method for the High Efficiency of Water-Soluble Carbodiimide-Mediated Amidation. *Analytical Biochemistry* **1994,** *218* (1), 87-91.

3. Kang, Y. S.; Risbud, S.; Rabolt, J. F.; Stroeve, P., Synthesis and characterization of nanometer-size Fe3O4 and γ-Fe2O3 particles. *Chemistry of Materials* **1996,** *8* (9), 2209-2211.

4. Rani, G.; Sahare, P. D., Structural and photoluminescent properties of Al2O3:Cr3+ nanoparticles via solution combustion synthesis method. *Advanced Powder Technology* **2014,** *25* (2), 767-772.

5. Sreenivasan, V. K. A.; Wan Razali, W. A.; Zhang, K.; Pillai, R. R.; Saini, A.; Denkova, D.; Santiago, M.; Brown, H.; Thompson, J.; Connor, M.; Goldys, E. M.; Zvyagin, A. V., Development of Bright and Biocompatible Nanoruby and Its Application to Background-Free Time-Gated Imaging of G-Protein-Coupled Receptors. *ACS Applied Materials & Interfaces* **2017,** *9* (45), 39197-39208.